

UNIVERSITY OF CALIFORNIA,  
IRVINE

**Effects of Vertically-Resolved Solar Heating, Snow Aging, and Black  
Carbon on Snow-Albedo Feedback**

DISSERTATION

submitted in partial satisfaction of the requirements  
for the degree of

DOCTOR OF PHILOSOPHY

in Earth System Science

by

Mark G. Flanner

Dissertation Committee:  
Professor Charles S. Zender, Chair  
Professor James T. Randerson  
Professor Eric S. Saltzman

2007

Chapter 2 © 2005 American Geophysical Union  
Chapter 3 © 2006 American Geophysical Union  
Chapter 4 © 2007 American Geophysical Union  
All other materials © 2007 Mark G. Flanner

The dissertation of Mark G. Flanner  
is approved and is acceptable in quality and form for  
publication on microfilm and in digital formats:

---

---

---

Committee Chair

University of California, Irvine  
2007

*To my parents, John and Cindy.*

# TABLE OF CONTENTS

LIST OF FIGURES	vi
LIST OF TABLES	viii
ACKNOWLEDGMENTS	ix
CURRICULUM VITAE	x
ABSTRACT OF THE DISSERTATION	xi
<b>1 Introduction</b>	<b>1</b>
1.1 Snow and Climate . . . . .	1
1.2 Previous Studies . . . . .	3
1.3 Models Used in this Study . . . . .	6
1.4 Organization of Research . . . . .	9
<b>2 Snowpack Radiative Heating: Influence on Tibetan Plateau Climate</b>	<b>11</b>
2.1 Abstract . . . . .	11
2.2 Introduction . . . . .	12
2.3 Methods . . . . .	12
2.4 Results and Discussion . . . . .	14
2.5 Conclusions . . . . .	20
2.6 Acknowledgments . . . . .	21
<b>3 Linking Snowpack Microphysics and Albedo Evolution</b>	<b>22</b>
3.1 Abstract . . . . .	22

3.2	Introduction . . . . .	23
3.3	Theory and Methods . . . . .	25
3.4	Results and Discussion . . . . .	34
3.5	Conclusions . . . . .	44
3.6	Acknowledgements . . . . .	47
<b>4</b>	<b>Present Day Climate Forcing and Response from Black Carbon in Snow</b>	<b>48</b>
4.1	Abstract . . . . .	48
4.2	Introduction . . . . .	49
4.3	Methods . . . . .	51
4.4	Results and Discussion . . . . .	61
4.5	Conclusions . . . . .	87
4.6	Acknowledgments . . . . .	88
<b>5</b>	<b>Conclusions</b>	<b>89</b>
5.1	Summary of Results . . . . .	89
5.2	Implications for Future Studies . . . . .	92
	<b>Bibliography</b>	<b>94</b>
<b>A</b>	<b>List of Symbols</b>	<b>108</b>

# LIST OF FIGURES

1.1	Coupled feedback mechanisms involving changes in snow cover, net surface radiation, albedo, snow grain size, and absorbing impurities. . . . .	8
2.1	Solar absorption profiles prescribed by CLM and predicted by SNICAR. . . . .	16
2.2	Climatological annual mean difference in 2 m air temperature caused by sub-surface snowpack solar absorption. . . . .	17
2.3	Annual cycle of observed and simulated snow depth over the Tibetan Plateau. . . . .	19
2.4	Annual cycle of observed and simulated 2 m air temperature over the Tibetan Plateau. . . . .	21
3.1	Comparison of model predictions of isothermal specific surface area evolution with measurements from <i>Legagneux et al.</i> (2004). . . . .	36
3.2	Comparison of model-predicted mean radius with observations from <i>Fukuzawa and Akitaya</i> (1993) under various temperature gradients. . . . .	37
3.3	Model parameter study illustrating the evolution of snow effective radius ( $r_e$ ) and albedo evolution, isolating dependence of initial size distribution, temperature, temperature gradient, and snow density. . . . .	40
3.4	Observed and modeled albedo decay at Niwot Ridge following the January 2, 2001 snowfall event. . . . .	43
3.5	Comparison of modeled specific surface area (SSA) evolution with parameterization from Equation 3.16, using best-fit parameters. . . . .	45
4.1	Zonal annual mean black carbon emissions from fossil fuel+biofuel combustion ( <i>Bond et al.</i> , 2004) and biomass burning during 1998 and 2001 ( <i>Van der Werf et al.</i> , 2006). . . . .	56
4.2	Measured diffuse incident radiation snow albedo at the South Pole from <i>Grenfell et al.</i> (1994) and modeled albedo from SNICAR. . . . .	62

4.3	Spectrally-averaged snow albedo and fraction of total absorption occurring more than 2 cm beneath the surface as functions of BC mass concentration for various snow effective radii. . . . .	64
4.4	Model vs. observed BC concentrations in near-surface snow for data from Table 4.2. . . . .	68
4.5	Annual mean predicted BC concentrations in snow using central estimate fossil fuel and biofuel sources only, and fossil fuel, biofuel, and 1998 biomass burning emission sources. . . . .	69
4.6	Central estimates of 1998 surface forcing from BC in snow. . . . .	77
4.7	Zonal mean surface forcing from BC in snow as a function of month and latitude. . . . .	79
4.8	Difference in zonal monthly mean land snowmelt rate between experiments with and without black carbon in snow. . . . .	80
4.9	Difference in zonal monthly mean surface albedo between experiments with and without black carbon in snow. . . . .	82
4.10	Difference in zonal monthly mean 2-meter air temperature between experiments with and without black carbon in snow. . . . .	84



# LIST OF TABLES

2.1	Numerical experiments . . . . .	13
2.2	Global land and Tibetan Plateau (TP) changes in snow depth, 2 m air temperature, and surface albedo caused by vertically-resolved snow-pack solar absorption. . . . .	15
3.1	Parameters $\hat{S}_0$ , $\kappa$ , and $\tau$ for observations of fresh snow evolution from Table III of <i>Legagneux et al.</i> (2004) . . . . .	34
3.2	Long-term temperature gradient growth . . . . .	38
3.3	Experimental configurations for Figure 3.3 . . . . .	39
3.4	Best-fit parameters of Equation 3.16 for the range of temperatures, temperature gradient, and snow density shown in Figure 3.5 . . . . .	45
4.1	Configurations for 1998 and 2001 low, central, and high experiments .	55
4.2	Comparison of modeled and measured BC in snow, sea-ice, and precipitation . . . . .	67
4.3	Summary of model experiment results . . . . .	72
4.4	Range of change in global mean BC/snow radiative forcing resulting from uncertainty in individual factors. . . . .	86

# ACKNOWLEDGMENTS

As an undergraduate near completion of my studies in engineering, I took a class entitled “Scientific Background to Global Environmental Problems,” instructed by Francis Bretherton. His teaching style and the subject matter made it was one of those rare classes that a student looks forward to each day. Without that most intellectually stimulating experience, I would not have pursued this Ph.D.

Charlie Zender provided superb mentorship. His open-door policy permitted countless spontaneous, engaging conversations. He provided more than a basic introduction to the indispensable tools which carved this dissertation and encouraged me to pursue what interested me most.

Jim Randerson also kindled many interesting conversations and offered crucial help with Chapter 4. Tom Painter and Jeff Dozier introduced me to field methods in snowy, mountainous (and fun) terrain. Phil Rasch’s aerosol transport model and support for Chapter 4 were critical. Other scientists who contributed important data or comments include Steve Warren, Tom Grenfell, Tami Bond, Zong-Liang Yang, Walter Rosenthal, Keith Oleson, Florent Dominé, and Teruo Aoki. Equally important has been the logistical support of Liz Ford and Cynthia Dennis, and free lunches provided by the department. Conversations with the Zender group, Mariah Carbone, Chris Doughty, Andrew McMillan, and Adrian Rocha broadened my scientific horizons.

Finally, the balance to life brought by Katie and our friends has promoted a healthy lifestyle and state of mind, benefiting academic pursuits. I am grateful for their support and patience.

Funding for this research was provided by the NASA Earth System Science Fellowship (NNG05GP30H) and NSF/NCAR SGER ATM-0503148. Computations were conducted with the Earth System Modeling Facility, NSF ATM-0321380.

# CURRICULUM VITAE

Mark G. Flanner

## Education

2002–2007 Ph.D., Earth System Science, University of California, Irvine  
1997–2002 B.S., Biomedical Engineering, University of Wisconsin, Madison

## Funding and Awards

2006 Outstanding Student Presentation Award,  
Fall 2005 Meeting of the American Geophysical Union  
2005 UCI Medal Award  
2004 – present NASA Earth System Science Fellowship

## Teaching Experience

Winter Quarter, 2004 Teaching Assistant, Oceanography (ESS3),  
Professor François Primeau  
Fall Quarter, 2003 Teaching Assistant, The Physical Environment (ESS1),  
Professor Bill Reeburgh

## Publications

1. **Flanner, M. G.**, C. S. Zender, J. T. Randerson, and P. J. Rasch (2007), Present day climate forcing and response from black carbon in snow, *J. Geophys. Res.*, *in press*.
2. Painter, T. H., N. P. Molotch, M. Cassidy, **M. G. Flanner**, and K. Steffen (2007), Contact spectroscopy for the determination of snow optical grain size, *J. Glaciol.*, **53**, 180, 121–127.
3. Randerson, J. T., H. Liu, **M. G. Flanner**, S. D. Chambers, Y. Jin, P. G. Hess, G. Pfister, M. C. Mack, K. K. Treseder, L. R. Welp, F. S. Chapin, J. W. Harden, M. L. Goulden, E. Lyons, J. C. Neff, E. A. G. Schuur, and C. S. Zender (2006), The impact of boreal forest fire on climate warming, *Science*, **314**, doi:10.1126/science.1132075, 1130–1132.
4. **Flanner, M. G.**, and C. S. Zender (2006), Linking snowpack microphysics and albedo evolution, *J. Geophys. Res.*, **111**, D12208, doi:10.1029/2005JD006834.
5. **Flanner, M. G.**, and C. S. Zender (2005), Snowpack radiative heating: Influence on Tibetan Plateau climate, *Geophys. Res. Lett.*, **32**, L06501, doi:10.1029/2004GL022076.

# ABSTRACT OF THE DISSERTATION

## Effects of Vertically-Resolved Solar Heating, Snow Aging, and Black Carbon on Snow-Albedo Feedback

by

Mark G. Flanner

Doctor of Philosophy in Earth System Science

University of California, Irvine, 2007

Professor Charles S. Zender, Chair

Snow cover is an important control on climate because it reflects a large fraction of solar radiation. Interaction between solar radiation and snow determines the strength of snow-albedo feedback, but this interaction has been crudely represented in climate models. This research employs Mie theory, a two-stream radiative transfer model, and snow microphysics to improve understanding of snow-radiation interaction, including vertically-resolved absorption in the snow column, evolution of snow optical properties following snowfall, and the influence of black carbon. First, we incorporate realistic solar heating in subsurface snow layers of the National Center for Atmospheric Research (NCAR) Community Land Model (CLM). Climate sensitivity experiments isolating the influence of this energy repartitioning show a large effect over the Tibetan Plateau. Because of intense insolation and low solar zenith angle, snowmelt in this region is initiated beneath the surface. Snow-albedo feedback strengthens the initial effect, and winter snow mass is reduced by 80% in equilibrium climate studies, reducing model bias relative to observation. Next, we develop a microphysical model that predicts the evolution of dry snow effective grain size as a function of snow temperature, temperature gradient, and density. Effective grain size determines snow albedo, the depth profile of absorption, and the perturbation to snow albedo by impurities like black carbon. We find that a large temperature gradient, coupled with high temperature and low density, can drive rapid grain growth

and a concurrent reduction in albedo. We parameterize this model for use in climate studies, improving on previous representations of snow albedo evolution that depend only on temperature. Finally, we apply a climate model to assess present-day climate sensitivity to black carbon in snow, accounting for fossil fuel and wildfire sources. We estimate a relatively small global radiative forcing, but greater “efficacy,” or change in global mean temperature per unit power of forcing, from this effect than any other anthropogenic forcing. The forcing maximum coincides with onset of local springtime snowmelt, hastening melt and triggering strong snow-albedo feedback. A second positive feedback, not accounted for in previous studies, involves more rapid grain growth caused by aerosol heating. We estimate a large range of possible forcing, caused primarily by uncertainty in black carbon emissions and snow aging.

# CHAPTER 1

## Introduction

### 1.1 Snow and Climate

Snow is a unique, climatologically important substance. It reflects a greater fraction of solar energy than any other substance that pervades Earth's surface. Snow's high reflectivity, or *albedo*, occurs in spite of being composed of ice and air, both highly transmissive substances in the visible portion of the spectrum, and is a consequence of their different indices of refraction. Ice on Earth, even in cold regions, also has a very high homologous temperature, the ratio of its absolute temperature to melting temperature. This means that slight increases in its energy content can induce melting. When snow melts and flows off or infiltrates into the ground, it generally exposes a much darker underlying substrate, such as soil, vegetation, rock, sea-ice, firn, or solid glacier. Pooled meltwater on a surface also constitutes a darker medium because of water's high transmissivity. As the darker surface absorbs a greater portion of incident solar energy, it warms at a greater rate (depending on specific heat capacity) than the snow-covered surface. Thus, the melting of snow represents a highly non-linear process in Earth's climate system, dramatically altering the optical characteristics of the surface, leading to an increasing rate of surface heating. This dissertation strives to improve understanding of how solar radiation interacts with snow and the consequences of this interaction for climate change.

*Croll* (1867) recognized that slight changes in orbital variation could drive ice sheet growth or decay via radiative feedback. Early one-dimensional climate modeling studies (*Budyko*, 1969; *Sellers*, 1969) identified very large climate sensitivity associated with wholesale removal of polar ice caps. The primary cause of this climate instability, the large change in surface albedo, was later termed *ice-albedo feedback*, although changes in meridional heat transport associated with removal of the ice thermal insulator were also identified as important. In this context, *ice-albedo feedback* refers to large changes in the areal extent of ice-sheets and sea-ice occurring on long timescales (centuries to millennia). This dissertation instead deals with shorter-timescale feedbacks associated with changes in snow optical properties and seasonal snow cover, so we apply the term *snow-albedo feedback* (e.g., *Randall et al.*, 1994; *Lynch et al.*, 1998; *Hall*, 2004) in discussions that follow. Relevant changes in snow optical properties occur on timescales of days and climate feedback induced by snow ablation and accumulation occur on monthly to interannual timescales.

Albedo change, the focus of this dissertation, is likely the dominant feedback associated with snow cover change, although it is only one of many feedbacks. *Cess et al.* (1991) and *Randall et al.* (1994) identified net climate feedback from snow cover changes driven by sea surface temperature forcing ranging from weakly *negative* to strongly positive in 17 early general circulation models. The primary source of uncertainty was cloud feedback. Widespread, thick cloud cover masks the top-of-atmosphere solar radiative response to changes in surface albedo, and models diverged considerably in responding to snow cover reduction with increasing or decreasing cloud cover and thickness. More recently, *Qu and Hall* (2006) found remarkable congruity between 17 climate models and observations from the International Cloud Climatology Project (ISCCP) of the quantity  $\partial\alpha_p/\partial\alpha_s$ , the change in planetary albedo with change in surface albedo, in spite of widely different cloud parameterizations. Averaged over northern extratropical land, they found  $\partial\alpha_p/\partial\alpha_s = 0.52 \pm 0.04$ . Longwave radiative response tends to be a negative feedback on snow cover change. This is simply because a snow-covered surface cannot be warmer than 0°C, whereas warmer surfaces emit more longwave energy (Stefan-Boltzmann feedback). Some models examined by *Cess et al.* (1991) and *Randall et al.* (1994) showed a *positive* longwave radiative feedback to reduced snow cover though. This happened either because of

large increases in atmospheric water vapor or steeper lapse rates reducing the atmospheric radiative emission to space. Longwave responses from cloud changes are also very important. *Zhang et al.* (1996) showed that low polar clouds actually enhance Arctic snowmelt during the onset phase because they increase downwelling longwave energy more than they decrease surface-incident solar energy. Nearly all models discussed by *Cess et al.* (1991) and *Randall et al.* (1994) showed a greater solar radiative response to snow cover change than longwave response. Changes in latent and sensible heat fluxes can also feed back on snow evolution, but often offset each other and have no direct influence on the total surface-atmosphere energy budget, measured at the tropopause or top of atmosphere.

## 1.2 Previous Studies

### 1.2.1 Models of Snow Radiative Processes

An important component of any model used to study snow-albedo feedback is that which represents the interaction of solar radiation with snow. *Wiscombe and Warren* (1980) developed the first generalized, physically-based model of snow albedo that was valid over the entire solar spectrum, accounted for an arbitrary combination of direct and diffuse incident radiation, and represented the forward-scattering nature of snow in a realistic manner. They applied Mie theory (an analytic solution of Maxwell's equations) to estimate scattering and absorption properties of spherical ice particles, given the particle size and spectrally-dependent complex index of refraction of ice. To account for multiple scattering, they applied the delta-Eddington two-stream approximation (*Joseph et al.*, 1976), which is an appropriate radiative transfer model for strongly forward-scattering, optically-thick media such as snow. (Snow scatters strongly in the forward direction because the primary means of photon redirection is refraction through the ice particle, rather than reflectance from the particle surface.)

*Wiscombe and Warren* (1980) showed a favorable comparison of their model with snow albedo measurements in the near-infrared part of the spectrum, but over-predicted observed albedo in the visible spectrum. A seminal companion study (*Warren and Wiscombe*, 1980) modified the pure snow model to account for impurities and



demonstrated that extremely small concentrations (less than 1 ppm) of soot (or *black carbon*) could significantly reduce visible albedo. They suggested that polar albedo measurements used for comparison (*Grenfell and Maykut*, 1977; *Kuhn and Siogas*, 1977) were likely contaminated because of proximity to camp. Later observations of clean snow albedo in Antarctica (*Grenfell et al.*, 1994) confirmed this hypothesis by showing higher visible albedo, closely matching model predictions of clean snow.

*Grenfell* (1991) later developed a multi-layer, multi-stream model for studying solar radiative transfer through sea-ice. The multi-layer representation built on *Wiscombe and Warren* (1980) by allowing for vertical inhomogeneity in optical properties, a critical feature of sea-ice, which generally has a surface snow layer and subsurface ice layers with distinct air bubble and brine concentrations. This dissertation does not examine radiative transfer through sea-ice, but we also apply a multi-layer model to account for vertically-varying snow density, grain size, and impurity concentration.

### 1.2.2 Snow Aging

It has long been recognized that the mean grain size of snow tends to increase with time (e.g., *Stephenson*, 1967). *Wiscombe and Warren* (1980) realized that grain growth should drive decreasing snow albedo with time, as snow with larger effective grain size is darker. Several studies have modeled dry snow metamorphism and crystal growth with a motivation of understanding avalanche formation (e.g., *Gubler*, 1985; *Brown et al.*, 2001; *Lehning et al.*, 2002), utilizing theory about vapor diffusion caused by differences in particle curvature (the Kelvin Effect) (e.g., *Colbeck*, 1980), and vapor diffusion caused by temperature gradient in snow (e.g., *Marbouty*, 1980; *Colbeck*, 1983a). This dissertation extends theory from these studies to represent the evolution of snow effective radius (the surface area-weighted mean radius), or specific surface area (units of surface area per mass), with an interest in the evolution of snow optical properties.

Effective radius is the most relevant grain size metric for snow optical properties. Following theory suggested by *Bryant and Latimer* (1969) three recent studies (*Grenfell and Warren*, 1999; *Neshyba et al.*, 2003; *Grenfell et al.*, 2005) demonstrate that representing ice media composed of non-spherical particles with a collection of

spheres that conserves the total volume and total surface area (but not the number of particles) yields predictions of hemispheric radiative fluxes typically with  $\pm 5\%$  accuracy. This implies that snow column radiative fluxes can be accurately represented using Mie theory with equivalent surface-area/volume spheres, given known vertically-resolved effective radius.

Current climate models either represent snow albedo as constant or with empirical representations dependent only on temperature (e.g. *Verseghy*, 1991; *Douville et al.*, 1995; *Loth and Graf*, 1998; *Oleson et al.*, 2004). With inclusion of a radiative transfer model for snow, it becomes important to predict the effective radius, rather than albedo itself. *Marshall* (1989) includes an empirical description of grain size evolution in dry and melting snow based on a limited set of measurements in polar snow. For global climate model use, however, it is desirable to have a robust, physically-based model that is valid over a wide range of conditions. Chapter 3 discusses a model that is suitable for dry snow conditions, utilizing recent observations of snow specific surface area evolution (*Legagneux et al.*, 2004).

### 1.2.3 Snow Impurity Influence on Climate

*Warren and Wiscombe* (1985) extended the model of *Warren and Wiscombe* (1980) to include hypothetical snow darkening from soot following full-scale nuclear war. They concluded that the albedo of snow on Greenland and over Arctic sea-ice could be reduced by 0.15–0.5. Although reduced surface insolation from atmospheric soot would offset this effect for some time, reduced snow albedo could persist for several years because of seasonal melting and deep penetration of visible radiation in the snow. To our knowledge, *Warren and Wiscombe* (1985) was the first study to suggest possible global climate effects of anthropogenic snow darkening.

Study of snow darkening from black carbon using a global climate model was not conducted until *Hansen and Nazarenko* (2004). This important study demonstrated that (at least in one model) the climate system is extremely sensitive to widespread changes in snow albedo. They went so far as to suggest that one-quarter of the global warming experienced during the last century may be due to snow darkening. While novel, this study provided only a first-order estimate of snow darkening effects, as

it applied uniform, constant snow albedo reductions across the Arctic and Northern Hemisphere based on only a few measurements. Much of this dissertation was motivated by *Hansen and Nazarenko* (2004); to apply more physically realistic models of snow radiative processes, such as those of *Wiscombe and Warren* (1980) and *Warren and Wiscombe* (1980), to understand the global climate effects of snow darkening from black carbon.

*Jacobson* (2004b) built on *Hansen and Nazarenko* (2004) with a global climate modeling study that predicted snow and ice reflectance using a radiative transfer solution dependent on local black carbon deposition. He predicts equilibrium global warming of  $0.06^{\circ}\text{C}$  from snow darkening by fossil fuel and biofuel black carbon. In estimating the radiative influence of black carbon, *Jacobson* (2004b) assumed uniform (in space and time) snow grain size. Chapters 3 and 4 of this dissertation discuss the importance of snow grain size in determining both pure snow reflectance and the effect of absorbing impurities. Subsequent studies (*Hansen et al.*, 2005, 2006) also allowed for spatially-dependent snow albedo reductions based on local black carbon deposition, lowering their original estimates of global warming from black carbon in snow to  $0.065^{\circ}\text{C}$ . Both *Hansen and Nazarenko* (2004) and *Hansen et al.* (2005) show that forcing from black carbon in snow has extremely high “efficacy,” or change in global mean temperature per unit power of radiative forcing. Efficacy is an important concept for extrapolating radiative forcings to global temperature response. Reasons for high efficacy from black carbon in snow are explored in Chapter 4.

## 1.3 Models Used in this Study

Throughout this dissertation, we develop and apply models appropriate for a wide range of spatial/temporal scales and processes. The most relevant ones are briefly discussed here.

### 1.3.1 Radiative Transfer

Towards the goal of understanding the influence of impurities on snow optical properties, we developed the SNow, ICe, and Aerosol Radiative (SNICAR) model.

SNICAR applies theory from, and builds upon *Wiscombe and Warren (1980)* and *Warren and Wiscombe (1980)*. As alluded to earlier, a key difference is that SNICAR predicts the vertical profile of radiative absorption and transmission, following *Grenfell (1991)*. We implement this via the multi-layer solution of *Toon et al. (1989)*, which utilizes an efficient tri-diagonal matrix solution for any number of layers and allows for different two-stream approximations. We apply the delta-Eddington (*Joseph et al., 1976*) and hemispheric-mean (*Toon et al., 1989*) approximations of multiple-scattering. Representing unique layers, SNICAR accounts for vertical heterogeneity in snow properties such as grain size, density, and impurity concentration. SNICAR is generalized to account for any number and concentrations of impurities, any snow grain size, and varying spectral and vertical resolutions. This flexibility allows for high-resolution “offline” studies of the basic interaction between solar radiation and snow, as well as coupled climate-snow studies requiring lower resolution.

Optical properties that drive SNICAR include single-scattering albedo, mass extinction cross-section, and asymmetry parameter describing the scattering direction. These properties are estimated using Mie theory with spectrally-dependent complex indices of refraction and size distributions of ice particles and impurities. Mie solutions (coded by Charlie Zender) are based on *Wiscombe (1980)* and *Bohren and Huffman (1983)*.

### 1.3.2 Snow Aging

Early in the development of SNICAR, an intricate connection of feedbacks involving impurities and snow grain size became apparent. This is depicted in Figure 1.1. We have already discussed snow-albedo feedback in the context of changes in the areal extent of snow cover. This is depicted by the loop in the upper-left portion of the figure. Starting (arbitrarily) with a reduction in snow cover: this decreases surface albedo, leading to an increase in net radiation (“R<sub>net</sub>”) and therefore temperature, which drives an even greater reduction in snow cover. Coupled with a change in snow temperature (R<sub>net</sub>), within the snow column itself, is a potential increase in snow grain size, as the rate of grain growth is temperature dependent. This is discussed in much more detail (Chapter 3). Furthermore, albedo is reduced with grain coars-

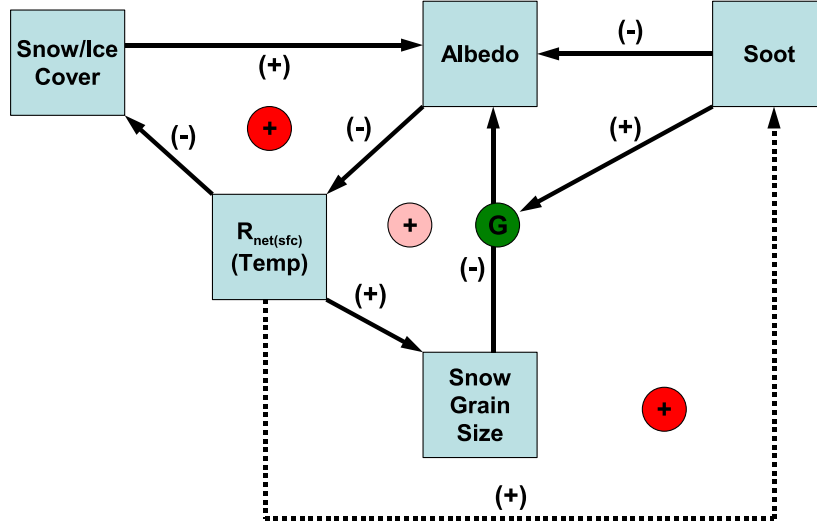


FIGURE 1.1. Coupled feedback mechanisms involving changes in snow cover, net surface radiation ( $R_{\text{net}}$ , or temperature), albedo, snow grain size, and absorbing impurities like soot. “G” represents gain, and the arrow pointing to it indicates increasing feedback gain with time. These feedbacks are described in Section 1.3.2.

ening. This is a consequence of the increase in photon path-length within ice grains, improving the probability of absorption. Therefore, there is a second, weaker positive feedback, depicted by the loop between “Albedo,” “ $R_{\text{net}}$ ,” and “Snow Grain Size.” Increased snowpack heating from absorption by impurities (“Soot”) also triggers these two feedbacks (arrow directed towards “Albedo.”) Furthermore, the instantaneous albedo perturbation caused by the impurity increases with grain coarsening. Reasons for this are discussed in Chapter 4. This effect is denoted with the arrow from “Soot” to “G,” indicating increasing gain on this feedback loop as time progresses. Finally, there is evidence that impurities, especially hydrophobic ones, accumulate near the snow surface during melt, as they are excluded from liquid water that percolates through the snow column (*Conway et al.*, 1996). This implies yet another positive feedback between “ $R_{\text{net}}$ ” (temperature) and the concentration of soot. The overarching goal of this dissertation is to improve understanding of the role of snow impurities in global climate change. A more specific research motivation is exploration of the coupled feedbacks depicted in Figure 1.1.

The model developed for prediction of snow grain size evolution (Chapter 3) uti-

lizes an ensemble of particle sizes and predicts vapor flux between the particles using both implicit and explicit physical assumptions. The vapor flux (and evolution of the particle size distribution) depends on snow temperature, temperature gradient, and density. As an offline microphysical model, these snow state variables are prescribed. Coupled to a climate model however, snow state is predicted with a bulk snowpack model and the evolution of snow optical properties is prognosed with an empirical parameterization of the microphysical model. These details are described in Chapter 4.

### 1.3.3 Global Climate

All global climate studies in this dissertation utilize the National Center for Atmospheric Research (NCAR) Community Atmosphere Model, Version 3 (CAM3) (e.g., *Collins et al.*, 2004). This model includes a slab-ocean model, as opposed to a full ocean model. Climate in this model therefore equilibrates on much shorter timescales. We also use a branch of the model that includes prognostic transport and deposition of carbonaceous aerosols (*Rasch et al.*, 2001) to represent interactive snow darkening. The land component of CAM3 is the Community Land Model (CLM) (*Oleson et al.*, 2004), that includes a snow model based on the work of *Jordan* (1991). The sea-ice component of CAM3 is the Community Sea-Ice Model (CSIM) (*Briegleb et al.*, 2004), based on the Los Alamos CICE model. Radiative transfer and snow aging models from SNICAR, suitable for GCM studies, are coupled to the CLM and CSIM components of CAM3.

## 1.4 Organization of Research

The organization of the rest of this dissertation is as follows: Chapter 2 (*Flanner and Zender*, 2005) discusses the importance of vertically-resolved solar heating in snow for Tibetan Plateau climate. This work followed the initial coupling of SNICAR with CAM3/CLM, which predicted realistic solar absorption in all snow layers, instead of prescribing all absorption to occur in the surface snow layer. The Tibetan Plateau is uniquely vulnerable to this representation because of its altitude and proximity

to the equator. Chapter 3 (*Flanner and Zender, 2006*), motivated by feedbacks depicted in Figure 1.1, discusses the development of a model for the prediction of snow effective grain size evolution. This chapter then discusses snow albedo evolution in response to different snow state regimes, including combinations of snow temperature, temperature gradient, and density. Chapter 4 (*Flanner et al., 2007*) discusses the influence of black carbon in snow on present-day climate, including radiative forcing, climate response, and efficacy. Chapter 5 summarizes the dissertation conclusions and identifies relevant future studies. Appendix A follows the bibliography and contains a list of symbols used in all chapters. Chapters 2, 3, and 4 are nearly verbatim copies of either published or accepted papers and can be read independently.

# CHAPTER 2

## Snowpack Radiative Heating: Influence on Tibetan Plateau Climate

As appears in:

Flanner, M. G., and C. S. Zender (2005), Snowpack radiative heating: Influence on Tibetan Plateau climate, *Geophys. Res. Lett.*, *32*, L06501, doi:10.1029/2004GL022076.

### 2.1 Abstract

Solar absorption decays exponentially with depth in snowpacks. However, most climate models constrain all snowpack absorption to occur uniformly in the top-most snow layer. We show that 20–45% of solar absorption by deep snowpacks occurs more than 2 cm beneath the surface. Accounting for vertically-resolved solar heating alters steady-state snow mass without changing bulk snow albedo, and ice-albedo feedback amplifies this effect. Vertically-resolved snowpack heating reduces winter snow mass on the Tibetan Plateau by 80% in one GCM, and significantly increases 2 m air temperature. These changes significantly reduce model-measurement discrepancies. Our results demonstrate that snowpack radiative heating plays a significant role in regulating surface climate and hydrology. More accurate snowpack radiation has the potential to improve predictions of related climate processes, such as spring runoff and the Asian Monsoon.



## 2.2 Introduction

Net surface solar radiation often dominates the energy budget of snow melt processes in non-forested areas and hence influences snow thickness, extent, and surface albedo in many regions (*Molotch et al.*, 2004). Winter mean snowpack absorption can reach  $50 \text{ W m}^{-2}$  or more, depending on local insolation and snow age. Sophisticated snow and ice radiation models predict realistic vertical distributions of solar absorption (e.g., *Grenfell*, 1991; *Jordan*, 1991). However, general circulation models (GCMs) typically deposit all absorbed solar radiation in the top-most snow layer. Unrealistic representation of snow-radiation interactions may bias climate predictions in snowy regions, especially mid-latitude regions where insolation is relatively intense. *Foster et al.* (1996) analyzed seven GCMs and found a nearly ubiquitous over-prediction of snow depth in the Tibetan Plateau (TP) region ( $30 - 40^\circ\text{N}$ ,  $80 - 100^\circ\text{E}$ ). This paper identifies and assesses climatic implications of vertically-distributed snowpack heating in the TP region.

Accurate representation of snow physical processes on the TP are important for several reasons. The Blanford Hypothesis (*Blanford*, 1884) predicts that springtime TP snow quantity influences the South Asian Monsoon strength. *Fasullo* (2004) shows that in non-ENSO, strong-monsoon years there is a significant negative correlation between snow cover fraction over Tibet and the Himalayas during December–February (DJF) and Indian rainfall in the following June–September. Tibetan winter snow cover is also linked to summer rainfall over the Yangtze River Valley (*Wu and Qian*, 2003). Late spring snow cover constrains dust emissions from East Asia (*Kurosaki and Mikami*, 2004). Finally, snow melt and glacial melt-water on the TP help feed ten of Asia’s largest rivers, which bring freshwater to about one-half of Earth’s population.

## 2.3 Methods

Snowpack heating and reflectance are predicted with our two-stream, multi-layer SNow, ICe, and Aerosol Radiation model (SNICAR), based on *Wiscombe and Warren* (1980) and *Toon et al.* (1989). The present study neglects aerosol effects. Snow is treated as a collection of ice spheres, lognormally distributed in size, with number

median radii  $50 \leq r_n \leq 1000 \mu\text{m}$  and geometric standard deviation of 2.0. Mie parameters are computed off-line for one visible ( $0.3 - 0.7 \mu\text{m}$ ) and four near-infrared (NIR) ( $0.7 - 1.0$ ,  $1.0 - 1.2$ ,  $1.2 - 1.5$ , and  $1.5 - 5.0 \mu\text{m}$ ) spectral bands. This coarse spectral discretization yields vertical flux profiles within 10% of a 10 nm spectral grid. The NIR bands are combined into the single NIR band predicted by the host GCM weighted by a surface insolation distribution appropriate for mid-latitude winter, assuming 30% cloud coverage. *In situ* data on vertical profiles of radiative flux divergence in snowpacks are scarce (Warren, 1982). However, net downward flux from SNICAR is within  $\sim 15\%$  of measurements throughout the top meter of one snowpack (Schwerdtfeger and Weller, 1977).

SNICAR is implemented in the Community Land Model (CLM) Version 3 (Oleson *et al.*, 2004), the land component of the NCAR Community Atmosphere Model (CAM) Version 3 (Collins *et al.*, 2004). The snow physics represented in up to five layers include thermal diffusion, density increases from snow compaction, water flow, and vertically resolved melting and re-freezing. SNICAR replaces the original CLM snowpack radiative formulation, which bases snow albedo on an empirical function and constrains solar snowpack absorption to occur in the top 2 cm surface layer.

Table 2.1 summarizes the two sets of experiments performed. The off-line experiments force CLM with 1990–1999 atmospheric data from the National Center for Environmental Prediction (NCEP) reanalysis project (Kalnay *et al.*, 1996). These experiments are named CLM-X for model configuration “X”. In this uncoupled mode, precipitation and temperature from the lowest atmospheric level are fixed, which tightly constrains land surface climate. Coupled experiments (named CAM-X) use CLM coupled to the CAM3 atmosphere model forced with climate-mean sea surface temperatures. The A experiments use the original CLM snow radiation physics (pre-

TABLE 2.1. Numerical experiments

Off-Line Simulation	Coupled Simulation	Snow RT Model	Median Radius	Shortwave Absorption
CLM-A	CAM-A	CLM	—	Top Layer
CLM-B	CAM-B	SNICAR	$200 \mu\text{m}$	Top Layer
CLM-C	CAM-C	SNICAR	$200 \mu\text{m}$	All Layers
CLM-D	CAM-D	SNICAR	$100 - 1000 \mu\text{m}$	All Layers

scribed albedo, all absorption occurs in top snow layer). The B experiments predict surface albedo and vertically-resolved heating with SNICAR, then artificially move all snowpack absorption into the top snow layer. The C experiments predict snow reflectance and absorption as in B, and allow solar absorption to occur realistically in sub-surface layers. Mean optically-effective snow grain sizes range from  $50 - 1100 \mu\text{m}$  (e.g., *Painter et al.*, 2003). Experiments B and C predict snow radiative properties using a globally uniform snow radius  $r_n = 200 \mu\text{m}$ . This is consistent with sizes determined from field observations of slightly-aged, non-melting snow in Greenland (*Stroeve and Nolin*, 2002) and Japan (*Aoki et al.*, 2000). The D experiments preserve the snow aging characteristics of CLM with a simple snow age model, increasing  $r_n$  based on snow column temperature and time since last snowfall.

We compare model results to three observational snow depth datasets. First, the US Air Force Environmental Technical Applications Center (USAF/ETAC) assembled the only global snow depth climatology that is based on *in situ* measurements covering an annual cycle (*Foster and Davy*, 1988). The second dataset is snow depth derived from the Nimbus-7 Scanning Multi-channel Microwave Radiometer (SMMR) from Nov. 1978 to Aug. 1987 (*Chang*, 1995). The third dataset is based on Advanced Microwave Scanning Radiometer (AMSR-E) global snow water equivalent for 2003 (*Chang and Rango*, 2004). We converted AMSR-E snow water equivalent to snow depth using the mean TP snow density predicted by CLM ( $259 \text{ kg m}^{-3}$ ). Lastly, we compare coupled model air temperature results with the Willmott and Matsuura (WM) (*Willmott and Matsuura*, 2000) and Climate Research Unit (CRU) (*New et al.*, 1999) global observational datasets, and with NCEP re-analysis data (*Kalnay et al.*, 1996).

## 2.4 Results and Discussion

Off-line and coupled experiments in Table 2.1 were integrated for 10 and 15 yr, respectively. In Experiment D the rate of change in global annual mean snow depth is less than  $1 \text{ \% yr}^{-1}$  after six years and the net top-of-atmosphere radiative flux is  $+0.76 \text{ W m}^{-2}$  with no significant trend. All experiments were performed at T42

spatial resolution, approximately  $2.8^\circ \times 2.8^\circ$  near the equator. The defined TP region includes about 25 gridcells.

### 2.4.1 Model Sensitivity to Sub-Surface Snow Heating

SNICAR predicts a significantly more gradual solar radiative absorption profile in snow than CLM prescribes. Figure 2.1 compares the absorption profiles for a 10 cm snow column assuming TP climate-mean surface insolation of 135 and  $137 \text{ W m}^{-2}$  in the visible and NIR bands, respectively. SNICAR linearly stratifies snow density based on CLM predictions that density increases from 190 to  $590 \text{ kg m}^{-3}$  from the surface to 1 m depth. The fractional solar absorption that occurs below 2 cm (the top-layer thickness) with 50, 200, 500, and  $1000 \mu\text{m}$  radius snowpacks is 19%, 36%, 44%, and 47%, respectively. *Brandt and Warren* (1993) suggest about 44% of total solar absorption in an Antarctic snowpack occurs in the top 1 mm. SNICAR estimates about 38% of absorption in a 1 m snowpack occurs in the top 1 mm (assuming  $r_n = 100 \mu\text{m}$ ). Wavelengths longer than about  $1 \mu\text{m}$  are absorbed very close to the surface. Shorter wavelength radiation represents a small but significant fraction of the total absorbed radiation, and penetrates much deeper. Solar radiation penetrates deeper into larger-grained snowpacks. Experiment D accounts for snow grain growth.

Comparison of Experiments B and C isolates the climate effects of sub-surface snowpack heating. Figure 2.2 shows the mean change (C–B) in 2 m air temperature ( $T_{2\text{m}}$ ) for the off-line and coupled experiments. Table 2.2 summarizes changes in global land and TP snow depth,  $T_{2\text{m}}$ , and surface albedo for these experiments. The heating-induced 5 cm global-mean reduction in snow depth is mostly due to reduced snow accumulation over Greenland and Antarctica, which are perennially

TABLE 2.2. Global land and Tibetan Plateau (TP) change in snow depth, 2 m air temperature, and surface albedo caused by vertically-resolved snowpack solar absorption in an off-line land surface model and in a coupled land-atmosphere model.

	Snow Depth [m]		Air Temp [ $^\circ\text{C}$ ]		Sfc. Albedo	
	Global	TP	Global	TP	Global	TP
CLM: C–B	–0.05	–0.01	+0.03	+0.23	–0.002	–0.007
CAM: C–B	–0.05	–0.25	+0.10	+2.00	–0.005	–0.138

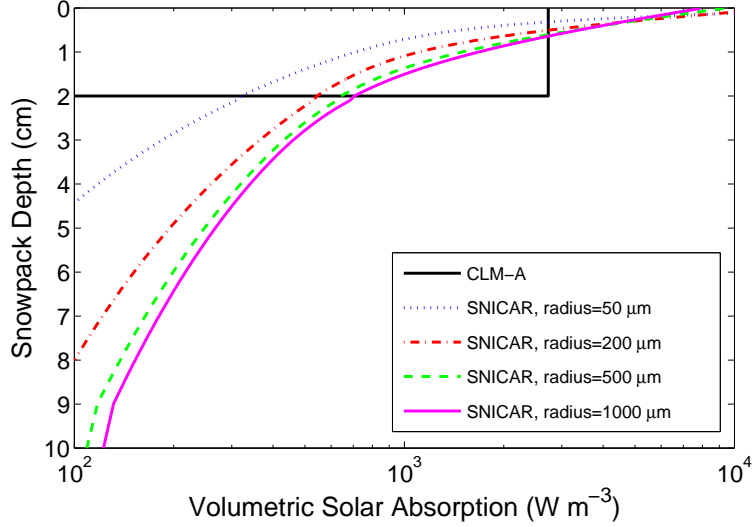


FIGURE 2.1. Solar absorption profiles prescribed by CLM and predicted by SNICAR.

snow-covered. Aside from the ice sheets, snow depth changes most over the TP, where snow thickness decreases by 25 cm in the coupled experiment. Local snowfall changed by less than 1%, implying that the snow thickness change is due entirely to increased snow melt and, to a lesser extent, sublimation. We attribute the increased snowmelt to intense wintertime insolation (owing to Tibet’s relatively low latitude) and subsequent sub-surface heating. The vertically distributed snowpack radiative absorption predicted by SNICAR and downward thermal diffusion in the C experiments cools the surface snow layer and warms all sub-surface snow layers relative to the B experiments, inducing sub-surface melting. Snow melt triggers atmospheric feedbacks (described below) that enhance snow melt.

The global mean  $T_{2m}$  warming in both experiments is small. In the coupled experiment, however, snowpack heating warms the TP by +2.0 °C, a highly significant regional change. Moreover, the TP is the only region where statistically significant warming occurs in the off-line experiment.

Table 2.2 shows that internal snowpack heating reduces surface albedo over the TP by 0.14 and 0.01 in the coupled and off-line experiments, respectively. The striking difference occurs because the coupled experiment allows the ice-albedo feedback mechanism to amplify snowpack-induced climate change over the TP. Snow melt reduces snow depth and therefore snow fraction. Reduced snow fractions expose darker surfaces which absorb more sunlight and, in the coupled experiments, warm the sur-

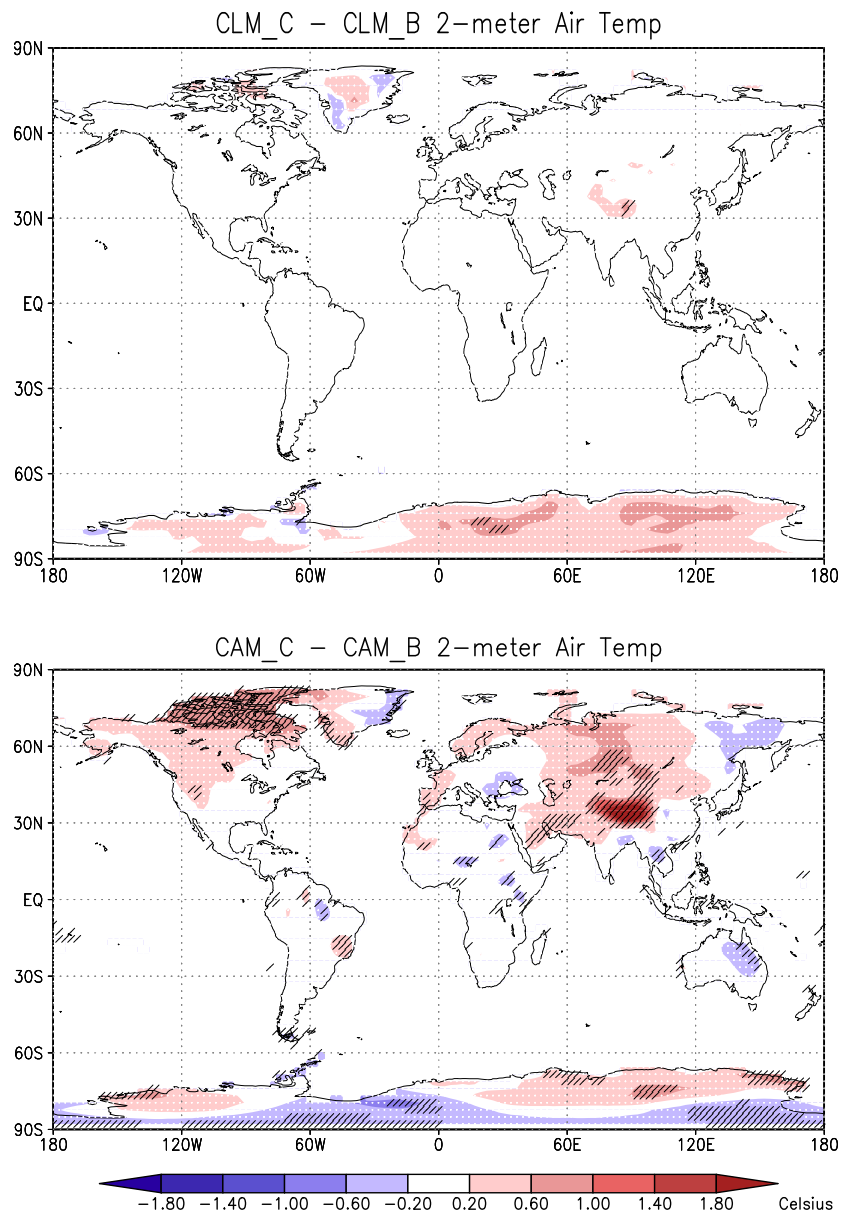


FIGURE 2.2. Climatological annual mean difference in 2m air temperature caused by sub-surface snowpack solar absorption in an off-line land model (top) and in a coupled land-atmosphere model (bottom). Hatching shows regions where differences are statistically significant at the 1% confidence level.

face air. The ice-albedo feedback loop completes as warmer surface air melts more snow. Mean maximum daily  $T_{2m}$  over the TP exceeds the melting temperature ( $0^{\circ}\text{C}$ ) from Apr–Nov with sub-surface heating, but only exceeds  $0^{\circ}\text{C}$  from May–Oct without sub-surface heating. Since bulk snow column albedo is identical in these experiments, the surface albedo reduction in Table 2.2 is due entirely to reduced snow cover and snow depth.

## 2.4.2 Model Comparison with Observation

Figure 2.3 shows seasonal snow depth from the three observational datasets, the original snow model experiments (CLM-A and CAM-A), and our most realistic experiments (CLM-D and CAM-D). While more realistic, the D experiments still neglect potentially significant effects such as absorbing aerosols and vertically-resolved snow grain size. Both microwave-derived datasets report greater snow depth during winter months than USAF/ETAC, which has less than 2 cm all year. Microwave retrievals overestimate snow mass on the TP by roughly a factor of two because the thin surface atmosphere requires a unique retrieval algorithm which has not been applied, and because seasonally frozen ground produces a snow-like microwave signature (R. Armstrong, personal communication, 2004). Furthermore, large errors persist with detection over mountainous terrain and shallow snow (*Chang and Rango, 2004*). USAF/ETAC may slightly underestimate snow depth because all ground measurements in the TP were made in low valleys.

The off-line experiments are forced with realistic winter precipitation and they predict mean TP Dec–Apr snow depths of 2.3 and 4.7 cm with and without internal snowpack radiative heating (CLM-D and CLM-A, respectively). Likewise, the coupled experiments (CAM-D and CAM-A) predict 8.9 and 55 cm, respectively. The off-line model changes in snow depth are within the margin of uncertainty of our observational data. CAM-A significantly over-predicts winter precipitation on the TP relative to observations (*Willmott and Matsuura, 2000*). Internal heating and atmospheric warming greatly reduce snow mass, but a slight high bias persists due to excessive snowfall. Further comparison of the coupled experiments with USAF/ETAC data shows that regional snow depth prediction elsewhere is slightly improved or no

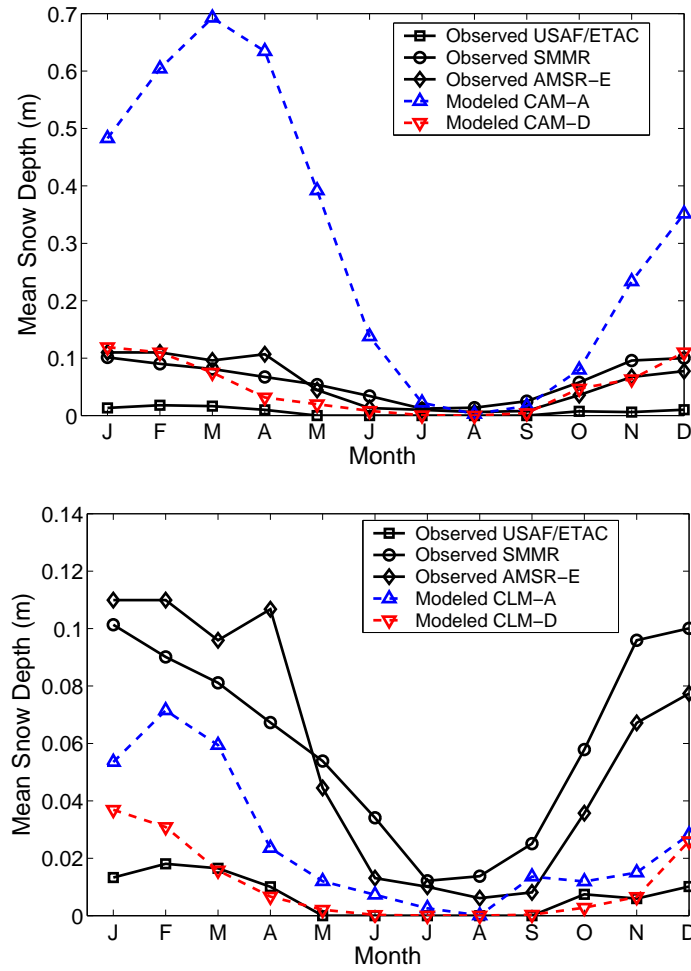


FIGURE 2.3. Annual cycle of observed and simulated snow depth over the Tibetan Plateau. (top) Coupled experiments. (bottom) Off-line, land-only experiments.



worse using SNICAR with snow aging relative to the A experiments. In particular, snowpack radiative heating slightly improves simulated annual mean snow depth over the Western U.S. and Eastern Siberia.

Finally, Figure 2.4 shows the seasonal cycle of  $T_{2m}$  over the TP from observations and from Experiments CAM-A and CAM-D. WM and CRU data are climatologies based on station data and interpolations which account for elevation changes, averaged over 1950–1996 and 1961–1990, respectively. The interpolation technique is important due to the sparseness of TP observations. NCEP assimilates model and observational data and, due to sparse  $T_{2m}$  TP observations, is probably strongly influenced by the model (*Kalnay et al.*, 1996), which may have snow biases similar to CAM-A. Global mean  $T_{2m}$  is  $0.14^{\circ}\text{C}$  warmer with vertically-resolved snowpack heating and snow aging relative to CAM-A, and is  $2.1^{\circ}\text{C}$  warmer over the TP. CAM-D agrees well with WM and CRU data. NCEP data are colder and closer to CAM-A than CAM-D from Mar–Jul. The largest discrepancies occur in spring, when CAM-A grossly overpredicts snow depth. We expect the more realistic snow depth predicted by CAM-D to improve  $T_{2m}$  prediction. However, CAM-D appears to over-predict  $T_{2m}$  from Dec–Feb.

## 2.5 Conclusions

We used a hierarchy of radiative transfer, off-line land surface, and coupled land-atmosphere climate models to investigate the sensitivity of Tibetan Plateau (TP) climate to sub-surface absorption of solar radiation in snowpacks. Vertically resolving solar heating in snowpacks does not necessarily alter snowpack reflectance, and shows that 20 – 45% of solar absorption by snow occurs beneath 2 cm. This sub-surface heating significantly alters snowpack evolution and atmospheric warming amplifies snowpack changes via the ice-albedo feedback mechanism. Representing vertically-resolved snowpack heating significantly improves predicted snow depth and 2 m air temperature over the Tibetan Plateau in one coupled land-atmosphere model. It will be interesting to see if other climate models behave similarly.

More physically-realistic snow models such as SNICAR could improve understand-

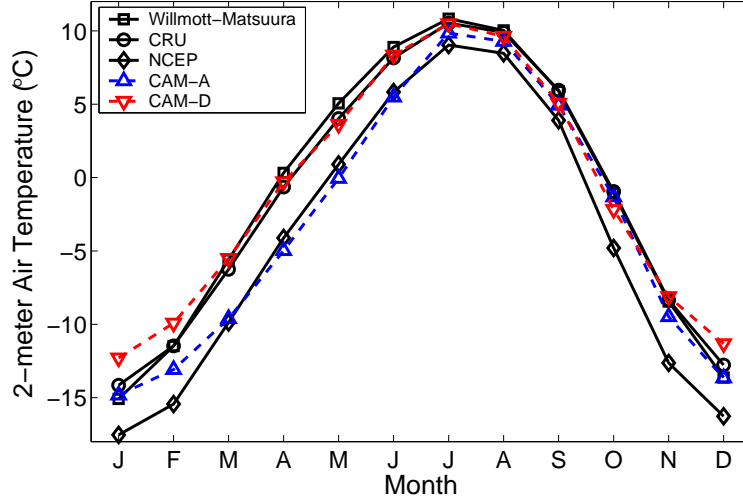


FIGURE 2.4. Annual cycle of observed and simulated 2 m air temperature over the Tibetan Plateau.

ing of phenomena related to TP snow cover, such as the South Asian Monsoon and the timing and intensity of spring surface run-off. More work is needed to understand the evolution of snow grain size with time and temperature, the relationship between snow depth and snow fraction, and the effect of absorbing aerosols on snow reflectance and heating. The strong sensitivity of TP climate to internal snowpack heating suggests that dark aerosols may play important roles in snowpack hydrology.

## 2.6 Acknowledgments

We thank R. Armstrong, R. Dickinson, K. Oleson, T. Painter, M. Vertenstein, S. Warren, Z.-Liang Yang and two anonymous reviewers for their help and insightful comments. Satellite snow data were obtained from the National Snow and Ice Data Center (<http://nsidc.org>).

# CHAPTER 3

## Linking Snowpack Microphysics and Albedo Evolution

As appears in:

Flanner, M. G., and C. S. Zender (2006), Linking snowpack microphysics and albedo evolution, *J. Geophys. Res.*, *111*, D12208, doi:10.1029/2005JD006834.

### 3.1 Abstract

Snow aging causes reflectance to vary significantly on timescales of days. This variability influences the strength of snow-albedo feedback, and can affect the timing of snowmelt. However, climate models have yet to incorporate important controls on snow aging and albedo evolution. We develop a physically-based model that predicts evolution of dry, pure-snow specific surface area, and apply aspherical ice particle theory to link these results with albedo evolution. This is the first theoretical study to quantify the relative roles of initial size distribution, vertical temperature gradient, and snow density in snow albedo evolution. Vapor diffusion caused by curvature differences causes rapid albedo decay in the first day following snowfall. Vertical temperature gradient generally dominates grain growth processes afterward, but is modulated by snow density, irregularity in particle spacing, and temperature. These

processes operate as a coupled system, which we uniquely represent without abrupt transitions between regimes.

Model results agree very well with measurements of isothermal snow evolution, and are within reasonable range of temperature gradient observations. We show that different snow state regimes cause albedo of non-melting snow surfaces with identical initial albedo to vary by 0.12 or more after 14 days. Lack of quality observational data illuminates the need for well-controlled snow studies that simultaneously monitor specific surface area, temperature gradient, and albedo. Accounting for snow aging processes, especially temperature gradient, will improve understanding and assessment of snow albedo feedback and climate sensitivity. The modeling framework we develop will also be useful for air-snow chemistry studies that consider specific surface area.

## 3.2 Introduction

The land surface plays an integral role in the planetary radiation budget. Snow is highly reflective and changes to its optical properties and spatial coverage modulate climate through snow-albedo feedback (e.g., *Budyko*, 1969; *Yang et al.*, 2001). Slight changes in snow reflectance can double or halve the absorbed radiation, and many studies show snow to be a rapidly evolving medium (e.g., *McGuffie and Henderson-Sellers*, 1985; *Aoki et al.*, 2003; *Pirazzini*, 2004). This evolution is an important consideration in global climate models (GCMs), where energy estimation errors due to poor radiative representation can affect the timing of snowmelt and then amplify biases through snow-albedo feedback (*Flanner and Zender*, 2005).

Previous studies account for the role of grain growth on albedo evolution only with empirical representations (e.g., *Verseghy*, 1991; *Marshall and Oglesby*, 1994; *Douville et al.*, 1995; *Loth and Graf*, 1998). *Marshall* (1989) parameterizes snow albedo for use in climate models, including a description of the evolution of snow grain size in dry and melting snow. The parameterization describes a constant growth rate for the first two weeks after snowfall, based on limited grain-size measurements in polar, surface snow (*Stephenson*, 1967; *Warren et al.*, 1986). Lack of observational data

at the time prohibited her from deriving a temperature-dependence for grain growth during this initial growth phase. Using model results and recent observations, we will show that initial grain growth is non-linear and depends on snowpack temperature, initial size distribution, vertical temperature gradient (TG), and snow density.

Three recent studies demonstrate that representing ice media composed of non-spherical particles with a collection of spheres that conserves the total volume and total surface area (but not the total number of particles) yields predictions of hemispheric radiation fluxes typically within about 5% accuracy (*Grenfell and Warren, 1999; Neshyba et al., 2003; Grenfell et al., 2005*). Suggested in earlier works (*Bryant and Latimer, 1969; Wiscombe and Warren, 1980; Pollack and Cuzzi, 1980*), this *equal-V/S* theory paves the way for an extremely powerful simplification that can be utilized when considering snow albedo evolution in GCMs, where generally only hemispheric fluxes are considered. It implies that if the specific surface area (SSA,  $\hat{S}$ , units of surface area per mass) of a snowpack is known, the snow can be represented optically with a collection of spheres, or effective radius ( $r_e$ ), that conserves the snow’s volume to surface area ratio, regardless of the snow’s crystal habits. While this theory is of less use when directional reflectance is an important consideration (e.g., *Dozier, 1989; Painter and Dozier, 2004*), it can be utilized for estimation of the column energy budget in climate models. In support of this theory, we have found that snow reflectance predicted by different lognormal distributions of spheres which have the same volume to surface area ratio (but different mean radii,  $\bar{r}$ ) are nearly identical over the entire solar spectrum.

Mean grain size of snowpacks generally increases with time, reducing albedo, especially in the near-infrared (near-IR) spectrum (e.g., *Wiscombe and Warren, 1980*). Following snowfall and immediate mechanical deformation (*Jordan, 1991*), five primary processes govern the evolution of grain size. First, differences in curvature of the particles cause slight vapor density gradients via Kelvin’s Law (e.g., *Colbeck, 1980; Arons and Colbeck, 1995*). This process operates in isothermal snow, and can dominate grain growth on short timescales in fresh snow. Second, macroscopic TG in the snow causes sharp inter-granular vapor density gradients and bulk vapor diffusion through the ice matrix (e.g., *Marbouty, 1980; Colbeck, 1983a; Gubler, 1985; Sturm and Benson, 1997*), inducing *temperature gradient growth*. Third, snow subject to melting

and refreezing experiences very dynamic growth as liquid  $\text{H}_2\text{O}$  is redistributed among the grains. Fourth, wind ventilation in surface snow also transports vapor. Finally, theory (*Zhang and Schneibel, 1995; Colbeck, 2001*) and recent observations using scanning electron microscopy (*Rosenthal et al., 2006*) indicate that sintering may be an important mechanism for reducing snow SSA in low TG environments. We treat the first two effects in this study. We will utilize empirical representations of wet snow metamorphism (*Brun, 1989; Marshall, 1989*) for future model development.

Snow albedo can also be strongly influenced by the accumulation of absorbing aerosols such as dust or soot (e.g., *Warren and Wiscombe, 1980; Hansen and Nazarenko, 2004*). We neglect aerosols here, although the current study is a necessary precursor to understanding soot-albedo forcing because of the sensitivity of the forcing to snow grain size (*Warren and Wiscombe, 1980*). In a coupled snow-aerosol model, aerosols will influence snow heating rates and affect grain growth through physically-realistic means.

The goal of this study is to apply basic microphysical principles to predict the evolution of dry snow SSA. Combined with *equal- $V/S$*  theory, this will facilitate more realistic representation of snow albedo evolution. We prescribe snow temperature, temperature gradient, and density, which are all prognostic variables in many land surface models (e.g., *Oleson et al., 2004*). Thus, our microphysical module could be coupled to existing snow climate models (e.g., *Jordan, 1991*) without changing the bulk thermodynamics. Developing a full thermodynamic snow model is beyond the scope of this study. Our parameterization will be constrained by observation, and be suitable for snowpack studies across a range of spatial scales.

### 3.3 Theory and Methods

Vapor diffusion causes complex morphological changes to snow grains, forming intergranular bonds, faceted depth hoar crystals, and other complex shapes (e.g., *Sturm and Benson, 1997*). Several studies have attempted to model dry snow metamorphism, accounting for some shape evolution in order to understand mechanical and thermal snow properties, with a motivation of understanding avalanche forma-

tion (*Gubler, 1985; Brown et al., 2001; Lehning et al., 2002*). Because our goal is to predict evolution only of snow SSA and albedo, we adopt a more simplified approach to understanding grain growth, developing a one-dimensional representation of a collection of ice spheres.

Snow aging enhances our SNow, ICe, and Aerosol Radiative (SNICAR) model (*Flanner and Zender, 2005*), which represents radiative transfer in the snowpack. SNICAR is a multi-layer two-stream model based on *Wiscombe and Warren (1980)* and *Toon et al. (1989)* that treats snow as a collection of ice spheres. It obtains Mie parameters (single scattering albedo, extinction coefficient, and asymmetry parameter) for any lognormal size distribution from a lookup table computed offline. The model depends on vertically-resolved effective radius ( $r_e$ ), solar zenith angle, snow depth and density, direct and diffuse incident radiation, bare surface reflectance, and concentrations of absorbing impurities. We use 470 radiative bands in the solar spectrum (0.3–5.0  $\mu\text{m}$ ). In this study, we assume direct and diffuse incident fluxes that are typical of mid-latitude winter.

### 3.3.1 Curvature Growth

We begin with general theory of diffusional growth of spherical ice particles. All symbols discussed here are listed in Appendix A. Fick’s Law, in the absence of any convection, describes diffusion of vapor through air in the presence of a vapor density gradient,  $d\rho_v/dz$  as:

$$J_v = -D_v \frac{d\rho_v}{dz} \quad (3.1)$$

where  $D_v$  is the diffusivity of water vapor in air and is dependent on temperature (*Pruppacher and Klett, 1998*). A convection term (simply wind vector multiplied by vapor density) is sometimes included in Equation 3.1, but we neglect it in this study because of large uncertainty about circulation processes within the snowpack. We note, however, that wind has competing effects on albedo evolution. High sublimation rates and delayed settling of the finest suspended crystals from wind-entrained snow leave a surface composed of small crystals (*Grenfell et al., 1994*). Conversely, wind accelerates grain growth by circulating vapor quickly through surface snow (*Cabanes et al., 2003*).

Assuming an ambient vapor density,  $\rho_{v,amb}$  and vapor density  $\rho_{v,s}$  at the particle surface, the steady-state concentration profile at radial distance  $x$ , derived from the diffusion equation, is (e.g., *Seinfeld and Pandis*, 1998):

$$\rho(x) = \rho_{v,amb} - \frac{r}{x}(\rho_{v,amb} - \rho_{v,s}) \quad (3.2)$$

where  $r$  is the particle's radius. The mass growth rate of a particle is:

$$\frac{dm}{dt} = 4\pi r^2 D_v \left( \frac{d\rho_v}{dx} \right)_{x=r} \quad (3.3)$$

Combining Equations 3.2 and 3.3, we get the general form of the steady-state growth equation for motionless aerosols employed in cloud and snow physics (e.g., *Colbeck*, 1983a; *Pruppacher and Klett*, 1998; *Seinfeld and Pandis*, 1998):

$$\frac{dm}{dt} = 4\pi r D_v (\rho_{v,amb} - \rho_{v,s}) \quad (3.4)$$

The difference between ambient vapor density and vapor density at the particle surface drives growth or sublimation of the ice particle. In the continuum regime,  $\rho_{v,s}$  is assumed to be in constant equilibrium with the particle surface during growth because growth progresses hundreds of times more slowly than diffusion to the particle surface (*Seinfeld and Pandis*, 1998). *Colbeck* (1983b) also discusses why surface kinetic effects are small. Thus, neglecting any solute effects,  $\rho_{v,s}$  is a function only of particle temperature and radius of curvature. For non-spherical ice shapes, the term  $4\pi r$  may be replaced with an equivalent 'capacitance' for the shape, derived from electrostatic theory (e.g., *Pruppacher and Klett*, 1998), but these solutions are non-trivial (*Chiruta and Wang*, 2003).

Kelvin's Law demonstrates that equilibrium vapor pressure over curved surfaces exceeds that over planar surfaces (e.g., *Pruppacher and Klett*, 1998):

$$p_s(r, T) = p_{eq} \exp \left( \frac{2\gamma}{R_v T \rho_i r} \right) \quad (3.5)$$

where  $p_{eq}$  is the saturation vapor pressure over a planar surface,  $\gamma$  the surface tension of ice against air,  $R_v$  the specific gas constant for vapor,  $T$  the system temperature, and  $\rho_i$  the density of ice. We use  $\gamma = 0.109 \text{ J m}^{-2}$  from *Pruppacher and Klett* (1998). Corresponding vapor density can be easily found with the Ideal Gas Law. The surface saturation ratio ( $p_s/p_{eq}$ ) is only about 1.021 and 1.002 for  $r = 0.1 \mu\text{m}$  and  $r = 1 \mu\text{m}$ ,



respectively, and is very close to 1 for  $r > 10\mu\text{m}$ . While such small grain sizes are atypical of snow, fresh snow typically has branch dendrites with sharp curvature. Thus the Kelvin Effect is an important consideration in fresh snow (*Colbeck*, 1980, 1983a), but otherwise does not contribute to significant vapor density gradients.

As sublimation or condensation occurs on a particle, latent heat is released or absorbed, altering the particle temperature. This temperature change has the effect of slowing both sublimation and condensation rates. An analytic approximation is derived for a particle’s mass rate of change which accounts for the latent heat effect (e.g., *Rogers and Yau*, 1994; *Seinfeld and Pandis*, 1998). We define it here in terms of the environmental vapor pressure  $p_{amb}$ :

$$\frac{dm}{dt} = \frac{4\pi r \frac{p_{amb} - p_s(r, T)}{p_{eq}}}{\left(\frac{L}{R_v T} - 1\right) \frac{L}{KT} + \frac{R_v T}{p_{eq} D_v}} \quad (3.6)$$

where  $K$  is the temperature-dependent thermal conductivity of air (*Seinfeld and Pandis*, 1998), and  $L$  is the latent heat of sublimation. Relative to Equation 3.4, this approximation predicts differences in SSA of only about 4% after 14 days.

The key challenge, especially for TG conditions, is the determination of  $p_{amb}$ . We do not know of any measurements of relative humidity inside the snowpack. But air in surface snow is well-mixed with the lower atmosphere, and thus likely has a similar vapor density. Indeed, seasonal sublimation totaling 15% of snowfall is observed in the Colorado Front Range (*Hood et al.*, 1999). During night, vapor saturation can induce frost deposition of small, ornate crystals, brightening the surface (*Pirazzini*, 2004). In sub-surface snow, we expect the interstitial pore space to be consistently near saturation, given the high density of solid surface. In a coupled snow-atmosphere model,  $p_{amb}$  could be predicted for surface snow from atmospheric conditions. But in this model we assume it is a volume-weighted mean of the equilibrium vapor pressures of all snow grains, as suggested by *Adams and Brown* (1982, 1983):

$$p_{amb} = \int_0^\infty p_s(r, T) r^3 P(r) dr \quad (3.7)$$

where  $P(r)$  is the probability density function of particles with radius  $r$ . As we will see later, this formulation also facilitates a consistent representation of TG growth.

For typical size distributions of snow grains, this weighted-mean predicts mean pore vapor pressure slightly greater than equilibrium with respect to planar ice. Thus,

the smallest grains sublime, while larger grains slowly grow. This formulation does not conserve mass (total ice mass only decreases with time, however), but as described earlier, the goal of this model is to predict SSA evolution using prescribed snow state variables. Furthermore, modeling the system as a closed-box is made difficult by the fact that ice mass is about five orders of magnitude greater than vapor mass for typical snow density and temperature. We found that preventing numerical oscillations in pore vapor pressure requires model timestep on the order of  $10^{-4}$  s, starting from non-equilibrium conditions. In reality, however, sublimated vapor slightly raises local pore vapor pressure, inducing deposition on neighboring surfaces, including concave necks that bond sintered grains (*Miller, 2002; Miller et al., 2003*). Incorporation of geometry with negative radius of curvature would enhance the Kelvin Effect. But the geometry suggested by *Miller (2002)* predicts concave ice volume that is a very small fraction of total ice volume, and would hardly affect  $p_{amb}$  with our formulation.

We assume a lognormal distribution of grain radii with initial geometric standard deviation  $\sigma_g$  and number-median radius  $r_n$ :

$$n(r) = \frac{1}{\sqrt{2\pi} r \ln(\sigma_g)} \exp \left[ -\frac{1}{2} \left( \frac{\ln(r/r_n)}{\ln(\sigma_g)} \right)^2 \right] \quad (3.8)$$

where  $n(r)$  is scaled to the probability density function  $P(r)$ . Our parameter of interest is  $\hat{S}$ , which is simply total surface area of the particle ensemble divided by total mass:

$$\hat{S} = \frac{3 \int_0^\infty r^2 P(r) dr}{\rho_i \int_0^\infty r^3 P(r) dr} \quad (3.9)$$

Similarly, effective radius, which drives the radiative transfer model, is also a surface area-weighted radius of the ensemble, and is directly related to  $\hat{S}$  for any collection of particles as:

$$r_e = \frac{3}{\rho_i \hat{S}} \quad (3.10)$$

Finally,  $r_n$  is related to  $r_e$  for a lognormal distribution as:

$$r_n = r_e \exp \left[ -\frac{5}{2} \ln(\sigma_g^2) \right] \quad (3.11)$$

The initial size distribution determines the ensemble growth rate. Broad distributions with small median radii grow quickly as small particles completely sublime,

and monodisperse distributions do not evolve at all. Small size bins disappear permanently when all of their mass sublimates, and the distribution becomes non-lognormal. Assuming a broad distribution of  $r$  for fresh snow hopefully captures realistic range of surface curvatures.

### 3.3.2 Temperature Gradient Growth

Temperature gradient growth is a complex and poorly understood phenomenon. General observations of particle growth rates under TG are that they:

1. increase with increasing TG (*Marbouty*, 1980; *Fukuzawa and Akitaya*, 1993), probably up to some limiting value.
2. increase with increasing temperature (*Marbouty*, 1980), and have little dependence on TG at low temperatures (*Kamata et al.*, 1999)
3. increase with decreasing snow density (*Marbouty*, 1980; *Sokratov*, 2001; *Schnee-  
beli and Sokratov*, 2004)
4. decrease with time and increasing particle size (*Sturm and Benson*, 1997; *Baunach et al.*, 2001)

Our approach captures these observations and represents curvature and TG growth in a unified manner. If we assume saturated pore vapor pressure along the temperature gradient axis, we can solve Equation 3.1 for  $d\rho_v/dz$  in terms of the temperature gradient  $dT/dz$  to get the macroscopic vapor flux (*Baunach et al.*, 2001):

$$J_v \left( T, \frac{dT}{dz} \right) = -D_v \frac{p_{eq}(T)}{R_v T^2} \left[ \frac{L}{R_v T} - 1 \right] \frac{dT}{dz} \quad (3.12)$$

$dT/dz$  is sign-dependent, but we always refer to it as positive in this study because of model symmetry along the TG axis. Conservation of mass requires that:

$$\frac{dJ_v}{dz} = -\frac{d\rho_v}{dt} \quad (3.13)$$

Microphysical studies either assume  $dJ_v/dz = d\rho_v/dt = 0$  (e.g., *Adams and Brown*, 1983; *Gubler*, 1985), or just  $d\rho_v/dt = 0$  (*Baunach et al.*, 2001; *Lehning et al.*, 2002).

The latter studies predict a vertical flux divergence, but conserve mass by depositing all excess vapor, equaling  $dJ_v/dz \times \Delta z$ , as ice. With this assumption, the densification of snow ( $d\rho_s/dt$ ) equals the divergence in vertical flux, and is proportional to both  $d^2T/dz^2$  and  $(dT/dz)^2$  (*Giddings and LaChapelle*, 1962). This approach was used by *Sturm and Benson* (1997) to calculate relative minima and maxima density positions in sub-Arctic snowpack, assuming measured temperature profiles.

Applying this theory to grain growth, however, by distributing the excess vapor to available grains in any reasonable way, under-predicts grain growth by 1–2 orders of magnitude. Deficiency in this macroscopic approach suggests that vapor flux must occur on very small (i.e., inter-particle) spatial scales. Evidence for this comes from measurements indicating that water molecules composing individual grains must sublime and re-deposit many times over during the course of a winter (*Sturm and Benson*, 1997). Presumably, this deficiency is also why *Baunach et al.* (2001) and *Lehning et al.* (2002) add an intra-lattice vapor flux to their vertical flux divergence term in the Swiss SNOWPACK model. Realizing that interparticle vapor flux is required to achieve observed growth rates, early modeling studies have considered coupled source-sink particle configurations analogous to electrostatic capacitors (*Colbeck*, 1983a,b; *Sommerfeld*, 1983; *Gubler*, 1985; *Colbeck*, 1993).

Because ice conducts heat about 100 times more efficiently than air (*Giddings and LaChapelle*, 1962), we expect temperature gradient to be enhanced across the pore, relative to the macroscopic gradient. Therefore, the top of a grain will tend to be warmer than its environment, and the bottom colder, causing growth from the bottom and sublimation from the top. Observations of grains with rounded tops and faceted bottoms support this theory (*Colbeck*, 1983a; *Sturm and Benson*, 1997). But if we consider regular spacing between grains in a uniform vapor gradient field, all grains should have almost zero net growth resulting from TG (the only growth resulting from the slow, bulk vapor flux, Eq. 3.12). The importance of irregular spacing for particle growth has been recognized (*Colbeck*, 1983a; *Sommerfeld*, 1983; *Gubler*, 1985). Observations that only about 1 in 10 grains survive a season in a large temperature gradient (*Sturm and Benson*, 1997) offer strong evidence of preferential growth sites and competition for vapor. Observations of the largest crystals being surrounded by greater pore volumes (*Akitaya*, 1974; *Colbeck*, 1983a) imply greater

vapor source for these particles and offer further evidence for the importance of particle spacing. Presumably, this is also why lower density snow experiences more rapid growth (*Marbouty*, 1980; *Fukuzawa and Akitaya*, 1993). Realizing the importance of irregularly-spaced particles for growth, it is not surprising that growth occurs faster in greater temperature gradients (*Marbouty*, 1980; *Fukuzawa and Akitaya*, 1993), as enhanced vapor density gradients accentuate minute advantages in grain positioning. These realizations helped motivate the early capacitor models, but they have the burden of manually designating source and sink particles.

In reality, the net growth or decay experienced by a particle depends on the sum contributions from all pore vapor sources/sinks. Our model assumes a single pore source/sink for each particle which accounts for all sources and sinks. To achieve this, we assign a single particle-pore distance vector,  $\vec{h}$ , to each particle, representing the vector sum of all particle-pore distances along the TG axis. Neglecting the Kelvin Effect, the sign of  $\vec{h}$  determines growth or sublimation, and the magnitude determines mass rate of change, as greater spacings imply greater vapor pressure differences. In a regular-packed lattice,  $\vec{h}$  would be zero for every particle because each particle would have equally-strengthened sources and sinks (again neglecting the small bulk flux from Equation 3.12), and only curvature growth would occur. To account for heterogeneous particle positioning, we synthesize Gaussian distributions of  $\vec{h}$  for each particle size, with means equal to zero.

But what is the standard deviation of  $\vec{h}$ ? It is directly related to interparticle spacing variability, but lacking observations of such, we define a tunable parameter,  $\phi$ , representing the degree of irregularity in particle packing, to scale the standard deviation of  $\vec{h}$  to the mean particle spacing,  $\bar{a}$ . The mean spacing between particle boundaries depends on snow density ( $\rho_s$ ) and particle size as:

$$\bar{a}(r, \rho_s) = \left( \frac{4\pi r^3 \rho_i}{3\rho_s} \right)^{1/3} - 2r \quad (3.14)$$

These ideas conform with *Colbeck* (1993), who considers distributions of the normalized quantity  $(a + 2r)/r - 2$ . If we assume the same distribution of this quantity applies to all particle sizes, then mean spacing and standard deviation are related by the same scalar quantity for every particle size. With these arguments, we define a Gaussian probability density function of  $\vec{h}$ , given particle size and snow density,

$P(\vec{h}|r, \rho_s)$ , which has zero mean and standard deviation  $\phi \bar{a}$ . We can see that  $\bar{a} \rightarrow 0$  as  $\rho_s/\rho_i \rightarrow \pi/6$ . Therefore, TG growth ceases at the limit  $\rho_s = 480 \text{ kg m}^{-3}$ . Snow densities this high are rare in seasonal snowpack. Our limit is greater than the observed limit of  $350 \text{ kg m}^{-3}$  for TG growth forms (Marbouty, 1980), but our model predicts very slow growth at high densities.

Having defined a representative particle-pore parameter  $\vec{h}$ , we assume the pore vapor density is the mean of the equilibrium vapor densities at the top and bottom of the pore (Adams and Brown, 1982, 1983; Colbeck, 1983b). This stems from the assumption that, on small spatial scales,  $dJ_v/dz = 0$ , and therefore, neglecting minuscule change in  $D_v$ ,  $d^2\rho_v/dz^2 = 0$  (Equations 3.1 and 3.13). Considering non-zero values of these terms, however, would alter our growth rates very little, as described above. Maintaining consistency with our curvature model, the equilibrium vapor densities at either pore boundary are also volume-weighted means of the ensemble of particle equilibrium vapor densities (Adams and Brown, 1982, 1983). Then, the ambient pore vapor pressure, respective to each particle size and particle-pore spacing, is:

$$p_{amb}(r, \vec{h}) = \frac{1}{2} \left( T - \vec{h} \frac{dT}{dz} \right) \left[ \frac{\int_0^\infty p_s(r, T) r^3 P(r) dr}{T} + \frac{\int_0^\infty p_s \left( r, T - 2\vec{h} \frac{dT}{dz} \right) r^3 P(r) dr}{T - 2\vec{h} \frac{dT}{dz}} \right] \quad (3.15)$$

Note that  $\vec{h}$  designates vertical distance from pore center to particle center (rather than particle boundary) to account for the enhanced TG across the pore (Colbeck, 1983a), discussed above. Particle centers and pores at the same vertical level ( $\vec{h} = 0$ ) are at the same temperature, and no vapor diffuses between them. With a TG of zero, Equation 3.15 reduces exactly to Equation 3.7, irrespective of grain size. Thus, we have a unified expression for ambient vapor pressure that includes the Kelvin Effect and TG effects. With  $p_{amb}$  determined, Equation 3.6 drives the growth or sublimation of all particles. While the mean particle-pore spacing is zero for all particle sizes, appreciable growth of the ensemble occurs because the sublimating particles disappear completely, leaving behind only growing ones. In the studies described below, we use a timestep of 3600 s, 200 size bins, and 40 spacing bins per size bin.

## 3.4 Results and Discussion

In this section we compare predictions by SNICAR with observations of isothermal snow SSA evolution and grain size evolution in snow with temperature gradient. Then, we show dependence of snow albedo evolution on snow properties, and compare SNICAR albedo with one 10-day observational timeseries. Finally, we discuss a simple and effective parameterization of SSA evolution suitable for climate models and air-snow chemistry studies (e.g., *Domine and Shepson, 2002*).

### 3.4.1 Isothermal SSA Evolution

We first compare model predictions of isothermal growth with recent controlled laboratory experiments from *Legagneux et al. (2004)*. They gathered snow as it was falling and stored it at liquid nitrogen temperatures to prevent grain growth before measurement. During the experiment, they kept the snow uniformly at  $-15^\circ\text{C}$ , and observed SSA evolution by measuring methane adsorption. They provide a physical basis for representing time-dependent SSA with an equation of the form:

$$\hat{S}(t) = \hat{S}_0 \left( \frac{\tau}{t + \tau} \right)^{(1/\kappa)} \quad (3.16)$$

where  $\hat{S}_0$  is the initial SSA, and  $\tau$  and  $\kappa$  are empirical parameters. As we show later, this function also robustly fits model predictions over a range of temperature, TG, and density.

We compare measurement and model results using different initial size distribution widths ( $\sigma_g$ ). *Legagneux et al. (2004)* provide best-fit parameters of Equation 3.16 for their measurements, which we reproduce in Table 3.1. We set  $\hat{S}_0$  and  $T$  to match

TABLE 3.1. Parameters  $\hat{S}_0$ ,  $\kappa$ , and  $\tau$  for observations of fresh snow evolution from Table III of *Legagneux et al. (2004)*

Sample	$\hat{S}_0(\text{m}^2 \text{ kg}^{-1})$	$\tau(\text{hours})$	$\kappa$
1	87	7.1	4.6
2	100.7	10.2	3.6
3	59.2	12.5	4.1

the snow samples. Figure 3.1 shows model results against observation for their three fresh snow samples. SNICAR reproduces observed SSA decay from samples 1 and 2 quite well using  $\sigma_g = 2.3$ , but struggles to capture the long-term decay manifested in sample 3. Our choices of  $\sigma_g$  are within reasonable range of observed  $\sigma_g$ . Using data provided by Teruo Aoki, we fit lognormal distributions to measurements of thousands of snow grains from four different snow samples (Aoki *et al.*, 2000). The best-fit values of  $\sigma_g$  for the four collections are 1.75, 1.80, 1.78, and 2.20. The snow studied by Aoki *et al.* (2000) was at least a day old, however, and we expect the size distribution to narrow with time, as small grains disappear. We also expect real variability in  $\sigma_g$  for fresh snow. Furthermore, we implicitly account for any sintering with our choice of  $\sigma_g$ . Finally, we are likely accounting for the greater range of *curvatures* in real, aspherical grains by assuming a broader distribution of spherical grains. The robustness of modeling SSA evolution with spheres must be tested against observations under variable snow temperatures though.

Conditions which favor rapid curvature growth are wide size distributions of small particles. In Figure 3.1, SSA decreases rapidly during the initial day or two following snowfall, and subsequently tapers off as the distribution narrows and mass becomes concentrated with larger grains. Grain growth in the first two days has a strong dependence on  $\sigma_g$ , while growth after about day 3 has little dependence on  $\sigma_g$ . These model results are also supported by observations of temporal decrease in grain curvature of fresh snow (Fierz and Baunach, 2000).

### 3.4.2 Temperature Gradient Evolution

Snow can be subject to TG well in excess of  $100 \text{ K m}^{-1}$  (Fukuzawa and Akitaya, 1993; Sturm and Benson, 1997). Cold, clear-sky nights favor large gradients, as strong radiative emission cools the snow surface more than the lower atmosphere, while snow at depth can remain near the melting temperature. With a goal of understanding avalanche formation, several studies have measured grain growth of high density, large-grained snow (characteristic of basal snow) subject to large TG over long time-periods (Marbouty, 1980; Sturm and Benson, 1997; Baunach *et al.*, 2001; Lehning *et al.*, 2002). These conditions induce depth-hoar formation, which is mechanically



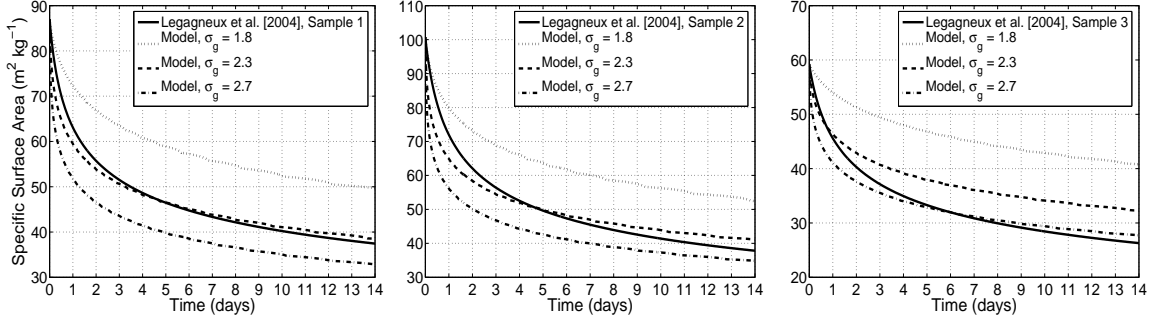


FIGURE 3.1. Comparison of model predictions of isothermal specific surface area evolution with measurements from *Legagneux et al.* (2004). The three panels each show one observed timeseries and three modeled timeseries, assuming different initial size distribution widths. Model initial effective radius is chosen to match initial observed SSA.

weak. *Fukuzawa and Akitaya* (1993), however, show that depth hoar can form very rapidly in surface snow.

We compare model predictions with *Fukuzawa and Akitaya* (1993). In laboratory studies, they induced temperature gradients from 150 to 300 K m<sup>-1</sup> in low density snow (80–100 kg m<sup>-3</sup>) made with an ice-slicer. They maintained a mean temperature of -16 °C at the sampling depth (1 cm). They report mean diameter,  $\bar{d}$ , as that of spheres with equal cross-sectional area as the photographed crystals, and note that this method can lead to high estimation biases. Experiments were conducted for up to 50 hours. We replicated these experimental conditions for all temperature gradients with SNICAR, using different values of  $\phi$ , and present a scatter-plot of modeled *vs.* observed mean radius in Figure 3.2.

*Fukuzawa and Akitaya* (1993) observe highly linear growth rates, whereas SNICAR predicts more rapid initial growth that tapers off. Based on our isothermal snow analysis, we used  $\sigma_g = 2.3$ , while snow produced by an ice-slicer may be more homogeneously-sized. However, we do not attribute the non-linear growth evolution to curvature effects, as a sensitivity study with monodisperse grain size showed only slightly more linear growth. The large TG of these studies overshadows any curvature effects, except in the first couple of hours. Interestingly, similar non-linear growth functions have been observed in long-term, high TG studies (*Sturm and Benson*, 1997; *Baunach et al.*, 2001), as mentioned above. Nonetheless, model-measurement agreement is quite good when we assume  $\phi = 5$ . Also, while we must use mean radius,

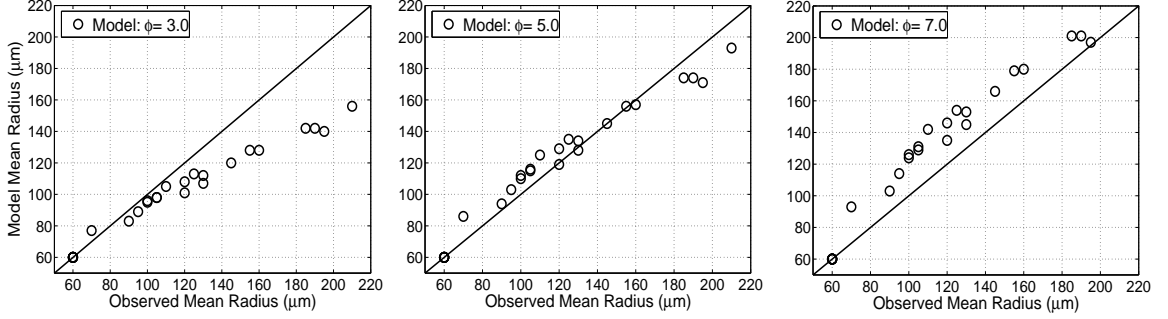


FIGURE 3.2. Comparison of model-predicted mean radius with observations from *Fukuzawa and Akitaya* (1993) under temperature gradients of 150, 200, 250, and 300 K m<sup>-1</sup>. The three panels show the same observations, but illustrate the effect of increasing model standard deviation of inter-particle spacing (left to right), defined by model parameter  $\phi$ .

$\bar{r}$  for comparison with *Fukuzawa and Akitaya* (1993), we emphasize that it is not the parameter of interest, having little bearing on snow radiative properties. In fact, the time-progression of  $\bar{r}$  and  $r_e$  can be *inversely* related if mass transfer is skewed towards one end of a broad size distribution. Hence, model-measurement agreement of  $\bar{r}$  is no guarantee that SNICAR predicts realistic albedo evolution. *Fukuzawa and Akitaya* (1993) is, however, the most relevant and comprehensive observational study on TG growth that we are aware of.

We also compare model predictions with two long-term laboratory observations, presented in Table 3.2. These studies examine growth in denser, larger-grained snow. They have less relevance to surface snow, but nonetheless offer some insight into SNICAR’s performance. *Baunach et al.* (2001) use the same equal-area method for determining grain size as *Fukuzawa and Akitaya* (1993) and *Lehning et al.* (2002) publish grain size referring to the greatest extension of the grain. In the long-term,  $\phi = 7$  provides better agreement with these data, but the measurement technique of *Lehning et al.* (2002) gives greater radius than the mean radius that we model.

Finally, we compared SNICAR predictions with recent observations of SSA evolution under TG conditions (*Schneebeil and Sokratov*, 2004). They use X-ray computed microtomography (XMT) to observe 3-D snow microstructure undergoing TG metamorphism. While this technique holds excellent promise for understanding the physics of crystal metamorphism, as sublimation and deposition on individual crystals are observed real-time, SSA evolution was not the focus of this study. Unfortunately, SSA

TABLE 3.2. Long-term temperature gradient growth

Time	Mean Radius ( $\mu\text{m}$ )			
	Observation	Mdl( $\phi = 3$ )	Mdl( $\phi = 5$ )	Mdl( $\phi = 7$ )
<i>(Baunach et al., 2001)</i> , $dT/dz = 30$ , $\rho_s = 200$ , $T = 269$				
0 days	135	135	135	135
23 days	415	318	387	444
30 days	455	355	435	501
<i>(Lehning et al., 2002)</i> , $dT/dz = 240$ , $\rho_s = 120$ , $T = 263$				
0 days	261	261	261	261
12.7 days	1345	895	1135	1338
<i>(Lehning et al., 2002)</i> , $dT/dz = 160$ , $\rho_s = 140$ , $T = 263$				
0 days	256	256	256	256
12.9 days	1174	702	877	1024
<i>(Lehning et al., 2002)</i> , $dT/dz = 35$ , $\rho_s = 210$ , $T = 263$				
0 days	256	256	256	256
30 days	713	457	548	625

deduced from XMT depends on scan resolution, so results from this method are inconsistent with the gas adsorption technique (*Legagneux et al., 2004*). We found best agreement with their results using  $3 < \phi < 5$ , but hesitate to place much emphasis on XMT observations until they can be corroborated with gas adsorption results.

More controlled experiments of fresh snow SSA evolution are needed to realistically assess SNICAR’s predictions of TG growth in the context of albedo evolution. Placing the heaviest emphasis on *Fukuzawa and Akitaya (1993)*, and considering a mean value of the other studies,  $\phi = 5$  is a reasonable assumption. We assume this value for the rest of the study, but should re-assess it as future observations becomes available.

### 3.4.3 Snow Albedo Evolution: Model Sensitivity to Physical Parameters

In this section we use SNICAR to examine the influence of  $\sigma_g$ , temperature, TG, and snow density on snow albedo evolution. Isolating these parameters also helps us assess if SNICAR captures the basic observations of TG growth listed in methods. Although  $r_e$  is most influential on near-IR albedo ( $0.7\text{--}5.0\mu\text{m}$ ), we only examine broadband albedo ( $0.3\text{--}5.0\mu\text{m}$ ). Grain size varies with snow depth, influencing bulk snow

albedo (e.g., *Grenfell et al.*, 1994), but here we assume an optically-thick snowpack of uniform time-evolving effective grain size. SNICAR predicts broadband albedo variation of only 0.0075 when  $r_e$  varies from 50–500  $\mu\text{m}$  beneath a 5 mm LWE layer with  $r_e = 50 \mu\text{m}$ . Thus, assuming a homogeneous, optically-thick snowpack is reasonable for fresh snowfall on top of existing snow. However, we expect  $r_e$  time-evolution to vary within a fresh snow layer in a strong surface TG. We assume direct incident flux with a zenith angle of  $60^\circ$ . Model snowpack configurations for our four experiments are summarized in Table 3.3. Also listed are the initial snow albedos, corresponding to initial effective radii,  $r_{e0}$ . Equation 3.10 relates  $\hat{S}$  to  $r_e$ , but we use  $r_e$  in these discussions because of its common use by the radiative transfer community.

Figure 3.3 shows the temporal evolution of  $r_e$  and albedo (plotted on different axes) for these configurations. Model Experiment A depicts isothermal snow evolution with four different initial size distributions. We see that large  $\sigma_g$  drives rapid initial albedo decay. But comparison of the two  $\sigma_g = 2.3$  simulations shows that larger initial effective radii mitigate the effect that large  $\sigma_g$  can have by reducing the Kelvin Effect. Only the combination of small  $r_{e0}$  and large  $\sigma_g$  drives rapid initial albedo decay. After 14 days, however, the albedo range is only 0.04 for the given range of initial conditions.

Model Experiment B demonstrates the effect of temperature on albedo evolution while holding  $\sigma_g$  and  $r_{e0}$  fixed with a modest (also fixed) TG. In contrast to the effects of  $\sigma_g$  and  $r_{e0}$ , temperature differences produce widespread albedo differences with time. For this configuration and these three temperatures, the albedos after 14 days are 0.79, 0.81, and 0.85.

Model Experiment C isolates the influence of TG with all other initial parameters

TABLE 3.3. Experimental configurations for Figure 3.3

	Exp. A	Exp. B	Exp. C	Exp. D
$\sigma_g$	1.25 – 3.5	2.3	2.3	2.3
$r_{e0}$ [ $\mu\text{m}$ ]	50, 100	50	50	50
Initial Alb.	0.854, 0.825	0.854	0.854	0.854
$T$ [ $^\circ\text{C}$ ]	–5	–50 – 0	–5	–5
$dT/dz$ [ $\text{K m}^{-1}$ ]	0	20	0 – 250	100
$\rho_s$ [ $\text{kg m}^{-3}$ ]	N/A	100	100	50 – 480

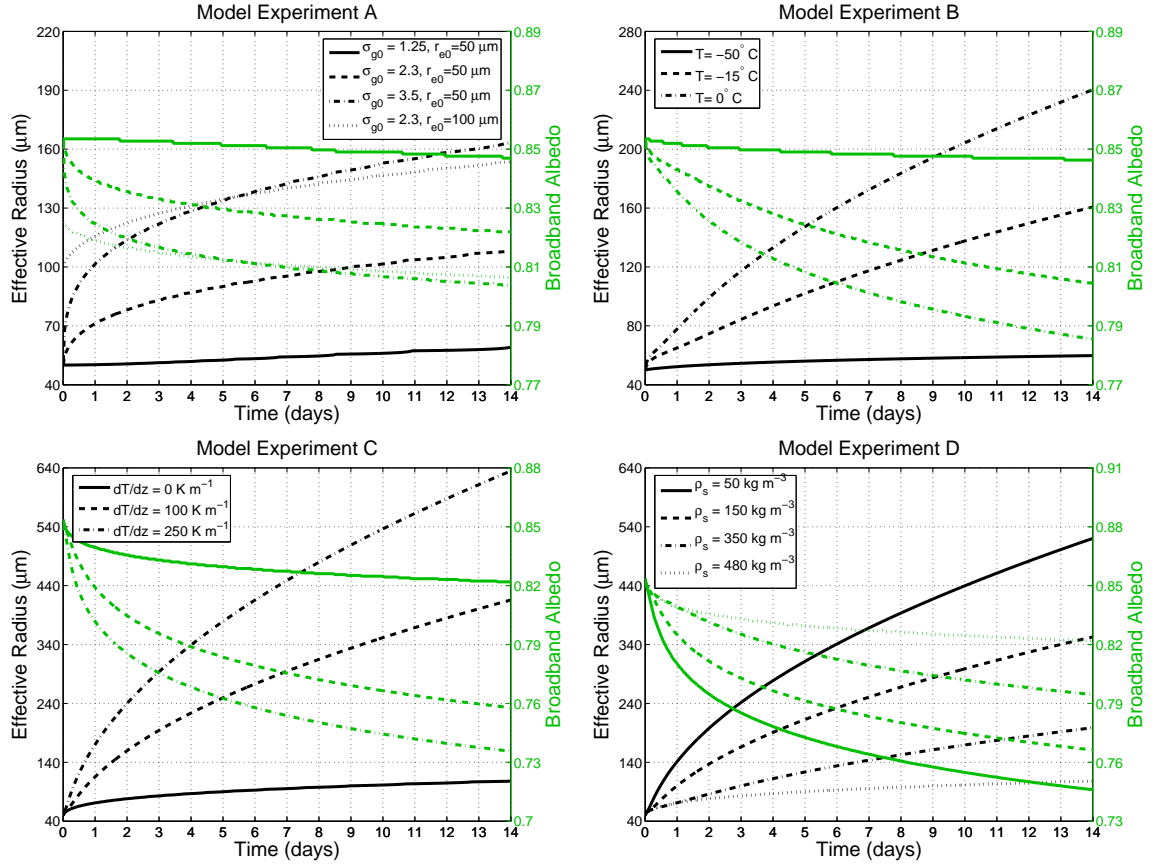


FIGURE 3.3. Model parameter study illustrating the evolution of snow effective radius ( $r_e$ ) and albedo evolution, isolating dependence of (a) initial size distribution, (b) temperature, (c) temperature gradient, and (d) snow density. Time evolution of effective radius is plotted in black against the left axis and broadband albedo in green against the right axis.

fixed. We see that, given realistic ranges of the physical parameters, TG can be the most influential on albedo. For this range of TG, albedo and  $r_e$  range by 0.09 and 530  $\mu\text{m}$ , respectively, after 14 days. In a sensitivity test with  $T = -50^\circ\text{C}$ , albedo varied by only 0.017 after 14 days under the same range of TG. Thus, our model conforms with observation that TG becomes unimportant in colder snow (*Kamata et al.*, 1999). We attribute this behavior to the non-linear dependence of saturation vapor pressure on temperature. Vertical vapor density gradients drive TG growth, and  $d\rho_v/dz$  decreases with decreasing temperature in near-saturation conditions because of the Clausius-Clapeyron relationship.

Finally, model Experiment D shows that snow density also modulates the importance of TG. All albedo change with  $\rho_s = 480 \text{ kg m}^{-3}$  is from curvature growth, since  $\bar{a} = 0$  (Equation 3.14). The range of albedo after 14 days for  $50 < \rho_s < 350 \text{ kg m}^{-3}$  is about 0.05. While *Marbouty* (1980) suggests that variable snow densities less than  $150 \text{ kg m}^{-3}$  do not affect TG growth, SNICAR predicts continual increasing influence as  $\rho_s \rightarrow 0$ . It may be reasonable to cap the effect of  $\rho_s$  at some low value, but given observational uncertainties and realistic snow densities, we refrain from doing so here.

### 3.4.4 Observed Albedo Evolution

At this time we cannot conduct a meaningful comparison of model and observed albedo evolution because:

1. We know of no observational studies simultaneously measuring albedo, temperature gradient, and size distribution.
2. Magnitudes of the competing wind effects (ventilation and fine crystal deposition) are unknown and not included in SNICAR.
3. We do not know the importance of, or consider, nighttime frost formation of fine, 'bright' crystals (e.g., *Pirazzini*, 2004).
4. Concurrent observations of albedo and accumulation of absorbing impurities, such as soot, are rare.

The paucity of data stresses the need for controlled studies which simultaneously measure albedo, vertically-resolved temperature, SSA,  $\rho_s$ , and accumulation of impurities at high temporal resolution, so the methods we discuss here can be better applied. In spite of these uncertainties, we include one timeseries of observed dry snow albedo evolution. Comparison of model predictions with these data demonstrates that SNICAR is capable of reproducing reality, whether for right or wrong reasons. More definitive conclusions about model performance can only be drawn when more comprehensive observational data becomes available.

We examined six years of data from the Subnivean site of the Niwot Ridge Long Term Ecological Research (LTER) site in Colorado (*Williams*, 2005), and five years of data from the Atmospheric Radiation Measurement (ARM) site at Barrow, Alaska. We isolated only one timeseries longer than five days, following a fresh snowfall event, in which there were consistent clear-sky or cloudy conditions, daily maximum temperature didn't exceed  $0.5^\circ\text{C}$ , and there was no, or little, fresh snowfall.

The Jan. 2, 2001 Niwot Ridge snowfall event (81 mm LWE) was followed by 10 clear-sky days. Unfortunately, the temperature exceeded  $0^\circ\text{C}$  (by only  $0.5^\circ\text{C}$ ) for three hours on the third day following snowfall, and a light snowfall of 2 mm LWE was also reported on this day. There is a very slight albedo increase this day, which likely tracks the snowfall, but could also be other variability. It is possible that the two effects partially canceled each other, or that they were both insignificant.

Figure 3.4 depicts the albedo evolution following this event, as measured at different times of the day, and also as predicted by SNICAR with different configurations. The data are hourly averages from 10-minute observations, and timeseries measured at the same time-of-day ensure nearly consistent zenith-angle. We also include snow aging parameterization from the NCAR Community Land Model 3 (CLM) (*Oleson et al.*, 2004), and NASA GISS GCM ModelE (*Schmidt et al.*, 2006), which is based on *Loth and Graf* (1998), who, in turn, uses albedo decay from *Verseghy* (1991) for dry, deep snow. CLM dry snow aging depends on snow temperature, while the non-melting relationships described by *Verseghy* (1991) and *Loth and Graf* (1998) do not. We have included the albedo increase that CLM would prescribe for the 2 mm LWE snowfall on day 3. To reduce zenith-angle dependence, all curves depict albedo change, rather than absolute albedo. The error bars represent one standard deviation of measured

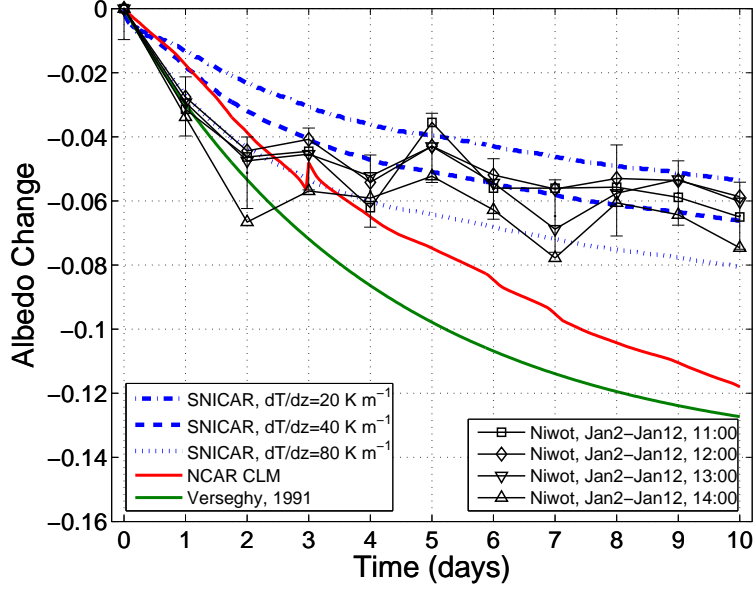


FIGURE 3.4. Observed and modeled albedo decay at Niwot Ridge following the January 2, 2001 snowfall event. Error bars represent one standard deviation of all measurements composing each day’s albedo change.

albedo reduction, centered about each day’s mean albedo change. The 10-minute measurements are normalized to their base albedo at time zero, and the standard deviation is derived from all 24 daily measurements. The three SNICAR predictions are of direct-radiation albedo evolution with  $dT/dz = 20, 40, \text{ and } 80 \text{ K m}^{-1}$ , assuming  $\sigma_g = 2.3$ ,  $\rho_s = 100 \text{ kg m}^{-3}$ , and vertically-homogeneous grain size ( $r_{e0} = 50 \mu\text{m}$ ), which is justified in this case because the snowfall event was large and rapid. SNICAR and CLM models are both driven with hourly mean air temperature, which we use as a rough surrogate for snow temperature. This assumption should cause little error for these conditions, as driving SNICAR with the mean (constant) temperature alters 10-day albedo change by  $\sim 1\%$ .

We make several observations here. First, the large 1-day albedo change ( $-0.03$ ) is characteristic of rapid curvature growth. We can replicate this with small TG and  $\sigma_g > 2.3$ , or with large TG. Second,  $dT/dz = 80 \text{ K m}^{-1}$  reproduces observed albedo decay during the first 4 days very well. Third, there is an albedo rise on Day 5 that could be explained by atmospheric- or frost- deposition of fine crystals, or noise. If deposition is the cause, grain growth of the underlying snow may proceed at a similar rate as predicted with  $dT/dz = 80 \text{ K m}^{-1}$ . Fourth, SNICAR captures this



observational trend better than the GCM parameterizations, which predict excessive albedo decay after day 3. CLM implicitly accounts for globally uniform accumulation of impurities, which is one reason for its greater predicted albedo reduction. In future GCM studies, we will account for time-dependent accumulation of impurities with on-line atmospheric transport and deposition.

### 3.4.5 Empirical Parameterization

*Legagneux et al.* (2004) propose Equation 3.16 as an empirical representation for observed isothermal SSA evolution. We show that Equation 3.16 robustly fits predictions of SSA evolution over a wide range of temperature, TG, and snow density. The simplicity of this equation is attractive because of the numerous size bins that SNICAR requires to capture curvature growth. Resulting computational savings open the door for its use in climate models and snow chemistry studies which utilize SSA.

We compute best-fit parameters  $\tau$  and  $\kappa$  for Equation 3.16 to match 14-day simulated SSA over the domain  $210 \leq T \leq 273 \text{ K}$ ,  $0 \leq \frac{dT}{dz} \leq 300 \text{ K m}^{-1}$ , and  $50 \leq \rho_s \leq 400 \text{ kg m}^{-3}$ . Figure 3.5 depicts time evolution of SSA predicted by SNICAR and Equation 3.16 with best-fit parameters over some of this domain. Agreement is exceptionally good, even with large TG and range of  $\rho_s$ . Best-fit parameters for the curves shown in this figure are listed in Table 3.4. Implementation of this method simply requires the time-derivative of Equation 3.16 and an online lookup table retrieving best-fit parameters as a function of  $T$ ,  $dT/dz$ , and  $\rho_s$ . The authors can be contacted for a comprehensive table.

## 3.5 Conclusions

We have developed a new, physically-based model which predicts the evolution of dry snow specific surface area (SSA), and is suitable for coupling to full snow thermodynamic and air-snow chemistry models. Recent studies (*Grenfell and Warren, 1999; Neshyba et al., 2003; Grenfell et al., 2005*) justify use of snow SSA to obtain accurate hemispheric radiative fluxes, even for aspherical particles, thus linking our results to albedo evolution. Our model suggests that curvature-driven vapor diffu-

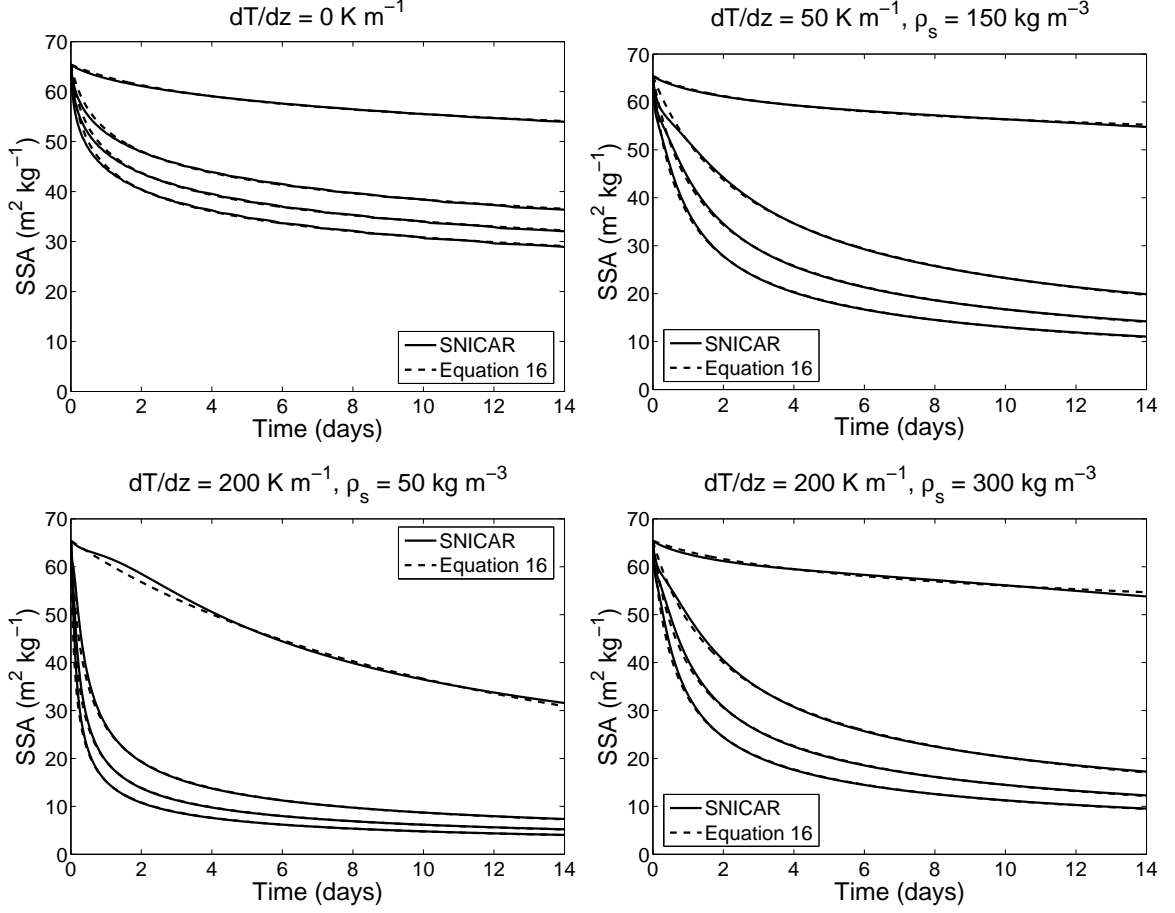


FIGURE 3.5. Comparison of modeled specific surface area (SSA) evolution with parameterization from Equation 3.16, using best-fit parameters for  $\tau$  and  $\kappa$ . Each plot depicts SSA evolution for a given temperature gradient and snow density with snow temperatures of (curves from top to bottom)  $-50$ ,  $-20$ ,  $-10$ , and  $0$  °C.

TABLE 3.4. Best-fit parameters of Equation 3.16 for the range of temperatures, temperature gradient, and snow density shown in Figure 3.5

		Snow Temperature (°C)				
$dT/dz$ (K m <sup>-1</sup> )	$\rho_s$ (kg m <sup>-3</sup> )		-50	-20	-10	0
0	150	$\tau$	43.6	7.1	4.5	3.2
		$\kappa$	11.4	6.7	6.1	5.8
50	150	$\tau$	27.5	47.1	21.0	11.9
		$\kappa$	15.3	1.7	1.8	1.9
200	50	$\tau$	370.6	5.2	2.5	1.5
		$\kappa$	0.9	1.9	1.9	1.9
200	300	$\tau$	47.2	35.0	15.5	8.8
		$\kappa$	11.7	1.8	1.9	1.9

sion dominates mass transfer of fresh snow under low temperature gradient. Vertical temperature gradients exceeding  $20 \text{ K m}^{-1}$ , however, induce vapor density gradients which otherwise dominate grain growth and albedo decay. The influence of temperature gradient is controlled by temperature, snow density, and variance of interparticle spacing.

Model results track laboratory observations of isothermal SSA evolution very well. Predictions of temperature gradient growth compare favorably with observed mean radius evolution, but simultaneous measurements of SSA and temperature gradient are needed for thorough model evaluation. 14-day albedo change of dry snow with identical initial effective radii varies from -0.01 to -0.13, depending on snow conditions. Model predictions track one 10-day timeseries of clear-sky albedo measurements from Niwot Ridge better than two GCM parameterizations, but too little is known about the snowpack conditions to draw any definitive conclusions. Lastly, we show that a simple representation of SSA evolution robustly describes our model over a wide range of parameters. Its simplicity and effectiveness suggest that it could be a valuable addition to climate and snow chemistry models.

Existing GCM representations of snow aging do not consider temperature gradient in albedo evolution, although this and several other studies (*Marbouty*, 1980; *Fukuzawa and Akitaya*, 1993; *Sturm and Benson*, 1997) show it to be very important. Investigations into the effects of blowing snow, wind ventilation, and frost formation are also needed for a thorough understanding of snow albedo evolution. This study also highlights the need for high-resolution experimental studies that simultaneously observe snow temperature gradient, SSA, accumulation of soot and dust, and albedo. Such data would provide stronger basis for defining model parameters describing snow SSA and albedo evolution. If models are to accurately predict climate changes due to greenhouse and other forcings, they must capture influences of all important processes involved in snowpack evolution.

## 3.6 Acknowledements

We dedicate this paper to the fond memory of Walter Rosenthal, whose enthusiastic conversations on sintering will be missed. We thank three anonymous reviewers for critical analysis and helpful comments about our methods. We also thank Jeff Dozier for his support, Teruo Aoki, Michael Lehning and Charles Fierz for providing snow grain size observations, Anne-Sophie Taillandier and Florent Domine for providing advice and references about SSA evolution, and Steve Warren for advice on relationships between size distributions and albedo. Data were obtained from the NSF supported Niwot Ridge Long-Term Ecological Research project and the University of Colorado Mountain Research Station. Funding for this work was provided by NSF/NCAR SGER ATM-0503148 and NASA Earth System Science Fellowship NNG05GP30H. Computations supported by Earth System Modeling Facility NSF ATM-0321380.

# CHAPTER 4

## Present Day Climate Forcing and Response from Black Carbon in Snow

As appears in:

Flanner, M. G., C. S. Zender, J. T. Randerson, and P. J. Rasch (2007), Present day climate forcing and response from black carbon in snow, *J. Geophys. Res.*, *in press*.

### 4.1 Abstract

We apply our SNow, ICe, and Aerosol Radiative (SNICAR) model, coupled to a GCM with prognostic carbon aerosol transport to improve understanding of climate forcing and response from black carbon (BC) in snow. Building on two previous studies, we account for interannually-varying biomass burning BC emissions, snow aging, and aerosol scavenging by snow meltwater. We assess uncertainty in forcing estimates from these factors, as well as BC optical properties and snow cover fraction. BC emissions are the largest source of uncertainty, followed by snow aging. The rate of snow aging determines snowpack effective radius ( $r_e$ ), which directly controls snow reflectance and the magnitude of albedo change caused by BC. For a reasonable  $r_e$  range, reflectance reduction from BC varies three-fold. Inefficient meltwater scavenging keeps hydrophobic impurities near the surface during melt and enhances forcing. Applying biomass burning BC emission inventories for a strong

(1998) and weak (2001) boreal fire year, we estimate global annual mean BC/snow surface radiative forcing from all sources (fossil fuel, biofuel, and biomass burning) of  $+0.054$  ( $0.007 - 0.13$ ) and  $+0.049$  ( $0.007 - 0.12$ )  $\text{W m}^{-2}$ , respectively. Snow forcing from only fossil fuel+biofuel sources is  $+0.043$   $\text{W m}^{-2}$  (forcing from only fossil fuels is  $+0.033$   $\text{W m}^{-2}$ ), suggesting the anthropogenic contribution to total forcing is at least 80%. 1998 global land and sea-ice snowpack absorbed 0.60 and 0.23  $\text{W m}^{-2}$ , respectively, because of direct BC/snow forcing. The forcing is maximum coincidentally with snowmelt onset, triggering strong snow-albedo feedback in local springtime. Consequently, the “efficacy” of BC/snow forcing is more than 3 times greater than forcing by  $\text{CO}_2$ . 1998 and 2001 land snowmelt rates north of  $50^\circ\text{N}$  are 28% and 19% greater in the month preceding maximum melt of control simulations without BC in snow. With climate feedbacks, global annual mean 2-meter air temperature warms 0.15 and 0.10°C, when BC is included in snow, whereas annual arctic warming is 1.61 and 0.50°C. Stronger high-latitude climate response in 1998 than 2001 is at least partially caused by boreal fires, which account for nearly all of the 35% biomass burning contribution to 1998 arctic forcing. Efficacy was anomalously large in this experiment, however, and more research is required to elucidate the role of boreal fires, which we suggest have maximum arctic BC/snow forcing potential during April–June. Model BC concentrations in snow agree reasonably well ( $r = 0.78$ ) with a set of 23 observations from various locations, spanning nearly 4 orders of magnitude. We predict concentrations in excess of 1000  $\text{ng g}^{-1}$  for snow in northeast China, enough to lower snow albedo by more than 0.13. The greatest instantaneous forcing is over the Tibetan Plateau, exceeding 20  $\text{W m}^{-2}$  in some places during spring. These results indicate that snow darkening is an important component of carbon aerosol climate forcing.

## 4.2 Introduction

Very small quantities of black carbon (BC, the strongly absorbing component of carbonaceous aerosols) reduce snow reflectance because of multiple scattering in the snowpack and huge disparity between mass absorption coefficients of BC and ice (e.g., *Warren and Wiscombe*, 1980). Reflectance reduction caused by BC and other

absorbing impurities is of concern because slight changes in solar absorption can alter snowmelt timing, and snow spatial coverage is tightly coupled to climate through snow-albedo feedback (e.g., *Budyko*, 1969).

Several other positive feedbacks amplify the first-order warming effect of BC in snow. Warmer snow temperatures can accelerate snow effective radius ( $r_e$ ) growth (e.g., *Flanner and Zender*, 2006), which darkens the snow itself. Second, the radiative perturbation of a given BC mass mixing ratio is greater in snow with larger  $r_e$  (*Warren and Wiscombe*, 1980). Third, spring and summer melting can concentrate hydrophobic and large impurities near the snow surface (*Clarke and Noone*, 1985). Fourth, the stable atmosphere of high latitudes prevents rapid heat exchange with the upper troposphere, resulting in strong surface temperature response to surface radiative forcings (*Hansen and Nazarenko*, 2004). We represent all of these feedbacks with a coupled snow-aerosol-climate model.

*Hansen and Nazarenko* (2004) raised awareness of BC/snow forcing by assuming spatially-uniform snow albedo reductions over arctic sea-ice and northern hemisphere land. They estimate global adjusted BC/snow radiative forcing of  $+0.15 \text{ W m}^{-2}$ , and global warming of  $0.24^\circ\text{C}$ , yielding a forcing “efficacy” (*Hansen et al.*, 2005), or change in equilibrium global mean temperature per unit power of radiative forcing, double that of  $\text{CO}_2$ . *Hansen et al.* (2005) scaled the BC/snow forcing based on deposition fields and revised their original estimate to  $+0.05 \text{ W m}^{-2}$  (corrected value published in Appendix A.5 of *Hansen et al.* (2006)), with a warming of  $0.065^\circ\text{C}$ . *Jacobson* (2004b) predicts snow and ice reflectance with a radiative transfer solution that interactively depends on BC deposition in an aerosol/chemical transport GCM. He predicts warming of  $0.06^\circ\text{C}$  from snow darkening by fossil fuel and biofuel BC.

We attempt to build upon these studies by accounting for, and assessing uncertainty from interannually-varying biomass burning BC emissions, snow aging and spatially-varying grain size, meltwater scavenging of BC in the snowpack, BC optical properties, and snow cover fraction. We discuss some features of our SNow, ICe, and Aerosol Radiative (SNICAR) model, including the influence of snow  $r_e$  on reflectance and vertical heating perturbation from BC. Next we compare global predictions of BC in snow with observations. Then we estimate the global climate response and efficacy of BC/snow forcing, finding three-fold greater global temperature response

than expected from equal forcing by CO<sub>2</sub>. Finally, we look at spatial and temporal patterns of the forcing and climate response with the goal of understanding this large efficacy in the context of snowmelt timing and snow-albedo feedback.

### 4.3 Methods

We simulate radiative transfer in the snowpack with SNICAR (*Flanner and Zender, 2005*), which utilizes theory from *Wiscombe and Warren (1980)* and the two-stream, multi-layer radiative approximation of *Toon et al. (1989)*. The multi-layer model allows for vertically-heterogeneous snow properties and heating, and influence of surfaces underlying snowpack. We couple this snow radiative model to the National Center for Atmospheric Research (NCAR) Community Atmosphere Model, version 3 (CAM3) (e.g., *Collins et al., 2004*), with configuration described below.

Hemispheric radiative fluxes may be accurately estimated for media composed of aspherical ice particles by assuming collections of spheres that conserve the total surface area and volume of the real media (*Grenfell and Warren, 1999; Neshyba et al., 2003; Grenfell et al., 2005*). For this reason,  $r_e$ , or surface area-weighted mean radius, is the most appropriate snow grain metric for optical considerations. We compute Mie parameters offline at fine spectral resolution for lognormal distributions of absorbing aerosols and a wide range of ice  $r_e$ . Coupled to a GCM, SNICAR uses only 5 spectral bands (0.3 – 0.7, 0.7 – 1.0, 1.0 – 1.2, 1.2 – 1.5, and 1.5 – 5.0  $\mu\text{m}$ ) for computational efficiency. Following the Chandrasekhar Mean approach, optical properties are weighted into broad bands according to incident solar flux (*Thomas and Stamnes, 1999*). We use surface incident flux typical of mid-latitude winter for clear- and cloudy-sky conditions, generated with the atmospheric ShortWave NarrowBand Model (SWNB) (*Stamnes et al., 1988; Zender et al., 1997*). In addition to weighting by solar flux, we also weight single-scatter albedo ( $\omega$ ) for ice grains by hemispheric albedo of an optically-thick snowpack:

$$\omega(\bar{\lambda}) = \frac{\int_{\lambda_1}^{\lambda_2} \omega(\lambda) S_s^\downarrow(\lambda) \alpha(\lambda) d\lambda}{\int_{\lambda_1}^{\lambda_2} S_s^\downarrow(\lambda) \alpha(\lambda) d\lambda} \quad (4.1)$$



where  $S_s^\downarrow$  is the downwelling surface incident flux (unique for diffuse and direct cases), and  $\alpha$  is the hemispheric albedo of an optically-thick snowpack of homogeneous  $r_e$ .

This weighting scheme produces relative error in albedo predicted using 5 bands of less than 0.5%, relative to 470-band solutions. Over a wide range of zenith angles, effective radii, and impurity concentrations, we found this technique to be significantly more accurate (factor of five difference in mean relative error) in predicting spectrally-averaged albedo than when  $\omega$  is weighted only by  $S_s^\downarrow$ . However, we stress that it is only an empirical approach and provides undesirable results in more general cases (such as the case of weighting the limits  $\omega = 0$  and  $\omega = 1$ ). It also requires *a priori* narrowband albedo values of the bulk medium. Errors in sub-2 cm absorption with this approach are  $\sim 4\%$ , slightly greater than errors without the albedo weighting of  $\omega$ . Broadband Mie parameters for  $50 \leq r_e \leq 1000 \mu\text{m}$  are compiled into a lookup table for online retrieval in the host GCM.

We partition online surface-incident visible and near-infrared (NIR), diffuse and direct flux into the 5 bands used by SNICAR using the same offline estimates of narrowband mid-latitude winter fluxes. We apply the delta-Eddington (*Joseph et al.*, 1976) and delta-Hemispheric Mean (*Toon et al.*, 1989) approximations in the visible and NIR spectra, respectively. In very rare situations (about 1 in  $10^6$  cases), the multi-layer solution approaches an indeterminate case with direct-beam incident flux (*Toon et al.*, 1989) so we adjust the sun angle by a few degrees to achieve reasonable predictions.

Multiple aerosol species are accounted for by summing extinction optical depths of each component, weighting individual single-scatter albedos by optical depths, and weighting asymmetry parameters by the product of optical depths and single-scatter albedos. Hydrophilic and hydrophobic BC species are treated separately. Absolute error in albedo predicted with 5 bands for snow with BC is also  $< 0.5\%$ , although albedo reduction from typical BC concentrations is consistently 4–6% (relative) less with 5 bands than with 470. As we will show, this bias is much smaller than other uncertainties.

We couple SNICAR to the CAM3 GCM with a slab ocean model that has spatially-varying mixed layer depth with fixed monthly-mean ocean heat transport. We include

prognostic transport and wet and dry deposition of hydrophobic and hydrophilic BC and organic carbon (OC) (*Rasch et al.*, 2001), using a single size bin for each of these four components. Wet deposition tendencies consist of both first-order loss from below-cloud scavenging by precipitation and in-cloud scavenging that assumes a fixed fraction of aerosol resides within the cloud water. BC and OC dry deposition velocities are fixed at  $1 \text{ mm s}^{-1}$  (e.g., *Collins et al.*, 2004). Carbon aerosols are emitted into the atmosphere as hydrophobic and then transform to hydrophilic components with an e-folding time of 1.2 days. Transformation ceases upon deposition to the snowpack.

Snow on land is represented in the Community Land Model (CLM3) (e.g., *Oleson et al.*, 2004) with a 5-layer model based on *Jordan* (1991) that accounts for vertically-resolved snow thermal processes, densification, and meltwater transport. Snow on sea-ice is represented with a single layer in the Community Sea Ice Model (CSIM) component of CAM3. Radiative layers in SNICAR match thermal layers in these models. GCM gridcell area is approximately  $97000 \text{ km}^2$  near the equator and  $17600 \text{ km}^2$  at  $80^\circ\text{N}$ .

We calculate instantaneous radiative forcing of carbon aerosols in both snow and the atmosphere at each radiative transfer timestep as the difference in absorbed radiation with all aerosols and all aerosols except carbon aerosols. Radiative transfer estimates with carbon aerosols feed back into the model climate. Reported atmospheric forcings are from BC+OC, whereas snow forcings are from only BC (discussed below).

Forcing is sensitive to cloud treatment, which strongly affects both surface-incident and outgoing top-of-atmosphere radiative fluxes. Cloud fraction is diagnosed based on relative humidity, atmospheric stability, and convective mass fluxes (*Collins et al.*, 2004). The cloud vertical overlap parameterization is described in *Collins* (2001). Liquid and ice cloud optical properties are parameterized according to *Slingo* (1989) and *Ebert and Curry* (1992), respectively. Thus mixed-phase bulk cloud radiative properties depend on prognosed cloud water path (e.g., *Rasch and Kristjánsson*, 1998), temperature-dependent drop effective radius, and ice fraction. Liquid and ice hydrometeors are each represented with a single size category. Finally, the atmospheric multi-layer radiative transfer approximation (*Briegleb*, 1992) utilizes the

delta-Eddington approximation and 19 spectral bands in the solar spectrum. Atmospheric and snow radiative transfer are solved separately for practical reasons, as the atmospheric radiation model is engineered to utilize pre-determined surface albedo.

To estimate present-day global forcing of BC in snow, we consider combinations of low, central, and high estimates of the following factors:

### 4.3.1 BC and OC Emissions

We use low, central, and high fossil fuel (FF) and biofuel (BF), BC and OC emission estimates at  $1^\circ \times 1^\circ$  resolution from *Bond et al.* (2004). These annual mean estimates are derived from 1996 fuel-use data and assumptions about local combustion technology and practice. We use monthly biomass burning (BB) estimates of BC and OC from the Global Fire Emissions Database, version 2 (GFEDv2) (*Van der Werf et al.*, 2006), which are derived from satellite-monitored burned area, modeled fuel load and combustion completeness, and aerosol emission factors from *Andreae and Merlet* (2001, personal communication). We also apply regional satellite-derived carbon monoxide inversion factors (*Prasad Kasibhatla, unpublished data, 2006*), which constrain the forward emission estimates. Boreal forest fires exhibit strong interannual variability and are likely the dominant source of arctic BC during moderate fire seasons (*Stohl*, 2006). In this 1997-2004 BB emissions timeseries, 1998 was the strongest boreal fire year, and we select 2001 as representative of a weak year. Boreal emissions were weaker in 1997, but global emissions were greatest this year. We estimate high and low emissions at each gridcell and month for these two years by combining standard error, in quadrature, of regional CO inversion factors, and CO and BC emission factors (*Andreae and Merlet*, 2001, personal communication). Assuming a broad range of emissions may compensate for some variability in atmospheric transport mechanisms, which we do not address here. Zonal-mean, annual FF+BF and BB emissions are shown in Figure 4.1, where a large difference in high-latitude BB emissions between 1998 and 2001 can be seen. Table 4.1 lists global and boreal annual FF+BF and BB emission estimates, and all other experimental configurations.

All emissions enter the lowest model atmosphere layer. Particulate matter from strong fires can be injected above the boundary layer however, and assumptions about

TABLE 4.1. Configurations for 1998 and 2001 low, central, and high experiments

	Low Estimate	Central Estimate	High Estimate
FF+BF BC Emissions [ $\text{Tg yr}^{-1}$ ] (Global/N of $30^\circ\text{N}$ )	1.6/1.0	4.7/2.7	16.2/9.3
1998 BB BC Emissions [ $\text{Tg yr}^{-1}$ ] (Global/N of $30^\circ\text{N}$ )	2.1/0.4	4.1/0.8	6.5/1.6
2001 BB BC Emissions [ $\text{Tg yr}^{-1}$ ] (Global/N of $30^\circ\text{N}$ )	1.1/0.1	2.0/0.2	3.0/0.4
BC MAC (fresh, hydrophobic) [ $\text{m}^2 \text{g}^{-1}$ at 550 nm]	6.3	7.5	8.7
BC MAC (aged, hydrophilic) [ $\text{m}^2 \text{g}^{-1}$ at 550 nm]	9.5	11.3	13.1
Snow Aging Scaling Factor	0.5	1.0	2.0
Snow Cover Fraction	<i>Oleson et al. (2004)</i>	<i>Romanov and Tarpley (2004)</i>	<i>Yang et al. (1997)</i>
Hydrophilic Meltwater Scavenging Ratio ( $k_{\text{phi}}$ )	2.0	0.2	0.02
Hydrophobic Meltwater Scavenging Ratio ( $k_{\text{pho}}$ )	0.3	0.03	0.003

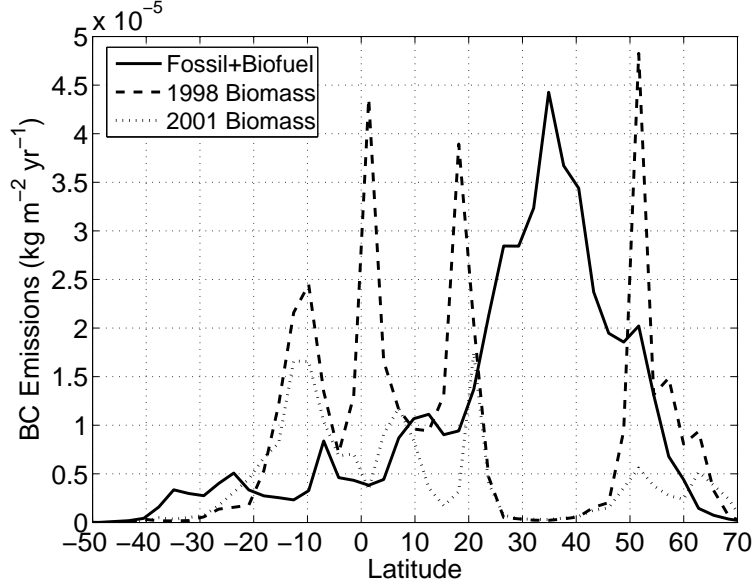


FIGURE 4.1. Zonal annual mean black carbon emissions from fossil fuel+biofuel combustion (*Bond et al.*, 2004) and biomass burning during 1998 and 2001 (*Van der Werf et al.*, 2006).

injection height may affect model high-latitude upper troposphere heating (*Rasch et al.*, 2005). Lacking associated injection height information for our emission inventories, we do not assess forcing sensitivity to this factor.

### 4.3.2 Optical Properties

*Bond and Bergstrom* (2006) comprehensively review current understanding of optical properties of freshly-combusted light absorbing aerosols. They suggest a mass absorption cross section (MAC) of  $7.5 \pm 1.2 \text{ m}^2 \text{ g}^{-1}$  at  $\lambda = 550 \text{ nm}$  for uncoated particles, based mostly on samples from diesel engines and traffic tunnels. Particle density, refractive index, size distribution, coatings, and morphology all affect the optical properties. But current understanding of these physical parameters, combined with Mie or Rayleigh-Debye-Gans theory, underpredict observed MAC by  $\sim 30\%$  (*Bond and Bergstrom*, 2006). Commonly used optical properties (*Hess et al.*, 1998) are in the correct observational range of BC MAC, but are derived by applying Mie theory to a highly unrealistic combination of physical properties. Scattering magnitude and direction by realistic BC concentrations have negligible effect on bulk snowpack radia-

tive transfer because scattering is dominated by the ice crystals. Therefore, realistic BC MAC, even if derived with assumptions that produce unrealistic  $\omega$  and scattering phase function, predicts realistic snowpack absorption enhancement. (This is not necessarily true for absorbing aerosols in the atmosphere, where scattering optical depth is much lower). For hydrophobic BC, we use indices of refraction from *Chang and Charalampopoulos* (1990), number-median radius of  $0.05\mu\text{m}$  (a central value among many studies published in *Bond et al.* (2006)), and lognormal size distribution with geometric standard deviation of 1.5. We use particle density as a tuning parameter to obtain  $\text{MAC} = 7.5\text{ m}^2\text{ g}^{-1}$  ( $\pm$  one standard deviation from *Bond et al.* (2004) for low and high estimates) at  $\lambda = 550\text{ nm}$ .

Coagulation between BC particles and collapse of the aggregate structure tend to occur as the particles age and obtain moisture (e.g., *Schnaiter et al.*, 2003), contributing to a reduction in MAC with atmospheric lifetime. But particle coating from condensation of weakly-absorbing material increases MAC (specific to the original BC mass) (e.g., *Jacobson*, 2001). *Bond et al.* (2006) suggest that the net effect of these competing processes increases MAC by a factor of  $\sim 1.5$  with aging. With this information, we treat aged, hydrophilic BC as sulfate-coated. We apply Mie theory, using the same core properties as hydrophobic BC and a sulfate coating with outer radius 1.67 times that of the uncoated BC, yielding an absorption enhancement of 1.5 at  $\lambda = 550\text{ nm}$ . Optical properties are applied consistently to these two aerosols in the atmosphere and snow. Uncertainty remains about BC/ice mixing states. We assume external mixtures of coated and uncoated BC, but BC coating by sulfate mimics that by ice, since both coatings are weakly absorbing. Furthermore, for small core diameters, increasing coating thickness only slightly increases the absorption amplification (*Bond et al.*, 2006).

We apply OPAC optical properties (*Hess et al.*, 1998) for water-soluble aerosol to atmospheric OC (*Collins et al.*, 2002; *Cooke et al.*, 1999), but do not treat OC in the snowpack. A short GCM sensitivity study with active OC in snowpack showed global forcing  $200\times$  smaller than BC/snow forcing using these optical properties. However, several recent studies (e.g., *Bond*, 2001; *Kirchstetter et al.*, 2004; *Hoffer et al.*, 2006; *Ganguly et al.*, 2005) showing carbon aerosol absorption features with Angstrom coefficients greater than 1, and other chemical analyses, lead *Andreae and*

*Gelencser* (2006) to state “there is clearly a substantial fraction of organic matter in fine atmospheric aerosol, which is light-absorbing, but has properties and origins very much different from soot and is definitely not black.” This “brown carbon” is characterized with Angstrom coefficients from 2–6, and is emitted in greater quantity from biomass burning and low-temperature combustion. Future research constraining OC emissions, atmospheric processes, optical properties, and snow concentrations may show that OC is a non-negligible absorber in snowpack.

### 4.3.3 Snow Aging

As discussed later, the change in absorbed energy caused by BC depends strongly on snow  $r_e$ , implying that forcing is sensitive to snow aging. We apply an empirical representation of the microphysical model developed in *Flanner and Zender* (2006), which predicts the evolution of snow specific surface area with dependence on snow temperature, temperature gradient, and density. In our model, large temperature gradients can reduce pure snow, spectrally-averaged albedo by up to 0.12 within 14 days, but the influence of temperature gradient is marginalized by cold temperature and high snow density. The predictive aging equation used here is the time derivative of Equation 16 in *Flanner and Zender* (2006):

$$\frac{d\hat{S}}{dt} = \frac{1}{\kappa} \hat{S}_0 \tau^{1/\kappa} (t + \tau)^{-1/\kappa - 1} \quad (4.2)$$

where  $\hat{S}$  is the snow specific surface area,  $\hat{S}_0$  is the fresh snow specific surface area (assumed to be  $60 \text{ m}^2 \text{ kg}^{-1}$ ),  $t$  is the time since snowfall (where snowfall of 10 mm liquid water equivalent completely resets snow age and SSA), and  $\kappa$  and  $\tau$  are best-fit parameters to predictions from the microphysical model, retrieved from a lookup table depending on local snow temperature, temperature gradient, and density. Finally, since effective radius is a surface area-weighted radius,  $r_e = 3/(\hat{S} \rho_i)$ , where  $\rho_i$  is bulk ice density. Model temperature gradient is taken as the mean gradient at the center of each snow layer in CLM, and for snow on sea-ice as the temperature difference between surface air and the mean of sea-ice and snow temperatures, divided by the snow layer thickness. With a single snow layer, CSIM cannot resolve the strong temperature gradient that often exists in near-surface snow, and hence likely underestimates aging. We also add a wet snow grain growth function, based on laboratory measurements,

that is parameterized as a function of liquid water content (*Brun*, 1989). Grain growth from liquid water transfer is still very poorly understood, and this function likely applies only to a limited set of snow condition. To enable wet snow aging in CSIM, we added diagnostic prediction of liquid water content based on net energy balance of snow at the freezing temperature. Our aging parameterization does not treat effects of wind, melt-freeze cycles, and sintering. Large uncertainties remain about snow aging because of the complexity of governing processes and because few quality observational datasets exist to help understand those processes. Hence, we consider half and double the rate of  $r_e$  evolution predicted by SNICAR for our low and high estimates, respectively.

#### 4.3.4 Meltwater Scavenging and Aerosol Removal

Very few studies have examined meltwater scavenging of impurities in snow. CLM accounts for meltwater drainage by adding excess water to the layer beneath when liquid content exceeds the layer’s holding capacity, defined by snow porosity and irreducible water saturation. We assume BC inclusion in meltwater proportional to its mass mixing ratio multiplied by a scavenging factor. Thus, the BC mass rate of change in each layer  $i$  is:

$$\frac{dm_i}{dt} = k (q_{i+1} c_{i+1} - q_i c_i) + D \quad (4.3)$$

where  $m$  is the absolute mass of BC in each layer,  $k$  is the scavenging ratio,  $q_i$  is the mass flux of water out of layer  $i$ ,  $c_i$  is the mass mixing ratio of BC in layer  $i$  (BC mass divided by liquid+solid H<sub>2</sub>O mass), and  $D$  is the sum of wet and dry atmospheric deposition, added only to the surface layer. This equation has similar form to Equation 2 of *Jacobson* (2004b) but is generalized for multiple snow layers and treats removal as a function of meltwater scavenging rather than with an empirical fall speed. After deposition, BC is instantly mixed uniformly in the model surface layer, which never exceeds 2 cm thickness.

*Conway et al.* (1996) applied BC to the surface of melting snow and observed that 99% of hydrophilic BC, and 50% of hydrophobic BC were removed from the top 50 cm of snow after 10 days. Applying a simple e-folding model with total meltwater



production observed during this period, and initial and final BC mass observed in the top 2 cm, we estimate hydrophilic and hydrophobic scavenging ratios of  $k_{\text{phi}} = 0.037$  and  $k_{\text{pho}} = 0.031$ . This estimate of  $k_{\text{phi}}$  is likely too small, because nearly all of the hydrophilic BC retained in the top 50 cm was in the top 2 cm and *Conway et al.* (1996) note that particles larger than  $\sim 5 \mu\text{m}$  are relatively immobile during melt. Therefore, retention of hydrophilic particles near the snow surface is likely because of size rather than particle affinity for water. This is consistent with observations of mineral dust particles (typically larger than BC by 2-3 orders of magnitude) remaining near the surface during snowmelt [*Tom Painter, personal communication, 2006*]. *Conway et al.* (1996) offers unique observations of aerosol transport with snow meltwater, but the spatial and temporal resolution of observations are too coarse, and uncertainty about the role of particle size too large, to estimate scavenging ratios with much confidence. Here, we assume  $k_{\text{pho}} = 0.03$ , derived from observations in the top 2 cm, and apply the  $k_{\text{pho}}/k_{\text{phi}}$  ratio obtained from analysis of observations in the top 50 cm of snow to obtain  $k_{\text{phi}} = 0.20$ . For high and low estimates, we assume an order of magnitude uncertainty (Table 4.1).

In the absence of melt, fresh snowfall in CLM continuously divides the model surface snow layer and prevents excessive BC accumulation. In CSIM, BC accumulates excessively in snow on perennial sea-ice because of the single layer representation and because snow remains perennially on the sea-ice (an issue discussed later). Consequently, we impose empirical BC removal with an e-folding time of 1.44 years, resulting in steady-state interannual concentrations. Future versions of this sea-ice model will have multiple snow layers.

### 4.3.5 Snow Cover Fraction

Snow cover fraction (SCF) controls the area over which BC/snow forcing operates. SCF is generally parameterized as a simple function of snow depth, but also depends on orographic variability, vegetation cover, and melt/accumulation phase [*Z. Liang-Yang, personal communication, 2006*]. We found seven widely-varying SCF representations in the literature and choose the following, based solely on their relative scales, for low, central, and high SCF relationships to snow depth:

- Low:  $\text{SCF} = d/(10z + d)$ . (*Oleson et al.*, 2004) (CLM)
- Central:  $\text{SCF} = \min[1.0, \log(100d + 1)/3.33]$  (*Romanov and Tarpley*, 2004)
- High:  $\text{SCF} = \tanh[d/(2.5z)]$  (*Yang et al.*, 1997)

Here,  $d$  is snow depth (m) and  $z$  is surface roughness length (fixed at 0.01 m for all soil types and glacier surfaces in CLM). Snow depth of 10 cm predicts SCF of 0.47, 0.69, and 0.99 for these three representations, respectively. *Oleson et al.* (2004) is the current implementation in CLM. *Romanov and Tarpley* (2004) relates snow depth, as measured by stations in the U.S. and Canada, to SCF observed by satellite. Their derived relationship is valid for snow depths less than 30 cm over prairies and lightly-forested regions. *Yang et al.* (1997) propose SCF from analysis of six years of station data from six sites in the Former Soviet Union. Improving SCF representation to account for variables other than snow depth is beyond the scope of this study.

Lacking a radiative transfer approximation for BC inclusion in sea-ice, we assume snow forcing acts homogeneously over snow-covered and snow-free ice. This crude assumption probably underestimates forcing, because surface sea-ice is very coarse-grained (e.g. *Light et al.*, 1998), and forcing increasing with increasing  $r_e$ .

## 4.4 Results and Discussion

In this section we first compare spectral albedo from SNICAR with observations and examine sensitivity of snow albedo and subsurface radiative heating to varying BC concentrations and snow effective radii. Next, we analyze GCM experiments with BC in snow, first comparing predicted BC concentrations in snow with observations, then assessing global forcing, and finally examining climate feedbacks.

### 4.4.1 BC Influence on Snow Albedo and Radiative Heating

We first apply offline, single-column, 470-band SNICAR to demonstrate model fidelity in reproducing observed snow reflectance. Figure 4.2 shows measured snow

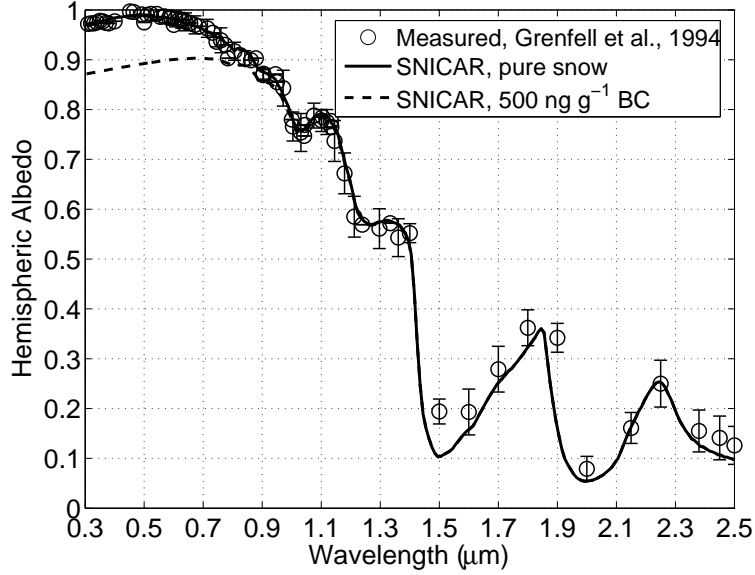


FIGURE 4.2. Measured diffuse incident radiation snow albedo at the South Pole from *Grenfell et al.* (1994) and modeled albedo from SNICAR assuming a 0.25 mm thick surface layer composed of  $45\text{ }\mu\text{m}$   $r_e$  snow and a deep underlying layer of  $100\text{ }\mu\text{m}$   $r_e$  snow. The thin surface layer controls reflectance in the highly-absorptive NIR portion of the spectrum. Also shown is modeled snow reflectance with  $500\text{ ng g}^{-1}$  of hydrophilic (coated) BC.

albedo for diffuse incident radiation at the South Pole (Figure 4 of *Grenfell et al.*, 1994, data provided by Steve Warren) and modeled reflectance using SNICAR with a thin (0.25 mm) surface layer composed of  $45\text{ }\mu\text{m}$   $r_e$  snow and a thick underlying layer composed of  $100\text{ }\mu\text{m}$   $r_e$  (snow density =  $350\text{ kg m}^{-3}$ ). *Grenfell et al.* (1994) found that a similar 2-layer model (with surface  $r_e = 30\text{ }\mu\text{m}$ ) also matched observed reflectance in both the visible and absorptive NIR. Because they did not measure snow grain size at the very high vertical resolution needed for model testing with fully-known snow conditions, *Grenfell et al.* (1994) point out that many arbitrary layer thickness and  $r_e$  model combinations can produce a good fit. Also shown in this figure is modeled albedo of the same snowpack, but with  $500\text{ ng g}^{-1}$  of hydrophilic (coated) BC. The BC strongly reduces visible reflectance, but has negligible influence at wavelengths beyond  $1\text{ }\mu\text{m}$ .

Next, we identify how varying concentrations of BC affect spectrally-averaged ( $0.3 - 5.0\text{ }\mu\text{m}$ ) hemispheric snow albedo and subsurface heating with different  $r_e$ . We assume an optically thick, homogeneous snowpack with direct-beam incident flux at

a solar zenith angle of  $60^\circ$ . *Grenfell et al.* (1994) report that, using the model of *Warren and Wiscombe* (1980), a uniform distribution of  $15 \text{ ng g}^{-1}$  BC reduces albedo by 1% at 500 nm with an effective grain radius of  $100 \mu\text{m}$ . In our model, hydrophobic and hydrophilic BC reduce 500 nm albedo in snow with  $r_e = 100 \mu\text{m}$  by 0.0079 and 0.0108, respectively. The experiments discussed below apply hydrophobic BC optical properties.

Figure 4.3 (top) shows spectrally-averaged snow albedo for BC concentrations ranging from  $0 - 1000 \text{ ng g}^{-1}$ , and four different  $r_e$ . Qualitatively, these curves agree well with Figures 1 and 2 of *Warren and Wiscombe* (1985). As originally noted by *Warren and Wiscombe* (1980), the presence of absorbing impurities reduces albedo more in snow with larger  $r_e$ . Albedo reduction for  $1000 \text{ ng g}^{-1}$  BC is 0.17 and 0.045 for snow with  $r_e = 1000$  and  $50 \mu\text{m}$ , respectively. Both the absolute perturbation from BC and disparity in perturbation between grain sizes grow as zenith angle decreases.

The grain size effect is somewhat counterintuitive, as one naturally expects brighter media to be more susceptible to darkening by impurities. But visible radiation penetrates deeper in snow with larger  $r_e$  because it has a smaller extinction coefficient and, less importantly, scatters more strongly in the forward direction. The snow depth where mean radiative intensity diminishes to  $1/e$  of its surface value is 17 cm for  $r_e = 50 \mu\text{m}$  and 78 cm for  $r_e = 1000 \mu\text{m}$  ( $\lambda = 550 \text{ nm}$ , snow density =  $150 \text{ kg m}^{-3}$ , zenith angle =  $60^\circ$ ). By traveling through a greater optical depth of impurities, photons thus have a greater probability of absorption by (homogeneously-interspersed) impurities in snow with larger  $r_e$ . Sensitivity to grain size highlights the importance of snow aging treatment and realistic  $r_e$ , which can vary significantly on small spatial scales (*Painter et al.*, 2003).

Nearly all albedo reduction from BC is due to increased absorption in the visible spectrum. NIR albedo decreases by only  $0.02 - 0.06$  with  $1000 \text{ ng g}^{-1}$  BC, whereas visible albedo is reduced by  $0.07 - 0.28$  (not shown). This produces another surprising result: with homogeneously mixed BC, the fraction of total absorption occurring more than 2 cm beneath the snow surface *increases* with increasing BC amount, up to a limit. Figure 4.3 (bottom) shows this fraction increasing by up to 0.11 with  $r_e = 1000 \mu\text{m}$ . While BC shifts the visible absorption to nearer the surface, a much greater portion of total absorption is in the visible spectrum. Even with large BC

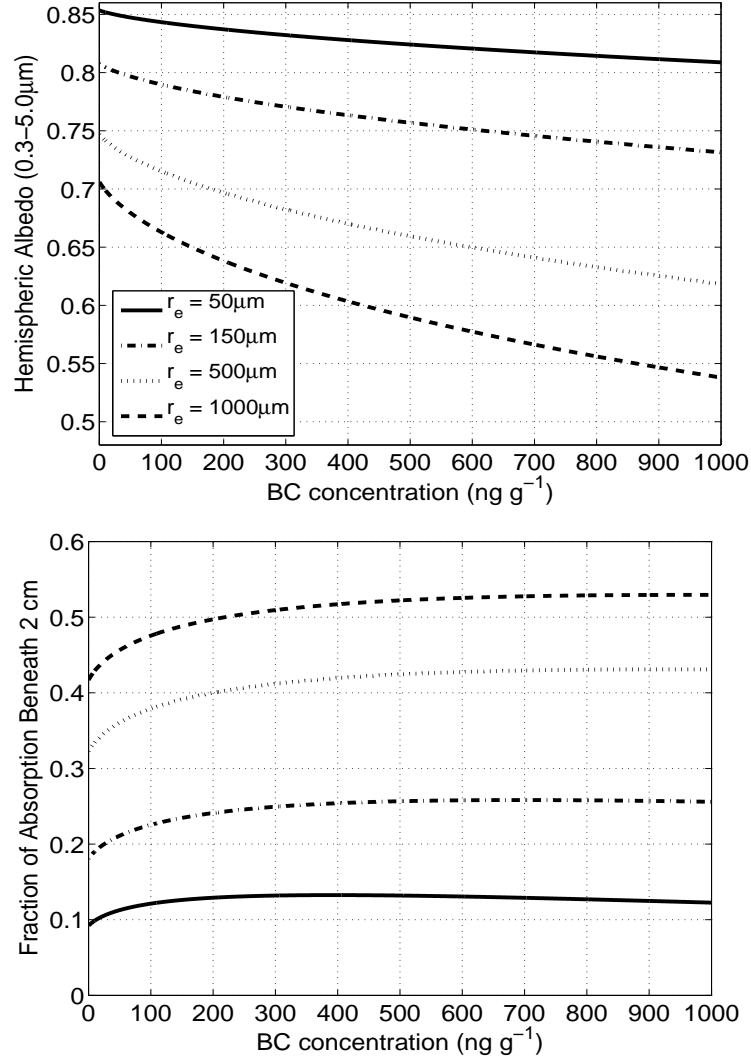


FIGURE 4.3. (top) Spectrally-averaged snow albedo as a function of BC mass concentration for various snow effective radii ( $r_e$ ). Note that BC perturbs albedo more in larger-grained snow. (bottom) Fraction of total snowpack absorption occurring more than 2 cm beneath the surface as a function of BC concentrations for the same  $r_e$  as the top panel. Absorption occurs deeper in the snow with homogeneously-mixed BC because more of the total absorption is from visible radiation, which tends to absorb deeper than NIR, even with large BC concentrations. In both experiments, the snowpack is optically semi-infinite and homogeneous. Incident flux is direct-beam from  $60^\circ$  zenith angle. For comparison of these BC concentrations with global observations and model predictions see Table 4.2 and Figures 4.4 and 4.5.

concentrations, visible absorption tends to occur deeper than NIR absorption. Most NIR absorption occurs in the top 1 mm of snow (*Brandt and Warren, 1993; Flanner and Zender, 2005*). With sufficiently high BC concentrations however, absorption shifts to higher in the snowpack, as can be seen by the slight downward trend in sub-2 cm absorption for  $r_e = 50 \mu\text{m}$  and BC concentrations greater than  $400 \text{ ng g}^{-1}$ . The BC concentration of maximum sub-2 cm absorption depends on  $r_e$  because of the visible depth-penetration dependence on  $r_e$ . If aerosol is more concentrated at the snow surface, however, due to dry deposition or accumulation of impurities near the snow surface during melt, total absorption shifts towards the surface. By influencing sub-surface melt (*Koh and Jordan, 1995*), changes to the vertical distribution of heating can have important influence on snow climatology (*Flanner and Zender, 2005*).

#### 4.4.2 GCM Experiments

We conducted six GCM experiments with BC in snow, using configurations presented in Table 4.1, designated from here on as YYYY low, central, or high experiment, where YYYY is 1998 or 2001. To assess climate response and efficacy, we also completed paired control simulations for the central and high experiments, (YYYY central and high control), identical to the experiments except without BC in snow. Forcing in the low experiments was insufficient to perturb climate. To help constrain efficacy, we also conducted experiment and control simulations with  $10\times$  1998 BC and OC emission inventories (1998  $10\times$  experiment and control), with otherwise central model configurations (Table 4.1). Finally, to help discern the relative forcing contributions from FF, BF, and BB sources, we conducted experiments emitting only FF+BF and FF central estimate sources (FF+BF and FF experiments). All runs apply annually-repeating emissions.

The wide range of climate perturbation in these experiments required different spinup periods for equilibrium. In the discussion that follows, we report results from the final 15 years of 16-year simulations (1998 and 2001 low, FF+BF, and FF experiment), 25-year simulations (1998 and 2001 central experiments and controls), and 35-year simulations (1998 and 2001 high experiments and controls). For the 1998  $10\times$

experiment and control, we analyze the final 20 years of 50-year simulations. The 95% confidence interval of linear trend in global mean 2-meter air temperature ( $T_{2m}$ ) of these 15- and 20-year timeseries included zero for all experiments and controls except 2001 central and high experiments, which both had trends of  $+0.01^{\circ}\text{C yr}^{-1}$ . Because the corresponding controls had no trend, it is possible we underestimated the climate response for these scenarios. Global mean top-of-model (TOM, about 3 mb pressure) radiative energy flux, averaged over the analysis periods, was within  $1 \text{ W m}^{-2}$  of equilibrium for all model runs.

### 4.4.3 Measured and Modeled BC Concentrations in Snow

Table 4.2 summarizes measurements of present-day BC in snowpack from all studies known to the authors. When mean values are not reported in the original literature, we report means of all published measurements from each location. Measurement techniques and uncertainties vary considerably between studies and are discussed to varying degrees in each reference. Most studies utilize optical or thermal/optical techniques, although *Slater et al.* (2002) applies an acid-base/thermal method. Table 4.2 also shows CAM/SNICAR predictions of BC concentrations in the surface snow layer. Data in the lower portion of the table show BC concentrations in precipitation, with model estimates derived from wet deposition and precipitation rates. When the measurements correspond to a particular time of year, we report model predictions from the same months. Otherwise, model results are annual mean estimates. Central estimates for 1998 and 2001 are reported with low–high range in parentheses. A log-log whisker plot of these data is shown in Figure 4.4. The center model point on this plot is the mean of 1998 and 2001 central experiments, and vertical error bar represents the greatest minimum–maximum range from both 1998 and 2001 low and high experiments. Global distributions of model annual mean BC concentrations in surface snow, averaged only when snow is present, are shown in Figure 4.5 for FF+BF and 1998 (FF+BF+BB) central estimates, plotted on a log-scale.

Figure 4.4 shows that central estimate BC/snow predictions capture the nearly 4 orders of magnitude range in observations with no apparent systematic bias. The

TABLE 4.2. Comparison of modeled and measured BC in snow, sea-ice, and precipitation

Site	Reference	Measurement Period	Measured BC [ng g <sup>-1</sup> ] <sup>a</sup>	1998 Model BC central (low–high)	2001 Model BC central (low–high)
Summit, Gr. (72.6°N, 38.5°W)	<i>Slater et al.</i> (2002)	1994-1996	14.6(4.2 – 30.1)	5.2(1.7 – 64.1)	3.5(1.5 – 34.5)
	<i>Cachier</i> (1997)	1991-1995	2.0 – 19.0 <sup>b</sup>		
	<i>Chylek et al.</i> (1995)	1989-1990	2.0(1.5 – 2.7)		
	<i>Cachier and Pertuisol</i> (1994)	1988-1989	1.0 – 4.0 <sup>b</sup>		
Camp Century (77.2°N, 61.1°W)	<i>Chylek et al.</i> (1987)	~ 1985	2.4(2.1 – 2.6)	13.3(1.2 – 26.9)	6.2(0.9 – 19.6)
Dye 3, Gr. (65.2°N, 43.8°W)	<i>Clarke and Noone</i> (1985)	May 1983	6.4(4.3 – 8.5)	11.8(3.6 – 131)	8.2(3.0 – 29.1)
Alert, Canada (83.5°N, 62.5°W)	<i>Clarke and Noone</i> (1985)	Nov.-Dec. 1983	56.9(0 – 127)	2.2(0.9 – 5.9)	2.5(1.0 – 6.0)
Greenland Sea (79.8°N, 4.2°W)	<i>Clarke and Noone</i> (1985)	Jul. 1983	38.7(5.4 – 75.5)	23.9(3.0 – 104)	20.4(3.5 – 93.9)
Spitzbergen (79°N, 12°E)	<i>Clarke and Noone</i> (1985)	May 1983	30.9(6.7 – 52)	12.7(3.7 – 37.0)	7.2(4.6 – 34.4)
Barrow (71.3°N, 156.6°W)	<i>Clarke and Noone</i> (1985)	Apr. 1983, Mar. 1984	22.9(7.3 – 60.4)	9.7(4.1 – 26.4)	8.4(3.2 – 25.4)
Abisko (68.3°N, 18.5°E)	<i>Clarke and Noone</i> (1985)	Mar.-Apr. 1984	33.0(8.8 – 77)	80.7(15.3 – 332)	96.4(19.4 – 279)
Hurricane Hill (48.0°N, 123.5°W)	<i>Clarke and Noone</i> (1985)	Mar. 1984	14.7(10.1 – 18.5)	29.5(7.1 – 101)	35.2(7.1 – 125)
Arctic Ocean (76°N, 165°E)	<i>Grenfell et al.</i> (2002)	Mar.-Apr. 1998	4.4(1 – 9)	8.4(4.2 – 21.8)	5.8(2.4 – 16.7)
Cascades, Wash (~47°N, 121°W)	<i>Grenfell et al.</i> (1981)	Mar. 1980	22 – 59	36.8(6.3 – 86.3)	35.1(6.7 – 85.9)
Halifax, N.S. (45°N, 64°W)	<i>Chylek et al.</i> (1999)	Nov. 1995-Mar. '96	11(4.3 – 32)	84.0(22.0 – 244)	84.9(18.9 – 270)
French Alps (45.4°N, 5.3°E)	<i>Sergent et al.</i> (1993)	winters 1989-'91	161(80 – 280)	165(50.5 – 226)	136(37.7 – 287)
	<i>Sergent et al.</i> (1998)	winters ~1992-'97	123(34 – 247)		
	<i>Fily et al.</i> (1997)	Apr. 1992	482(235 – 826)	394(92.2–) <sup>c</sup>	69.4(32.7 – 498) <sup>c</sup>
	<i>Fily et al.</i> (1997)	Dec. 1992	115(22 – 302)	29.0(37.4 – 349)	43.5(17.6 – 51.5)
West Texas (32°N, 106°W)	<i>Chylek et al.</i> (1987)	1982-'85	10.6(2.2 – 25.4)	31.6(8.4 – 89.6)	15.5(6.4 – 73.0)
Vostok (78.5°S, 106.9°E)	<i>Grenfell et al.</i> (1994)	Dec. 1990-Feb. '91	0.6	1.08(0.07 – 2.1)	0.50(0.07 – 1.8)
Siple Dome (81.7°S, 148.8°W)	<i>Chylek et al.</i> (1987)	1982-'85(?)	2.5(2.3 – 2.9)	0.08(0.04 – 0.68)	0.09(0.04 – 0.51)
South Pole (90°S)	<i>Warren and Clarke</i> (1990)	Jan.-Feb. 1986	0.23(0.10 – 0.34)	0.20(0.07 – 1.23)	0.21(0.06 – 1.2)
BC in Precipitation					
Rural Michigan (45.5°N, 84.7°W)	<i>Cadle and Dasch</i> (1988) <sup>d</sup>	Dec.-Apr 1984-'85	72(28 – 210)	50(22 – 108)	46(21 – 98)
Urban Michigan (42.5°N, 83°W)	<i>Dasch and Cadle</i> (1989) <sup>d</sup>	Jan.-Apr 1984-'85	160(17 – 5700)	57(26 – 132)	53(23 – 113)
Lithuania (55.5°N, 21°E)	<i>Armalis</i> (1999) <sup>e</sup>	Dec. 1986-Jun. '90	100(8 – 530)	61(22 – 177)	56(20 – 179)

<sup>a</sup> When mean values are not reported in the original literature, we report means of all published values from each location<sup>b</sup> as reported in *Slater et al.* (2002)<sup>c</sup> model results from March used in place of April; no March snow in 1998 high experiment<sup>d</sup> snow precipitation<sup>e</sup> snow+rain precipitation



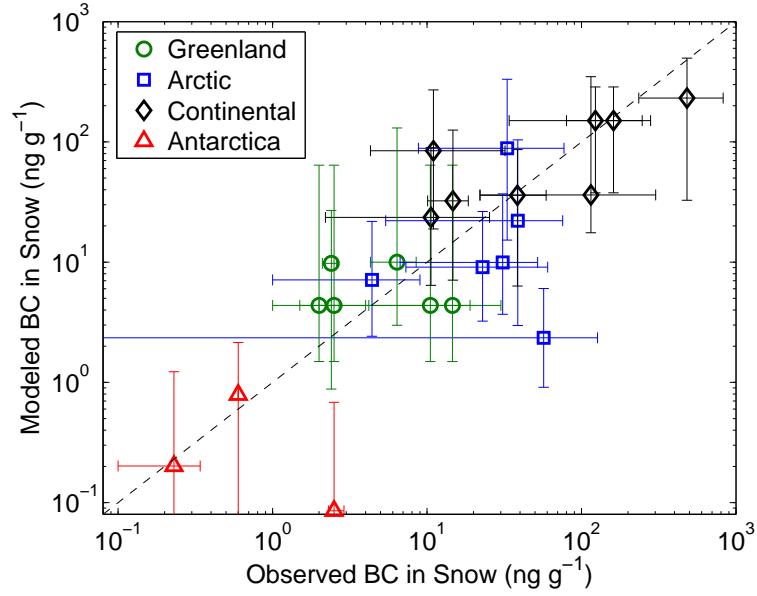


FIGURE 4.4. Model vs. observed BC concentrations in near-surface snow for data from Table 4.2, grouped by region (precipitation measurements excluded). Model data are from the top 2 cm of snowpack. The center model point on this plot is the mean of 1998 and 2001 central experiments. The upper extent of the model error bar represents the maximum of 1998 and 2001 high experiments, whereas the lower extent is the minimum of both low experiments. The correlation coefficient of the log of these data is 0.78.

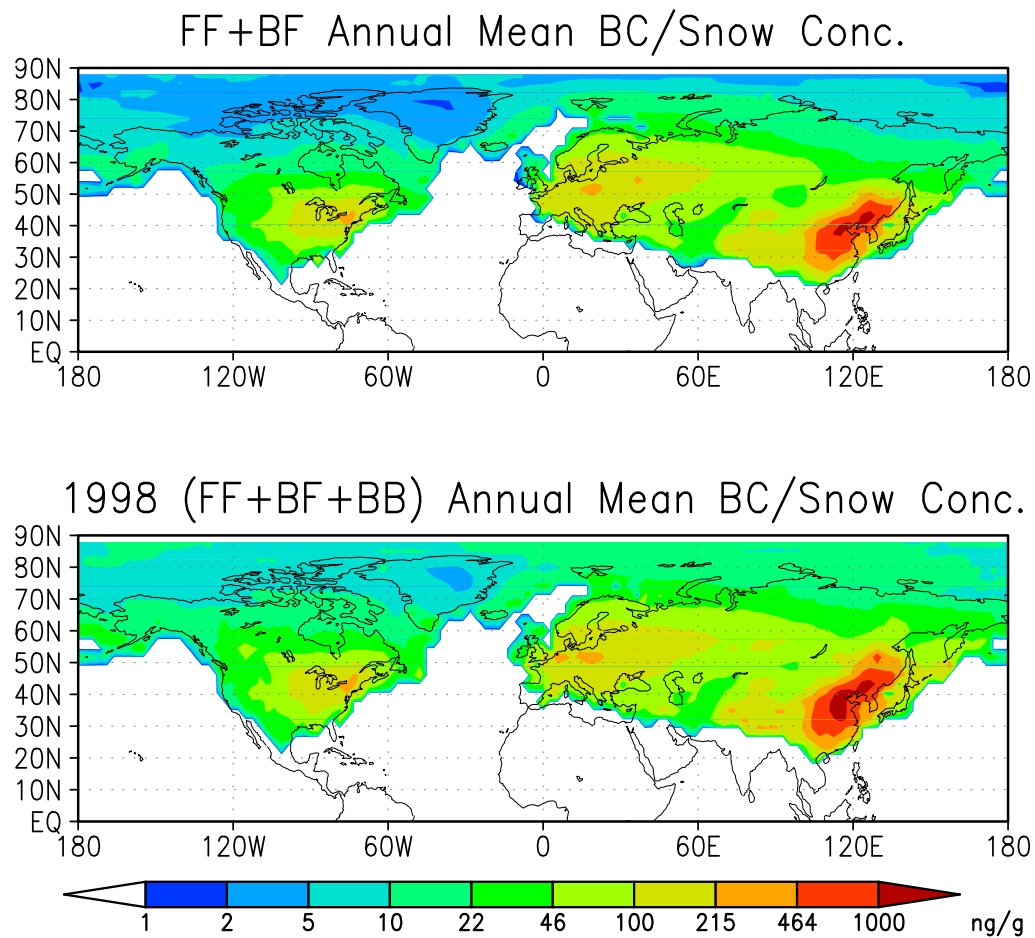


FIGURE 4.5. Annual mean predicted BC concentrations in snow (ng BC per g of ice) using central estimate (top) fossil fuel and biofuel sources only, and (bottom) fossil fuel, biofuel, and 1998 biomass burning emission sources.

correlation coefficient of the log of central model estimates and mean observations is 0.78. Furthermore, in nearly all cases there is some overlap between the range of measurements and low-high model predictions.

Central model predictions are within the range of observations on Greenland and Antarctica, indicating reasonable model long-range BC transport. An exception is Siple Dome, where *Chylek et al.* (1987) report measurements an order of magnitude greater than more recent Antarctic observations (*Warren and Clarke*, 1990; *Grenfell et al.*, 1994). Measurements in Table 4.2 are not time-resolved, except for *Slater et al.* (2002), who reports elemental carbon (EC, often considered synonymous with BC) concentrations with quarter-annual resolution, varying from 4 – 30 ng g<sup>-1</sup> over the course of two years. EC concentration spike in the fall of 1994, although <sup>14</sup>C analysis shows a predominantly fossil fuel-derived source. At Summit, monthly-mean BC concentrations vary from 2 – 10 and 7 – 330 ng g<sup>-1</sup> in our 1998 central and high estimate experiments, respectively, peaking in August and July.

None of the measurements overlap our two years of emission scenarios. Because of interannual variability in biomass burning and trends in regional fossil fuel use, validity of this model-measurement comparison is therefore reduced. For example, our predictions are lower than four arctic measurements (*Clarke and Noone*, 1985) made in the early 1980's, when BC emissions from the Former Soviet Union were much greater than today (*Novakov et al.*, 2003).

Conversely, predictions exceed measurements at Abisko (Sweden), Hurricane Hill (Washington) (*Clarke and Noone*, 1985), and Halifax (*Chylek et al.*, 1999). While Hurricane Hill may be representative of long-range transport because of prevailing westerlies, it is in the same model gridcell as Seattle and has a large local source. Measurements east of Seattle by *Grenfell et al.* (1981) show double the concentrations from Hurricane Hill, in accord with central model predictions. Halifax has a smaller, but still significant local source. *Chylek et al.* (1999) specifically measure urban areas, however, so our model may have a high-bias in this region. Low predictions are in range of measurements at Halifax and Abisko. In the French Alps near Grenoble, central model estimates agree well with *Sergent et al.* (1993) and *Sergent et al.* (1998), but are lower than *Fily et al.* (1997). Central estimates of BC concentrations in precipitation are within range of measurements in rural Michigan (*Cadle and Dasch*,

1988) and Lithuania (*Armališ*, 1999), although are lower than measurements made near Detroit (*Dasch and Cadle*, 1989).

The largest predicted BC concentrations in snow are in northeast China (Figure 4.5), near strong industrial sources. There, concentrations in excess of  $1000 \text{ ng g}^{-1}$  can lower snow albedo by more than 0.13. Annual mean concentrations in the eastern U.S. and Europe exceed  $100 \text{ ng g}^{-1}$ , enough to lower snow albedo by  $> 0.03$ , depending on  $r_e$ . While fossil fuel-derived BC is the dominant source of mid-latitude BC in snow, the effect of strong 1998 wildfires can be seen across the Arctic and Greenland (Figure 4.5). Annual mean BC concentrations in snow averaged over Greenland are 44% greater in 1998 than 2001. Comparing with the FF+BF simulation, we estimate that 43% and 24% of the annual mean BC in arctic snow ( $66.5-90^\circ\text{N}$ ) is from biomass sources in 1998 and 2001, respectively. During summer (June, July, August) these BB source fractions rise to 60% and 36%.

Summer atmospheric conditions favor enhanced wet and dry arctic BC deposition rates (*Stohl*, 2006), implying greater summer BC concentrations in snow regardless of temporal variability in emissions. *Koch and Hansen* (2005) predict that south Asia is the largest source of tropospheric arctic BC, but *Stohl* (2006) contests this and predicts that biomass sources dominate summer arctic BC using a mean 1980's burning inventory (*Lavoue et al.*, 2000). *Stohl* (2006) also suggests that Siberian fires, and northern Eurasia sources in general, can reach the Arctic more easily than emissions from other regions of similar latitude. Future studies should use re-analysis winds to study the impact of individual fire events.

#### 4.4.4 Global Mean Forcing and Response

Table 4.3 lists for all experiments (from left to right) the global mean instantaneous surface forcing from BC in snow ( $F_{s,\text{snow}}$ ), the fraction of  $F_{s,\text{snow}}$  acting over land (where the remaining fraction operates over sea-ice),  $F_{s,\text{snow}}$  averaged temporally and spatially only over snow-covered land surface,  $F_{s,\text{snow}}$  averaged only over sea-ice, the change in global annual mean  $T_{2\text{m}}$  ( $\Delta T_{2\text{m}}$ ) relative to control simulations without BC in snow, forcing “efficacy,” and finally top-of-model (TOM) forcings from atmospheric BC+OC ( $F_{t,\text{atm}}$ ). Efficacy is defined as (*Hansen et al.*, 2005):

TABLE 4.3. Summary of model experiment results

Model Scenario	$F_{s,\text{snow}}^a$ [W m <sup>-2</sup> ]	Land frac. <sup>b</sup> of $F_{s,\text{snow}}$	$F_{s,\text{snow}}$ LAND <sup>c</sup> [W m <sup>-2</sup> ]	$F_{s,\text{snow}}$ ICE <sup>d</sup> [W m <sup>-2</sup> ]	$\Delta T_{2m}^e$ [°C]	Efficacy <sup>f</sup>	$F_{t,\text{atm}}^g$ [W m <sup>-2</sup> ]
1998 low	+0.007 ± 8%	0.73	+0.08	+0.04	—	—	+0.07 ± 14%
1998 central	+0.054 ± 7%	0.82	+0.60	+0.23	+0.15 ± 0.03	4.52 <sup>+0.98</sup> <sub>-0.97</sub>	+0.37 ± 2%
1998 high	+0.131 ± 6%	0.83	+1.56	+0.79	+0.23 ± 0.02	2.83 <sup>+0.35</sup> <sub>-0.34</sub>	+1.31 ± 1%
2001 low	+0.007 ± 9%	0.74	+0.07	+0.04	—	—	+0.05 ± 11%
2001 central	+0.049 ± 7%	0.83	+0.55	+0.20	+0.10 ± 0.03	3.29 <sup>+1.12</sup> <sub>-1.11</sub>	+0.28 ± 2%
2001 high	+0.122 ± 6%	0.83	+1.42	+0.75	+0.16 ± 0.03	2.11 <sup>+0.37</sup> <sub>-0.37</sub>	+1.09 ± 1%
FF+BF	+0.043 ± 5%	0.85	+0.48	+0.15	—	—	+0.19 ± 5%
FF	+0.033 ± 6%	0.85	+0.26	+0.12	—	—	+0.10 ± 4%
1998 10×	+0.277 ± 3%	0.77	+2.90	+1.11	+0.54 ± 0.02	3.11 <sup>+0.15</sup> <sub>-0.14</sub>	+4.96 ± 1%

<sup>a</sup> Global annual mean of BC/snow instantaneous surface forcing<sup>b</sup> Fraction of  $F_{s,\text{snow}}$  acting over land<sup>c</sup>  $F_{s,\text{snow}}$  averaged spatially and temporally only over land snowpack<sup>d</sup>  $F_{s,\text{snow}}$  averaged spatially and temporally only over snow on sea-ice<sup>e</sup> Equilibrium change in global annual mean  $T_{2m}$  relative to control simulations without BC in snow<sup>f</sup> (See Equation 4.4)<sup>g</sup> Global annual mean top-of-model (TOM) forcing from atmospheric BC+OC

$$E = \frac{\Delta T_s / F_a}{\Delta T_s(\text{CO}_2) / F_a(\text{CO}_2)} \quad (4.4)$$

where  $F_a$  is the forcing at the tropopause after stratospheric adjustment (e.g., *Hansen et al.*, 1997) and  $\Delta T_s$  is the change in global mean surface air temperature. The denominator is the response-to-forcing ratio from  $\text{CO}_2$ . *Hansen et al.* (2005) use forcing and temperature response from  $1.5\times$  pre-industrial  $\text{CO}_2$  levels. We apply CAM3 slab ocean model results from *Kiehl et al.* (2006), who report  $F_a(\text{CO}_2) = 3.58 \text{ W m}^{-2}$  and equilibrium  $\Delta T_s(\text{CO}_2) = 2.47^\circ\text{C}$  from a doubling of  $\text{CO}_2$  (355 – 710 ppm). In deriving  $F_a$  from  $F_{\text{s,snow}}$ , we assume that instantaneous forcing at the tropopause ( $F_i$ ) is  $0.91 F_{\text{s,snow}}$ , and that  $F_a$  is equal to  $F_i$  (e.g., there is negligible immediate stratospheric radiative adjustment to the surface forcing). The first assumption is derived from numerous offline experiments with SWNB (*Zender et al.*, 1997). We examined the change in net solar energy at 132 mb relative to that at the surface ( $F_i/F_s$ ) for slight reductions in visible surface albedo of a typical snow surface (initial visible and NIR albedos of 0.97 and 0.60). With zenith angle varying from  $20 - 70^\circ$ , cloud extinction optical depth  $\tau_{\text{cld}}$  varying from  $0 - 50$ , and visible albedo reduction varying from  $0 - 0.10$ , the ratio  $F_i/F_s$  varies only from  $0.94 - 0.96$ . While  $F_s$  is substantially reduced under cloudy skies,  $F_i/F_s$  remains large and constant. However, absorbing aerosol significantly reduces  $F_i/F_s$ , particularly when it resides beneath a cloud, as multiple scattering between snow and cloud enhances absorption by the aerosol. Absorption optical depth  $\tau_a = 0.05$  ( $\lambda = 550 \text{ nm}$ ) can reduce  $F_i/F_s$  to 0.44. But assuming global mean  $\tau_a = 0.0096$  inferred from AERONET scaling of aerosol climatologies (*Sato et al.*, 2003; *Koch*, 2001),  $\tau_{\text{cld}} = 5$ , and zenith angle of  $60^\circ$ , we estimate  $F_i/F_s = 0.91$ , which we apply to derive efficacy. The ranges reported in Table 4.3 represent standard deviation in the annual-mean timeseries. The reported range of  $\Delta T_{2\text{m}}$  assumes unpaired pools (of global mean temperature from each year of equilibrium simulation) with equal variance. Efficacy standard error combines, in quadrature, standard deviations of  $F_{\text{s,snow}}$  and  $\Delta T_{2\text{m}}$ . Support for our second assumption (that  $F_a$  equals  $F_i$ ) comes from *Hansen et al.* (2005), who report  $F_a$  for BC/snow forcing within 2% of  $F_i$ .

Table 4.3 shows that global BC/snow forcing is small relative to forcing from atmospheric BC+OC (columns 'a' and 'g' in Table 4.3). When  $F_{\text{s,snow}}$  is averaged spatially

and temporally only over snow, however, central estimates suggest that  $0.55 - 0.60$  additional  $\text{W m}^{-2}$  are absorbed by snowpack on land and  $0.20 - 0.23 \text{ W m}^{-2}$  by sea-ice because of the immediate presence of BC in snowpack. Our central estimates of  $F_{\text{s,snow}} = +0.054$  and  $+0.049 \text{ W m}^{-2}$  predict  $\sim 10\%$  greater forcing in 1998 than 2001. Comparison with the FF+BF run suggests that about 20% of the total forcing can be attributed to biomass burning in 1998 and 12% in 2001. Estimates from *Hansen and Nazarenko* (2004) of  $F_{\text{a}} = +0.16 \text{ W m}^{-2}$  were downgraded to  $+0.05 \text{ W m}^{-2}$  (*Hansen et al.*, 2005, corrected result published in Appendix A.5 of *Hansen et al.* (2006)). The latter estimate is derived from spatially-varying BC deposition, but without a detailed radiative transfer solution for snow with BC.

An estimate of  $F_{\text{a}}$  from FF+BF BC in snow and ice from *Jacobson* (2004b) is  $+0.06 \text{ W m}^{-2}$  [*Mark Jacobson, personal communication, 2006*], greater than our estimate of  $+0.039 \text{ W m}^{-2}$  ( $0.91 \times 0.043 \text{ W m}^{-2}$ ). *Jacobson* (2004b) treats BC in snow with a radiative transfer approximation, but prescribes spatially and temporally uniform snow grain size and an empirical fall-speed for BC removal from snowpack. Atmospheric aerosol and cloud physical processes are highly sophisticated in *Jacobson* (2004b), however. Size-resolved BC and hydrometeors (including graupel) interact in clouds and precipitation through nucleation and coagulation, and both first and second aerosol/cloud indirect effects are treated. These processes enable prediction of more realistic size distribution and mixing state of BC deposited on snow. Because BC ages rapidly in our model relative to the transport time from source to remote snow surface, 87% of the BC deposited on snow is via wet deposition (providing a minimum estimate of the hydrophilic BC fraction in snow). This is less than the 98% BC wet deposition fraction on snow reported by *Jacobson* (2004b), but likely greater than *Koch and Hansen* (2005), who report that dry deposition is responsible for the majority of BC landing on Greenland. Model differences could be due to several reasons, including more explicit treatment of size-resolved in-cloud scavenging processes by *Jacobson* (2004b), different dry deposition velocities, and different spatial pattern of emissions relative to model snow cover.

While  $F_{\text{s,snow}}$  is small globally, its efficacy is very large. Mean efficacy from the 5 experiment/control pairs in Table 4.3 is  $3.17(2.1 - 4.5)$ . Because the temperature signal/noise ratio is small for realistic (e.g., central estimate) BC/snow forcing, the

1998 10 $\times$  experiment and control provide a more constrained efficacy estimate. (More years of analysis also improve statistical constraint of the temperature response). Tight agreement between 1998 10 $\times$  efficacy and the mean of the other experiments is also encouraging. We caution, however, that efficacy does not necessarily scale linearly with forcing magnitude for a given agent (Figure 25 of *Hansen et al.*, 2005). Global mean  $T_{2m}$  cooled several degrees before achieving steady-state in both 1998 10 $\times$  experiment and control runs because of extreme atmospheric aerosol optical depth, in spite of a positive TOM aerosol forcing.

*Hansen et al.* (2005) report similarly large BC/snow efficacy of 2.7 (corrected result in Appendix A.5 of *Hansen et al.* (2006)), the largest efficacy of all forcings studied. Conversely, mean efficacy of atmospheric BC ( $\sim 0.69$ ) is less than CO<sub>2</sub> (*Hansen et al.*, 2005). Possible reasons for even greater BC/snow efficacy in our study include 1) greater albedo change sensitivity to temperature change in the IPCC AR4 NCAR model relative to the GISS model (*Qu and Hall*, 2006), 2) representation in our model of impurity accumulation near the surface during spring melt, which enhances the forcing precisely when it can have the largest impact on snowmelt and thus snow-albedo feedback, and 3) representation in our model of dynamic snow grain growth, which is enhanced by excess snowpack heating from BC. Better constraint on efficacy will require larger ensembles of GCM simulations with varying initial conditions, and is beyond the scope of this study.

Forcing from atmospheric BC+OC ( $F_{t,atm}$ ) is about 5 – 6 $\times$  greater than BC in snow (Table 4.3). However, if forcings are scaled by their respective efficacies, as *Hansen et al.* (2005) suggest, the resulting atmospheric BC+OC and BC/snow “effective” forcings are of similar magnitude. Much of the forcing from atmospheric BC is offset by OC, which is emitted simultaneously as BC in greater proportion, and which strongly scatters solar radiation. The net effect of atmospheric BC+OC forcing depends on aerosol optical properties, relative aerosol quantities, and reflectance of the underlying surface (e.g., *Ramanathan et al.*, 2001). The OC/BC emission ratio is smaller in FF combustion than BB (e.g., *Bond et al.*, 2004). Hence, net radiative forcing from FF BC+OC is positive (e.g., *Jacobson*, 2001), whereas the sign of net forcing from BB BC+OC could be positive (e.g. *Hansen et al.*, 2005) or negative (e.g., *Myhre et al.*, 2003), depending especially on whether aerosol is lofted above clouds,



where it is much more likely to have positive forcing. However, many other scattering aerosols are emitted in significant quantity from biomass burning, leading *Jacobson* (2004a) to suggest a global net surface cooling effect from all biomass burning aerosols. In our study, biomass burning contributes a much greater portion to  $F_{t,atm}$  (49% and 32% in 1998 and 2001 central estimates, respectively) than to  $F_{s,snow}$  (Table 4.3). Atmospheric aerosol forcing is not the focus of this study though, so we refrain from a detailed analysis.

#### 4.4.5 Spatial/Temporal Climate Response Patterns

The primary reason why BC/snow forcing is so efficacious is its ability to trigger snow-albedo feedback. Here, we look at spatial and temporal distributions of forcing, snowmelt, albedo change, and temperature response to assess this feedback.

Figure 4.6 depicts the northern hemisphere distribution of annual mean surface forcing from BC in snow for 1998. The top panel shows mean gridcell forcing, which depends on snow cover fraction. The bottom panel shows forcing averaged only over snow covered surface within each gridcell, irrespective of SCF, and averaged only when snow is present. This metric describes the quantity of energy added specifically to snowpack, providing some insight into how local snowpack evolution may be affected. However, because model snow depth is very low in regions of low snow spatial coverage, and because forcing is reduced with shallow snowpack because of the radiative influence of the underlying ground, the snow-only forcing is significantly underestimated in unresolved mountainous terrain that should have deep snowpack. This deficiency can also be gleaned by noting very low snow-only forcing in the southern-most regions of model snow cover, where Figure 4.5 depicts large annual mean BC concentrations. The largest forcing is over the Tibetan Plateau (30 – 40°N, 80 – 100°E), averaging  $1.5 \text{ W m}^{-2}$  over all-land. Forcing over northeastern China and much of Eurasia becomes larger when considering snow-only forcing, as expected from large BC/snow concentrations (Figure 4.5) but modest snow cover fraction. During some spring months, snow-only forcing exceeds 10 and  $20 \text{ W m}^{-2}$  over parts of eastern China and the Tibetan Plateau, respectively. Even though BC mixing ratios and albedo reductions are greater in northeastern China, forcing is greater over the

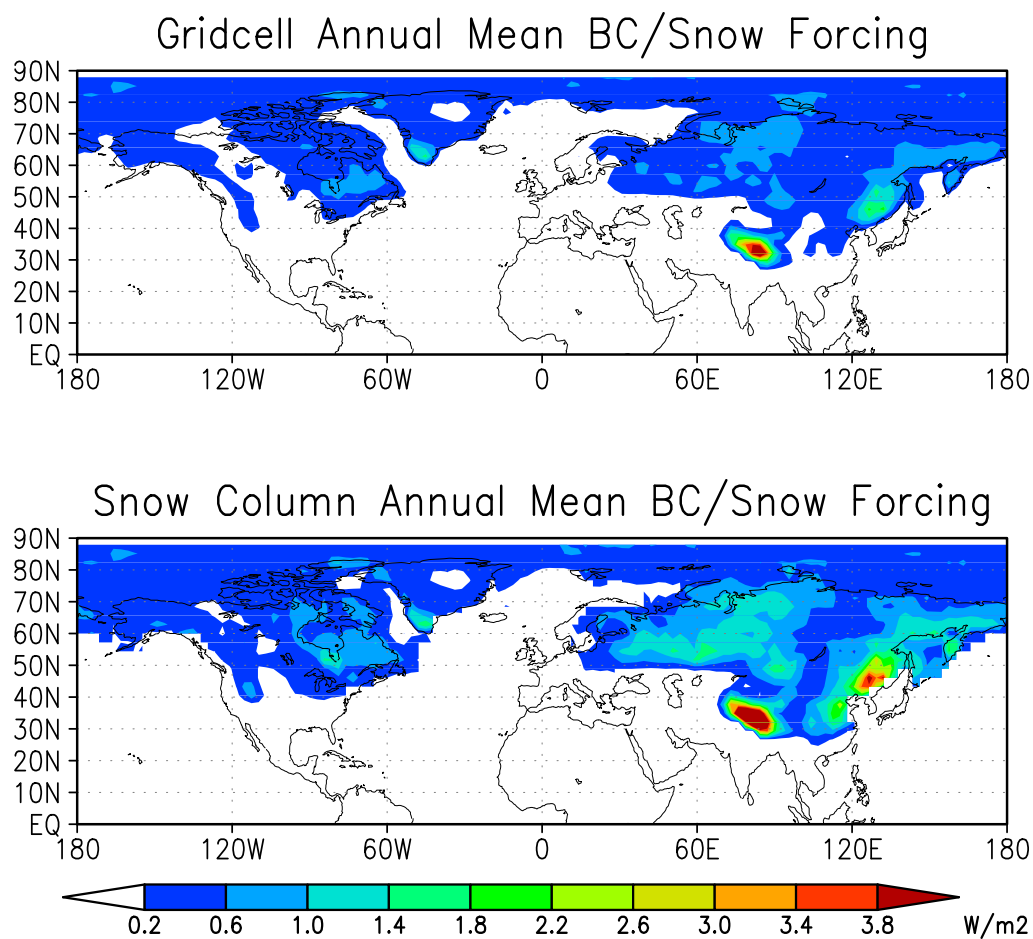


FIGURE 4.6. Central estimates of 1998 surface forcing ( $\text{W m}^{-2}$ ) from BC in snow; (top) annual mean gridcell forcing, representing the true climate forcing; (bottom) forcing averaged spatially and temporally over only snow-covered surface, representing the mean increase in energy absorption by snowpack.

Tibetan Plateau because of greater ground-incident solar flux (because of closer proximity to the equator and less vegetation cover). More than 98% of the global forcing operates in the northern hemisphere.

Maximum BC/snow forcing occurs with the combination of high BC concentrations in snow, surface-incident solar flux, and snow cover. This pattern is manifested in Figure 4.7, which shows northern hemisphere zonal, monthly mean surface forcing from BC in snow for 1998 and 2001 central estimates and derived estimates of the 1998 biomass burning contribution. The latitude of maximum forcing moves north as the spring progresses, following regions with large amounts of snow and incident sunlight. While BC emissions are consistent or stronger in fall than spring (1998 boreal fire intensity peaked in August and September), seasonal snowpack does not generally form before incident sunlight significantly diminishes, thus greatly reducing forcing during the accumulation phase. 1998 arctic BC concentrations in snow peak in August, as opposed to July in 2001, attributable to boreal fires. But  $80 - 90^{\circ}\text{N}$  surface-incident solar flux drops to only 96 and  $26 \text{ W m}^{-2}$  in August and September, reducing the radiative forcing potential. Thus April–June boreal fires have the greatest potential for strong BC/snow forcing. A second reason for greater forcing during the snow melt phase is accumulation of impurities near the surface. This effect is controlled by the scavenging ratio (Table 4.1), which is largely unconstrained.

The forcing space-time pattern in Figure 4.7 coincides closely with that of snowmelt onset. Thus, BC/snow forcing, while generally small, is maximum precisely when it can have the greatest influence on snowmelt rate. Zonal-mean forcing is large at high-latitudes, even though BC concentrations are lower, because a greater portion of the surface is snow-covered. Arctic forcing is 17% greater in 1998 than 2001, and we attribute 35% of the total arctic forcing to biomass burning in 1998.

Strong evidence for BC influence on snowmelt timing is seen in Figure 4.8, which shows change in zonal mean snowmelt rate (averaged over land only), resulting from inclusion of BC in snow. Hatching shows statistically significant change at the 0.01 level. High latitude melt rate clearly increases during the early snowmelt phase and decreases during the late melt phase, as there is less snow available. Quantified one way, zonal mean melt rate increases in the experiments by 8 – 54% in the month prior to maximum melt of the controls at latitudes north of  $50^{\circ}\text{N}$ . Area-weighted,

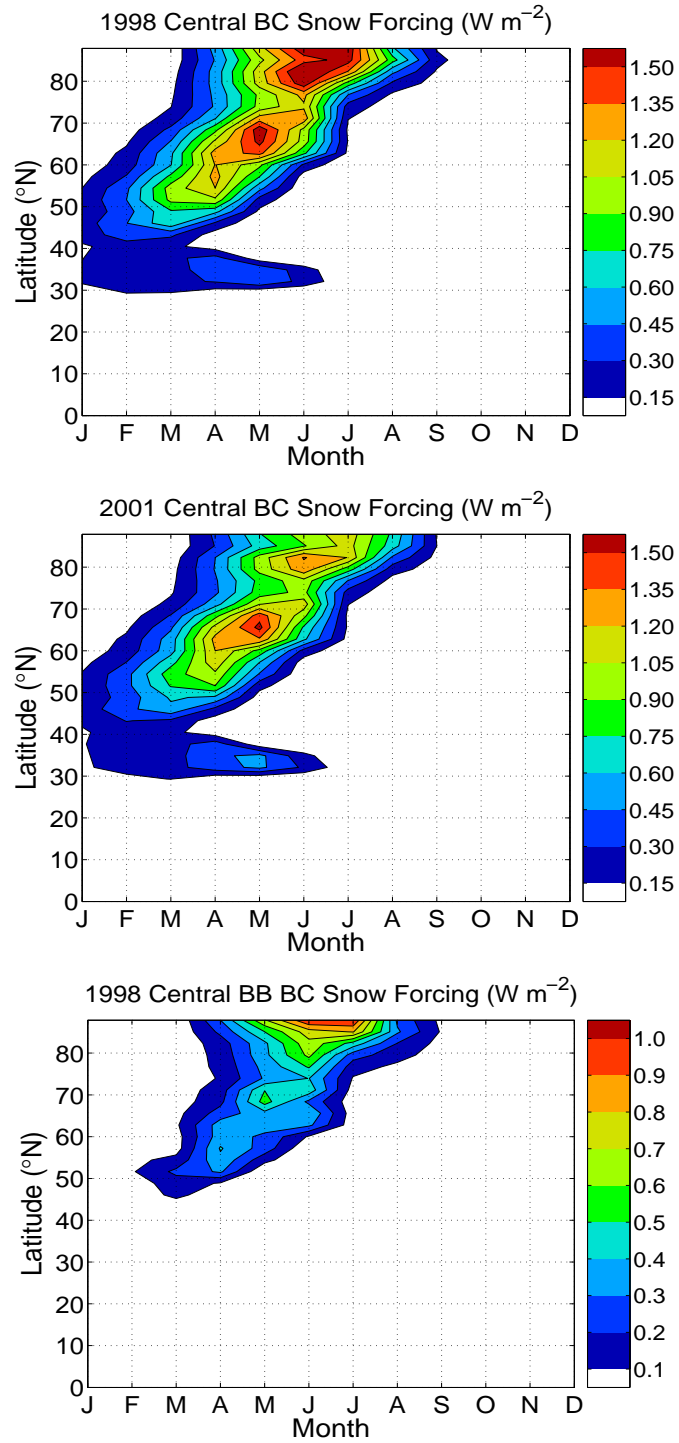


FIGURE 4.7. Zonal mean surface forcing from BC in snow as a function of month and latitude for (top) 1998 and (middle) 2001 central estimates, and (bottom) 1998 biomass burning only. The biomass burning forcing contribution is estimated as the difference between 1998 central (FF+BF+BB) and FF+BF only forcing.

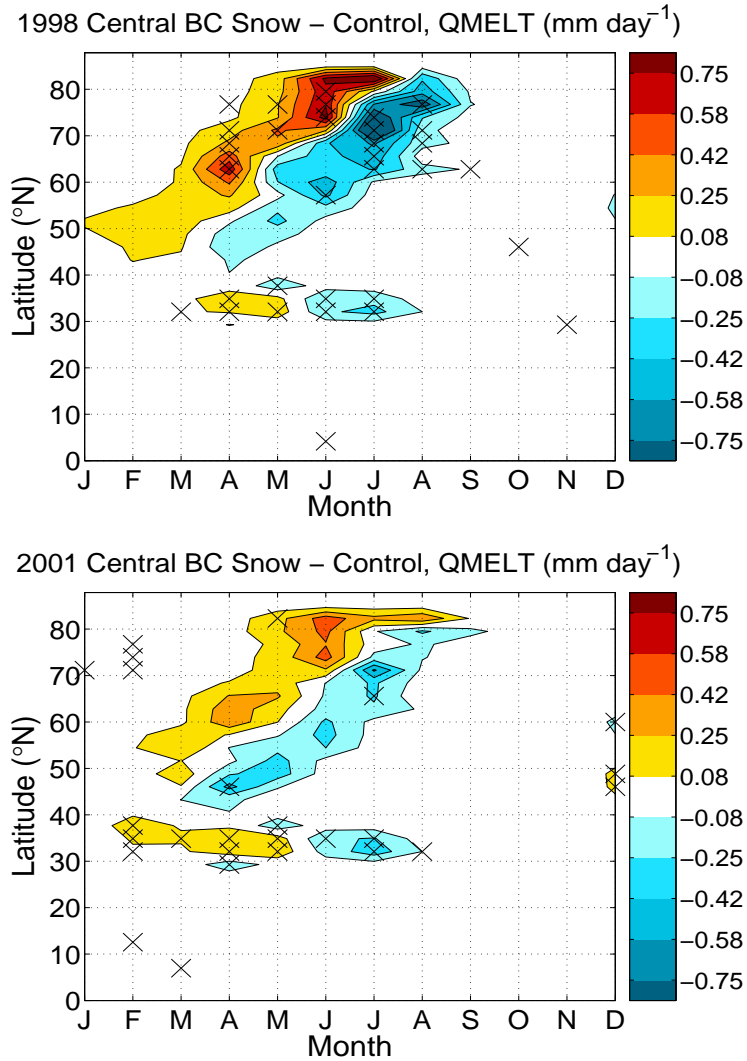


FIGURE 4.8. Difference in zonal monthly mean land snowmelt rate between central experiments and their respective controls. Experiment and control are identical except that BC only affects snow reflectance and heating in the experiment. Hatching shows statistically significant change at the 0.01 level.

this increase is 28% and 19% for 1998 and 2001, respectively. Figure 4.8 shows that statistically significant melt changes are more widespread in 1998 than 2001.

Surface snowmelt on Greenland has been shown to increase the rate of ice-sheet flow (*Zwally et al.*, 2002). Summer mean melt rate averaged over Greenland is 3% and 13% greater in 1998 and 2001 central experiments than their respective controls, but these changes are not significant at the 0.05 level. Summer  $T_{2m}$  warming over Greenland is  $0.44^{\circ}\text{C}$  in both central experiments. Corresponding warming in both 1998 and 2001 high experiments is  $1.15^{\circ}\text{C}$ , and melt rate changes are both significant at the 0.05 level. Central and high estimates of BC in Antarctic snow are too low to have significant influence on snow albedo, but we wonder if strong Australian wildfires could have a noticeable effect.

Along with snowmelt changes are highly significant reductions in zonal mean surface albedo. Figure 4.9 shows these changes, averaged over land and ocean, with hatching again at 0.01 significance. Annual mean albedo (weighted by surface insolation) of all arctic surface is reduced by 0.047 and 0.017 in 1998 and 2001 central experiments, respectively. The late-summer (August–September) 0.10 – 0.18 reduction in  $80^{\circ} - 90^{\circ}\text{N}$  1998 albedo happens because summer snow depth on sea-ice is reduced by 72%, exposing the darker bare sea-ice. This large reduction follows the  $1.5 \text{ W m}^{-2}$  June–July BC/snow forcing (Figure 4.7).

Observations spanning 1954–1991 from Soviet drifting stations indicate that snow on top of perennial sea-ice is generally nearly gone by July or August (*Warren et al.*, 1999). SHEBA observations from 1998 show snow ablation by early July (*Perovich et al.*, 2002), whereas model snow depth reaches August minimums of 29 and 13 cm in 1998 and 2001 central control simulations, respectively, and 5 and 11 cm in 1998 and 2001 central experiments. These observations indicate a model tendency of excessive snow cover on late-summer sea-ice. Perhaps encouragingly, the inclusion of BC in snow reduces model snow depth.

Excess snowpack heating and climate feedback in the model also appear to accelerate snow grain growth, which darkens the snow itself and enhances the perturbation from BC (Figure 4.3). The increase in  $80^{\circ} - 90^{\circ}\text{N}$  June and July  $r_e$  relative to 1998 central control is  $289 \mu\text{m}$ . The forcing responsible for this feedback is largely from

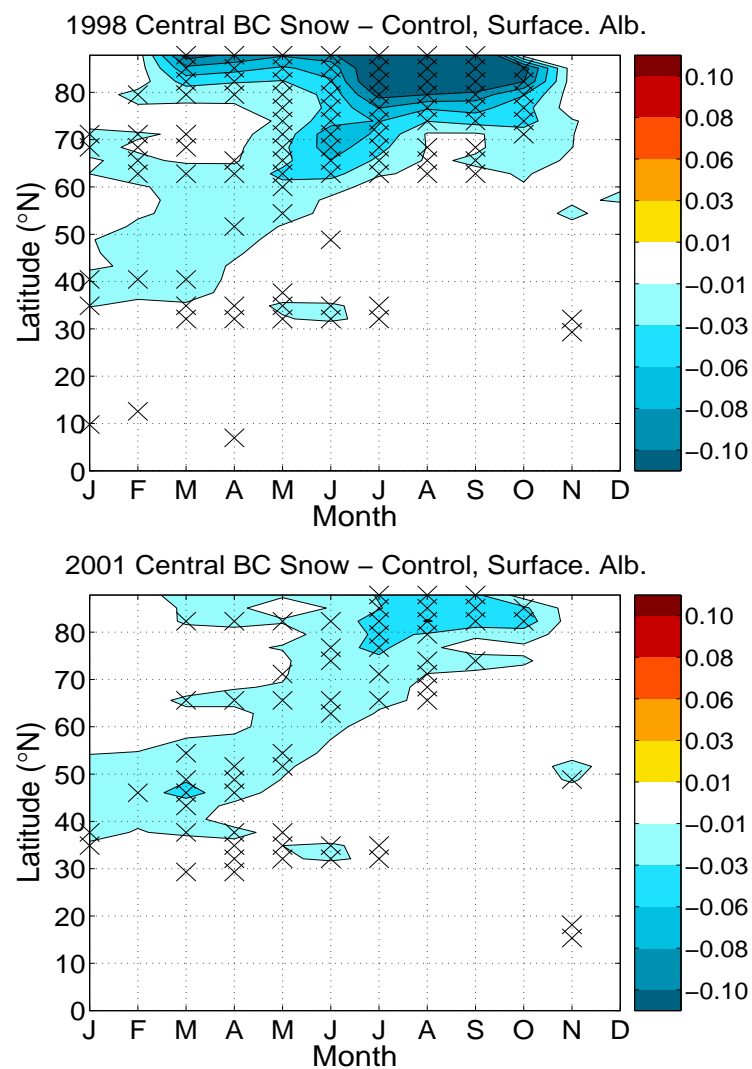


FIGURE 4.9. Difference in zonal monthly mean surface albedo between central BC/snow experiments and their respective controls. Hatching shows statistically significant change at the 0.01 level.

biomass burning and is clearly damped in the 2001 central experiment (Figure 4.7), where  $80 - 90^\circ\text{N}$  June and July  $r_e$  is only  $52\mu\text{m}$  greater than 2001 central control, summer snow depth on sea-ice reduced by only 13%, and late-summer albedo reduced by 0.05. Note that these results are sensitive to the CSIM snow height/SCF relationship (*Briegleb et al.*, 2004), which determines the proportion of exposed bare sea-ice. Slight changes to snow depths less than 10 cm have large impact on SCF and therefore albedo. In spite of large albedo reduction, sea-ice area changes are small. July–September mean arctic ( $66.5 - 90^\circ\text{N}$ ) sea-ice coverage is reduced by 3% and 1% in these two experiments relative to their respective control simulations.

Finally, Figure 4.10 shows significant surface air warming from BC in snow, especially from  $60 - 90^\circ\text{N}$  during June–November, 1998. Annual mean  $T_{2\text{m}}$  warming averaged over the Arctic is  $+1.61$  and  $+0.50^\circ\text{C}$  for 1998 and 2001. The late-summer polar warming pattern in 1998 is logically coupled with the forcing and albedo change patterns described above. 1998 winter and spring warming may be a consequence of thermal inertia from fall warming, or could be dynamical in nature. We note that our 1998 central experiment showed the highest efficacy of all experiments, so we urge caution in assuming that the large responses discussed are due entirely to biomass burning emissions, which cause only a modest increase in forcing (Figure 4.7c).

These changes provide evidence that significant snow-albedo feedback occurs from BC in snow, even though its forcing is small. Reasons why BC and other aerosols can provoke disproportionately large responses include their ability to warm snow, either directly melting it or priming it for earlier melt, enhanced snow grain metamorphism, which darkens the snow itself and increases the radiative perturbation by impurities, and amassing of impurities at the surface during melt. Changes in the timing of snow ablation, however, have the greatest influence on the surface energy balance because of the huge contrast in surface reflectance between snow and most other surfaces. Hence, the subtler effects of snow impurities come into play when they combine to influence snowmelt timing, as they apparently do in both 1998 and 2001 central experiments.



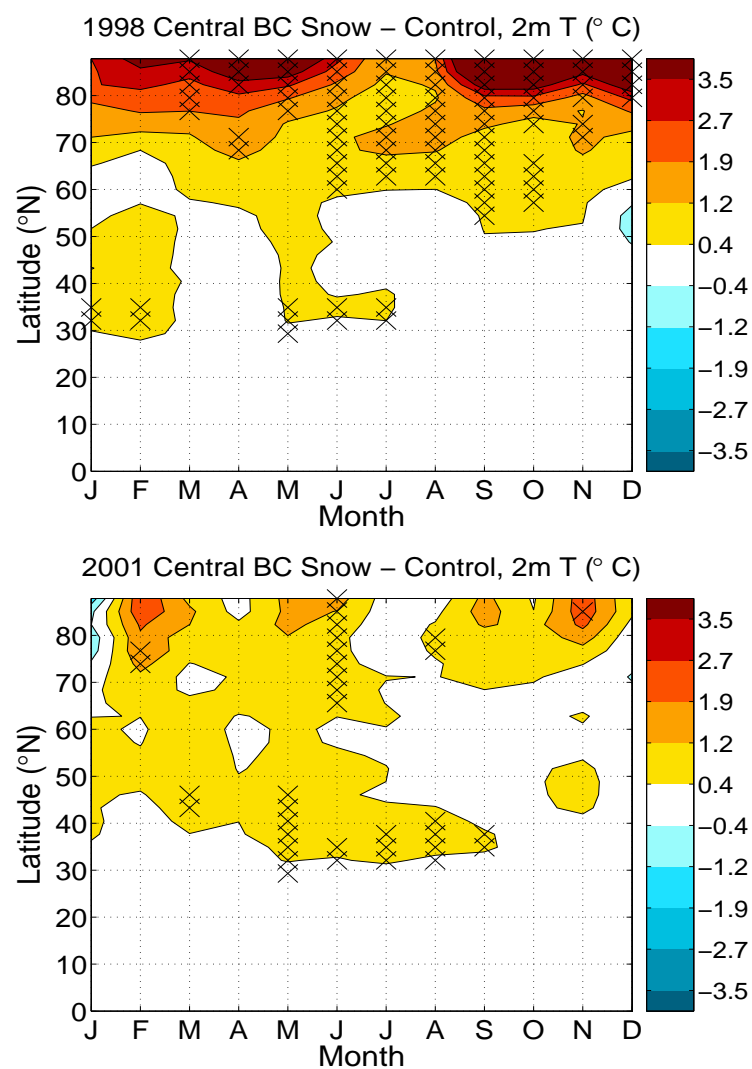


FIGURE 4.10. Difference in zonal monthly mean 2-meter air temperature between central BC/snow experiments and their respective controls. Hatching shows statistically significant change at the 0.01 level.

#### 4.4.6 Individual Uncertainties

Finally, we examine the influence, to first order, that each of the five uncertainties discussed in Methods have individually on global snow/BC forcing. This offers insight into the relative importance of constraining uncertainty in each factor.

To derive estimates of variability in global annual mean  $F_{s,snow}$ , we performed the following experiments: For the role of BC emission scenarios, we conducted two 6-year simulations using 1998 central configuration (Table 4.1), but with low and high emissions estimates. For optical properties, we conducted offline 470-band SNICAR experiments, estimating hypothetical forcing assuming less-absorptive and more-absorptive BC, given annual-mean BC concentration and  $r_e$  at each gridcell of the 1998 central experiment. For snow aging, we also used offline SNICAR to estimate forcing at each gridcell, assuming annual mean BC concentration from the 1998 central experiment, but using the corresponding annual-mean  $r_e$  from the 1998 low and high experiments, representing slow and rapid aging. (If a gridcell contained snow in the central experiment, but not in the high or low, we assumed the global-mean high or low  $r_e$ ). For the role of meltwater scavenging, we conducted another pair of 6-year CAM3 experiments with 1998 central configuration, but with meltwater scavenging factor ranging by two orders of magnitude (Table 4.1). Finally, we assess the role of SCF by scaling the BC/snow forcing at each gridcell of monthly output according to hypothetical SCF (calculated from snow depth), using the high and low representations discussed in Methods. Note that it would be more appropriate to estimate optical property and aging uncertainty at monthly resolution, as with SCF, but this would require an excessive number of offline SNICAR runs.

The range in mean  $F_{s,snow}$  estimated with these approaches is shown in Table 4.4. Uncertainty in emissions has the largest bearing on BC/snow forcing, closely followed by snow aging. The low–high range of FF+BF emissions from *Bond et al.* (2004) is greater than the range we derive for BB emissions (Table 4.1). Some of this difference is because we derive uncertainty using an observational inversion constraint, whereas uncertainty from *Bond et al.* (2004) is derived from compounding forward uncertainties. Global mean snow  $r_e$  varied from 91 – 812  $\mu m$  between 1998 low and high experiments. While our choice of scaling snow aging by a factor of 2 was purely

TABLE 4.4. Estimated range of change in global mean BC/snow radiative forcing ( $F_{s,snow}$ ), represented as a scalar, resulting from variation of individual factors. The range is relative to 1998 central estimates, using low and high estimates of each factor in Table 4.1

	Low	High
BC Emissions	0.54	2.00
Snow Aging	0.58	1.58
Melt Scavenging	0.69	1.08
Optical Properties	0.88	1.12
Snow Cover Fraction	0.83	1.08

subjective, there are no observations of all relevant parameters required to constrain aging processes (*Flanner and Zender, 2006*). Uncertainty in scavenging factor can significantly decrease the global forcing estimate, but raise it only slightly. This happens because scavenging, even for hydrophilic impurities, is relatively inefficient in the central estimates. Thus decreasing the scavenging ratio increases the forcing only minimally in the high experiment, as impurities tend to reside near the surface during melt in the central experiment. Increasing the scavenging efficiency, however, significantly lowers the global forcing estimates, as impurities efficiently flush through the snowpack during the melt phase. *Grenfell et al. (2002)* report relatively uniform vertical profiles of BC in the snow on sea-ice during the SHEBA campaign in late March and April 1998. More observations of BC profiles during the melt phase will help constrain scavenging ratios. Additional offline SNICAR experiments showed that the range of effect of varying BC optical properties was relatively insensitive to snow grain size, in spite of the sensitivity of forcing to grain size (Figure 4.3), but the range narrowed slightly with increasing BC concentrations. Finally, the range of effect of SCF representation is small but slightly asymmetrical. This can be explained by the probability density function of snow depth where and when BC forcing operates. Snow depths greater than 20 cm predict SCF close to 1 with both central and high estimates, but much lower SCF with low estimates.

## 4.5 Conclusions

We incorporate our SNICAR model into the NCAR CAM3 GCM to improve quantification of present-day forcing, climate response, and associated uncertainties from black carbon (BC) in snow. This is the first global climate study which treats coupled snow aerosol heating and snow aging. We assemble model scenarios which bound the plausible range of present-day BC/snow forcing using combinations of BC emissions, BC optical properties, snow aging, meltwater scavenging of BC, and snow cover fraction. We estimate global annual mean BC/snow surface radiative forcings from all BC sources of  $+0.054$  ( $0.007-0.13$ ) and  $+0.049$  ( $0.007-0.12$ )  $\text{W m}^{-2}$  during strong (1998) and weak (2001) boreal fire years, respectively. The forcing contributions from only fossil fuel+biofuel and only fossil fuel sources are  $+0.043$  and  $+0.033$   $\text{W m}^{-2}$ , respectively. Central estimate predictions of BC concentrations in snow capture the nearly 4 orders of magnitude range in observations with no apparent systematic bias, lending some confidence to our central forcing estimates. However, uncertainty in BC emissions and snow aging can individually account for a nearly two-fold range in forward-modeled global forcing. Uncertainty arising from the other factors is of order 20%.

Global annual mean equilibrium warming resulting from the inclusion of BC in snow is  $0.15$  and  $0.10$   $^{\circ}\text{C}$  for 1998 and 2001 central experiments, respectively. Annual arctic ( $66.5-90^{\circ}\text{N}$ ) warming, however, is  $1.61$  and  $0.50^{\circ}\text{C}$ . Arctic annual mean surface albedo for these two experiments is reduced by  $0.047$  and  $0.017$ , relative to their control simulations without BC in snow. 1998 and 2001 land snowmelt rates north of  $50^{\circ}\text{N}$  are 28% and 19% greater in the month preceding maximum melt of control simulations. These statistically significant climate signals all indicate that snow-albedo feedback is triggered by present-day BC/snow forcing. Greater climate response in 1998 might be attributable to strong boreal fires, which increase arctic BC/snow forcing by 17% relative to 2001. Climate response in our 1998 central experiment was unusually strong, however, and more simulations are needed to test this hypothesis. 1998 boreal fire strength peaked in August and September, whereas fires occurring in April–June have the greatest BC/snow forcing potential because of strong high-latitude insolation and large snow areal coverage. Even in the strong

boreal fire year, we attribute 80% of the global BC/snow forcing to fossil fuel and biofuel sources.

Mean efficacy (*Hansen et al.*, 2005) of our 5 experiments is 3.17(2.1 – 4.5). This mean closely matches efficacy obtained from a long experiment with 10× present-day BC emissions, likely providing a more realistic efficacy estimate because of large temperature response relative to natural variability. BC in snowpack can provoke disproportionately large springtime climate response because the forcing tends to coincide with the onset of snowmelt, thus triggering more rapid snow ablation and snow-albedo feedback. The model and methods we develop here could be applied to study snow forcing by other aerosols, including mineral dust, volcanic ash, brown carbon, and marine sediment in sea-ice (*Light et al.*, 1998). Sparseness of snow impurity measurements and uncertainty in snow effective radius variability suggest that more ground measurements need to be made and remote-sensing techniques refined to constrain understanding of this phenomenon on a global scale.

## 4.6 Acknowledgments

We thank Steve Warren for insightful comments after reviewing our manuscript and providing the spectral albedo measurements for Figure 4.2. We also thank two anonymous reviewers for comments. We thank Tami Bond for providing advice and recent manuscripts on black carbon optical properties, Prasad Kasibhatla for providing carbon monoxide inversion factors, M. Andreae for providing updated fire emission factors, Tom Painter for the opportunity to observe and measure, first-hand, snow-impurity effects, and Dani Bundy and Mariana Vertenstein for advice on CAM/SNICAR coupling. Funding for this work was provided by NSF/NCAR SGER ATM-0503148 and NASA Earth System Science Fellowship NNG05GP30H. Computations supported by Earth System Modeling Facility NSF ATM-0321380.

# CHAPTER 5

## Conclusions

### 5.1 Summary of Results

In Chapter 2 we identified a snow treatment problem in the Community Land Model (CLM). All solar radiative absorption was prescribed to occur in the surface snow layer, which never exceeds 2 cm thickness. Using our multi-layer SNICAR model, we find that 20–45% of total solar absorption (nearly all of it in the visible portion of the spectrum), occurs more than 2 cm beneath the surface, depending on solar zenith angle, snow density, and effective grain size. With high solar zenith angle, surface insolation and the fraction of deep absorption are both small. Hence, the CLM assumption of all-surface absorption does not produce large errors in polar regions, but can be significantly biased in mid-latitudes. Monthly-mean sub-2 cm radiative absorption can exceed  $25 \text{ W m}^{-2}$  over the Tibetan Plateau, a unique region because of its coldness, equatorial proximity, and sparse vegetation cover.

Incorporating SNICAR into CLM, coupled with the Community Atmosphere Model (CAM3), and predicting realistic vertically-resolved solar absorption in snow, we identified large improvements in model climate over the Tibetan Plateau. Snowmelt occurred beneath the snow surface, consistent with field observations of snow exposed to strong insolation (*Koh and Jordan, 1995*). Subsurface melt happens because the snow surface emits more longwave energy than it absorbs from the atmosphere, offsetting surface heating from solar absorption, whereas snow several

centimeters deep tends to have net longwave balance closer to zero. Furthermore, snow can maintain large temperature gradients because it is a poor thermal conductor. Reduction in model snow mass via melt triggered strong snow-albedo feedback as the areal fraction of snow cover diminished. Winter snow mass on the Tibetan Plateau was reduced by 80% when energy absorption was re-partitioned, and surface air temperature increased by several degrees. These changes brought model climate closer to station and satellite-derived observations of snow mass and surface temperature in this region. This study also showed that snow-albedo feedback can be triggered solely by energy repartitioning within the snow column (i.e., with no change in bulk snow reflectance).

Chapter 3 develops a model to predict snow effective grain size evolution. As identified in Chapter 2, effective grain size determines the fraction of subsurface solar absorption. It also determines bulk snow reflectance and the magnitude of perturbation by snow impurities. Therefore, it is critical to know the time-dependent snow effective grain size for climate and snow-albedo feedback studies. Our model of effective grain size considers an evolving size distribution of ice particles, governed by the diffusion of water vapor. Re-distribution of vapor and ice is driven by the Kelvin Effect, snow temperature gradient, temperature, and density. The influence of these bulk snow state variables on grain size evolution is also controlled by the initial size distribution (wider size distributions enhance the Kelvin Effect) and degree of irregularity in particle spacing (which enhances vapor availability for some particles and reduces it for others).

We find decent agreement of model-predicted specific surface area (SSA) with observations under isothermal conditions (*Legagneux et al.*, 2004), suggesting that representation of the Kelvin Effect is realistic for the (very limited) observed range of temperature and initial SSA. At the time of writing Chapter 3, there were no observations of snow SSA evolution under temperature gradient. However, model predictions of mean grain size agree well with observations under a wide range of temperature gradient (*Fukuzawa and Akitaya*, 1993) when we choose the degree of particle spacing irregularity.

Linking SSA evolution with the radiative transfer component of SNICAR, we identify the Kelvin Effect as the primary driver of albedo decay in the first day

or two following snowfall. This happens as sharply curved, dendritic branches of snowflakes (represented in our model with very small spheres) sublimate rapidly, reducing specific surface area. Albedo evolution afterward is primarily governed by temperature gradient, but its influence is modulated by snow temperature and density. Large temperature gradient drives rapid albedo decay in the presence of warm snow temperature and low density.

Chapter 4 explores the influence of black carbon in snow on global climate. We carry out a series of sensitivity studies using SNICAR coupled with a version of CAM3 that includes prognostic carbon aerosol transport (*Rasch et al.*, 2001). Our GCM experiments identify the influence, via changes in snow reflectance, of strong and weak boreal fires, and the range in radiative forcing attributed to uncertainty in black carbon emissions, rate of snow aging, efficiency of black carbon removal from snow with meltwater (controlled by the scavenging ratio), black carbon optical properties, and representation of snow cover fraction. The ranking of influence on radiative forcing follows the order just listed.

We estimate global mean surface radiative forcings from all black carbon in snow of  $+0.054$  ( $0.007 - 0.13$ ) and  $+0.049$  ( $0.007 - 0.12$ )  $\text{W m}^{-2}$  in strong (1998) and weak (2001) boreal fire years, respectively. The large uncertainty range reflects compounding uncertainty of the factors listed above. We estimate forcing from anthropogenic (fossil fuel+biofuel) sources of  $+0.043$   $\text{W m}^{-2}$ , slightly smaller than previous estimates (*Jacobson*, 2004b; *Hansen et al.*, 2005). However, we observe very large temperature response to these forcings, implying forcing efficacy, or change in global mean temperature per unit power of radiative forcing, more than three times that of  $\text{CO}_2$ . This is the highest estimate of efficacy reported from any forcing agent. We attribute this to snow-albedo feedback and warming-induced snow grain growth, which is a feedback not captured in any previous study. Snow-albedo feedback is uniquely strong because 1) the forcing only operates over snow but is averaged globally, and 2) the forcing is maximum coincidentally with snowmelt onset, or precisely when it can have the greatest impact on snowmelt timing. The springtime forcing maximum occurs because of the combination of strong insolation and large snow cover; a combination that is absent during the snow accumulation phase when local insolation is low. Future forcing will depend on changes in snow cover, mid- and high-latitude indus-



trial emissions (caused by changes in technology and sources like ship traffic), boreal fire regime, which is expected to intensify (*Flannigan et al.*, 2005), and agricultural clearing practices.

## 5.2 Implications for Future Studies

Chapter 2 showed that subsurface radiative absorption can trigger feedback with low solar zenith angle and intense surface insolation. In present-day climate this is only important in mid-latitude, low-vegetation regions. Could this process have been important over ice sheets in past climates when solar zenith angle was lower over northern polar regions and summer solstice insolation greater? This issue could be investigated with a multi-layer model like SNICAR, coupled either to a climate model or a column energy balance model like SNTHERM (*Jordan*, 1991).

In Chapter 4, we compare modeled snow albedo with precise, spectrally-resolved measurements in Antarctica (*Grenfell et al.*, 1994). We can obtain very good agreement with measurements over the entire solar spectrum when we introduce a very thin (0.25 mm thick) layer of fine-grained snow, which determines reflectance at wavelengths greater than  $1.2\mu\text{m}$ . Although this assumption is reasonable, there have been no studies which simultaneously measure spectrally-resolved albedo, vertically-resolved SSA (or effective grain size) at sufficient resolution, and impurity concentration. Such measurements would bring full closure, or identify inconsistencies with, radiative transfer predictions of snow albedo. Although there is currently a vertical resolution limit of about 1 mm for SSA measurements, information about the vertical distribution of this optically-important snow property would be helpful.

Chapter 3 presents a microphysical model framework for the prediction of dry snow SSA and effective grain size evolution. Although it treats vapor diffusion processes in a consistent, thorough manner, it is not a comprehensive model of snow albedo evolution, which also depends on wind, liquid water content, and melt-freeze cycles. Wind has competing effects on albedo evolution. High sublimation rates and delayed settling of the finest suspended crystals from wind-entrained snow leave a surface composed of small crystals (*Grenfell et al.*, 1994). Wind also accelerates grain

growth by circulating vapor quickly through surface snow (*Cabanes et al.*, 2003). Field observations show large jumps in grain size when snow melts during daytime and then re-freezes at night. A comprehensive model of snow albedo evolution must also account for these processes.

There are numerous possibilities of how interaction between snow aging, climate, and impurities will behave in the future. Possible changes in the evolution of optically-important snow properties include:

- Faster grain growth associated with warmer snow temperatures.
- Slower grain growth because of decreased near-surface temperature gradient, induced by enhanced nighttime downwelling longwave radiation from a stronger greenhouse effect.
- Faster grain growth associated with greater, or more frequent presence, of liquid water.
- Faster grain growth caused by increases in absorbing impurities in snow. Sources of important changes in aerosol emissions could include pan-Arctic ship traffic, boreal fire regime changes, deforestation, and technology change.
- Snow with lower albedo caused by less frequent (but more intense) precipitation events (*IPCC*, 2001), providing more time for snow to age.

The net result of all these effects is, of course, highly uncertain. However, as coupled snow-aerosol-climate models like SNICAR develop, understanding of these interactions, which determine the strength of snow-albedo feedback, will improve.

Chapter 4 showed that the climate system is highly sensitive to small changes in snow reflectance caused by black carbon. What impact does black carbon have on glacier evolution? We suspect that tropical glaciers like Kilimanjaro are influenced by black carbon because 1) many are near to strong biofuel and biomass burning sources, and 2) small black carbon concentrations in snow are much more potent in the tropics, where surface insolation is intense year-round, and solar zenith angle low.

Finally, how important are other snow impurities to climate? Other aerosols are much less absorptive than black carbon, but may be present in much greater

mass mixing ratios. Mineral dust may be important in mountainous regions near strong dust sources, and globally important during glacial periods when global dust emissions were many times greater than today (e.g., *Mahowald et al.*, 2006). Volcanic ash could have strong episodic influence on snow reflectance regionally or globally. Recent research (e.g., *Andreae and Gelencser*, 2006) has shown widespread presence of atmospheric “brown carbon,” which has unique spectral absorption properties, and whose absorption is not accounted for by current black carbon emission inventories. As aerosol characterization improves, so will our understanding of their influence on climate via snow albedo.

# BIBLIOGRAPHY

- Adams, E. E., and R. L. Brown (1982), A model for crystal development in dry snow, *Geophys. Res. Lett.*, *9*(11), 1287–1289.
- Adams, E. E., and R. L. Brown (1983), Metamorphism of dry snow as a result of temperature gradient and vapor density differences, *Ann. Glaciol.*, *4*, 1–9.
- Akitaya, E. (1974), Studies on depth hoar, *Contrib. Inst. Low Temp. Sci., Ser. A*, *26*(67).
- Andreae, M. O., and A. Gelencser (2006), Black carbon or brown carbon? The nature of light-absorbing carbonaceous aerosols, *Atmos. Chem. Phys.*, *6*, 3131–3148.
- Andreae, M. O., and P. Merlet (2001), Emission of trace gases and aerosols from biomass burning, *Global Biogeochem. Cycles*, *15*(4), 955–966.
- Aoki, T., T. Aoki, M. Fukabori, A. Hachikubo, Y. Tachibana, and F. Nishio (2000), Effects of snow physical parameters on spectral albedo and bidirectional reflectance of snow surface, *J. Geophys. Res.*, *105*(D8), 10,219–10,236.
- Aoki, T., A. Hachikubo, and M. Hori (2003), Effects of snow physical parameters on shortwave broadband albedos, *J. Geophys. Res.*, *108*(D19), doi:10.1029/2003JD003506.
- Armališ, S. (1999), Wet deposition of elemental carbon in Lithuania, *The Science of the Total Environment*, *239*, 89–93.
- Arons, E. M., and S. Colbeck (1995), Geometry of heat and mass transfer in dry snow: A review of theory and experiment, *Rev. Geophys.*, *33*(4), 463–493.
- Baunach, T., C. Fierz, P. K. Satyawali, and M. Schneebeli (2001), A model for kinetic grain growth, *Ann. Glaciol.*, *32*, 1–6.
- Blanford, H. F. (1884), On the connection of the Himalaya snowfall with dry winds and seasons of drought in India, *Proc. Roy. Soc. London*, *37*, 3–22.
- Bohren, C. F., and D. R. Huffman (1983), *Absorption and Scattering of Light by Small Particles*, 530 pp., John Wiley & Sons, New York, NY.

- Bond, T. C. (2001), Spectral dependence of visible light absorption by carbonaceous particles emitted from coal combustion, *Geophys. Res. Lett.*, *28*(21), 4075–4078.
- Bond, T. C., and R. W. Bergstrom (2006), Light absorption by carbonaceous particles: An investigative review, *Aerosol Sci. Technol.*, *40*(1), 27–67, doi: 10.1080/02786820500421521.
- Bond, T. C., D. G. Streets, K. F. Yarber, S. M. Nelson, J.-H. Woo, and Z. Klimont (2004), A technology-based global inventory of black and organic carbon emissions from combustion, *J. Geophys. Res.*, *109*, D14203, doi:10.1029/2003JD003697.
- Bond, T. C., G. Habib, and R. W. Bergstrom (2006), Limitations in the enhancement of visible light absorption due to mixing state, *J. Geophys. Res.*, *111*, D20211, doi: 10.1029/2006JD00731.
- Brandt, R. E., and S. G. Warren (1993), Solar-heating rates and temperature profiles in Antarctic snow and ice, *J. Glaciol.*, *39*(131), 99–110.
- Briegleb, B. P. (1992), Delta-Eddington approximation for solar radiation in the NCAR Community Climate Model, *J. Geophys. Res.*, *97*(D7), 7603–7612.
- Briegleb, B. P., C. M. Bitz, E. C. Hunke, W. H. Lipscomb, M. M. Holland, J. L. Schramm, and R. E. Moritz (2004), Scientific description of the sea ice component in the Community Climate System Model, version three, *Tech. Rep. NCAR/TN-463+STR*, National Center for Atmospheric Research.
- Brown, R. L., P. K. Satyawali, M. Lehning, and P. Bartelt (2001), Modeling the changes in microstructure of snow during metamorphism, *Cold Reg. Sci. Tech.*, *33*, 91–101.
- Brun, E. (1989), Investigation of wet-snow metamorphism in respect of liquid-water content, *Ann. Glaciol.*, *13*, 22–26.
- Bryant, F. D., and P. Latimer (1969), Optical efficiencies of large particles of arbitrary shape and orientation, *J. Colloid Interface Sci.*, *30*, 291–304.
- Budyko, M. I. (1969), The effects of solar radiation on the climate of the earth, *Tellus*, *21*, 611–619.
- Cabanes, A., L. Legagneux, and F. Domine (2003), Rate of evolution of the specific surface area of surface snow layers, *Environ. Sci. Tech.*, *37*(4), 661–666.
- Cachier, H. (1997), Particulate and dissolved carbon in air and snow at the Summit site, in *Transfer of Aerosols and Gases to Greenland Snow and Ice: Final Technical Report*, Cedex, France, pp. 21–27.
- Cachier, H., and M. H. Pertuisol (1994), Particulate carbon in Arctic ice, *Analysis Magazine*, *22*, M34–M37.

- Cadle, S. H., and J. M. Dasch (1988), Wintertime concentrations and sinks of atmospheric particulate carbon at a rural location in northern Michigan, *Atmos. Environ.*, *22*(7), 1373–1381.
- Cess, R. D., et al. (1991), Interpretation of snow-climate feedback as produced by 17 general circulation models, *Science*, *253*, 888–892.
- Chang, A. (1995), Nimbus-7 SMMR global monthly snow cover and snow depth, Boulder, CO, USA: National Snow and Ice Data Center. Digital media.
- Chang, A., and A. Rango (2004), AMSR-E/Aqua monthly L3 global snow water equivalent EASE-Grids V001, Boulder, CO, USA: National Snow and Ice Data Center. Digital media.
- Chang, H., and T. T. Charalampopoulos (1990), Determination of the wavelength dependence of refractive indices of flame soot, *Proc. Roy. Soc. London A, Math. and Phys. Sci.*, *430*(1880), 577–591.
- Chiruta, M., and P. K. Wang (2003), The capacitance of rosette ice crystals, *J. Atmos. Sci.*, *60*, 836–846.
- Chylek, P., V. Srivastava, L. Cahenzli, R. G. Pinnick, R. L. Dod, and T. Novakov (1987), Aerosol and graphitic carbon content of snow, *J. Geophys. Res.*, *92*(D8), 9801–9809.
- Chylek, P., B. Johnson, and P. A. Damiano (1995), Biomass burning record and black carbon in the GISP2 Ice Core, *Geophys. Res. Lett.*, *22*(2), 89–92.
- Chylek, P., L. Kou, B. Johnson, F. Boudala, and G. Lesins (1999), Black carbon concentrations in precipitation and near surface air in and near Halifax, Nova Scotia, *Atmos. Environ.*, *33*, 2269–2277.
- Clarke, A., and K. Noone (1985), Soot in the Arctic: A cause for perturbation in radiative transfer, *J. Geophys. Res.*, *19*(12), 2045–2053.
- Colbeck, S. C. (1980), Thermodynamics of snow metamorphism due to variations in curvature, *J. Glaciol.*, *26*(94), 291–301.
- Colbeck, S. C. (1983a), Theory of metamorphism of dry snow, *J. Geophys. Res.*, *88*(C9), 5475–5482.
- Colbeck, S. C. (1983b), Ice crystal morphology and growth rates at low supersaturations and high temperatures, *J. Appl. Phys.*, *54*(5), 2677–2682.
- Colbeck, S. C. (1993), The vapor diffusion coefficient for snow, *Water Resour. Res.*, *29*(1), 109–115.
- Colbeck, S. C. (2001), Sintering of unequal grains, *J. Appl. Phys.*, *89*(8), 4612–4618.

- Collins, W. D. (2001), Parameterization of generalized cloud overlap for radiative calculations in general circulation models, *J. Atmos. Sci.*, *58*, 3224–3242.
- Collins, W. D., P. J. Rasch, B. E. Eaton, D. W. Fillmore, , and J. T. Kiehl (2002), Simulation of aerosol distributions and radiative forcing for INDOEX: Regional climate impacts, *J. Geophys. Res.*, *107*(D19, 8028), doi:10.1029/2000JD000032.
- Collins, W. D., P. J. Rasch, B. A. Boville, J. J. Hack, J. R. McCaa, D. L. Williamson, J. T. Kiehl, and B. Briegleb (2004), Description of the NCAR Community Atmosphere Model (CAM 3.0), *Tech. Rep. NCAR/TN-464+STR*, National Center for Atmospheric Research.
- Conway, H., A. Gades, and C. F. Raymond (1996), Albedo of dirty snow during conditions of melt, *Water Resour. Res.*, *32*(6), 1713–1718.
- Cooke, W. F., C. Lioussé, and H. Cachier (1999), Construction of a 1 x 1 fossil fuel emission data set for carbonaceous aerosol and implementation and radiative impact in the ECHAM4 model, *J. Geophys. Res.*, *104*(D18), 22,137–22,162.
- Croll, J. (1867), On the change in the obliquity of the ecliptic, its influence on the climate of the polar regions and on the level of the sea, *Philosophical Magazine*, *33*, 426–445.
- Dasch, J. M., and S. H. Cadle (1989), Atmospheric carbon particles in the Detroit urban area: Wintertime sources and sinks, *Aerosol Sci. Tech.*, *10*, 236–248.
- Domine, F., and P. B. Shepson (2002), Air-snow interactions and atmospheric chemistry, *Science*, *297*, 1506–1510.
- Douville, H., J.-F. Royer, and J.-F. Mahfouf (1995), A new snow parameterization for the Meteo-France climate model Part I: validation in stand-alone experiments, *Climate Dyn.*, *12*, 21–35.
- Dozier, J. (1989), Spectral signature of alpine snow cover from the Landsat Thematic Mapper, *Remote Sens. Environ.*, *28*, 9–22.
- Ebert, E. E., and J. A. Curry (1992), A parameterization of ice cloud optical properties for climate models, *J. Geophys. Res.*, *97*(D4), 3831–3836.
- Fasullo, J. (2004), A stratified diagnosis of the Indian Monsoon–Eurasian snow cover relationship, *J. Climate*, *17*, 1110–1122.
- Fierz, C., and T. Baunach (2000), Quantifying grain shape changes in snow subject to large temperature gradients, *Ann. Glaciol.*, *31*, 439–444.
- Fily, M., B. Bourdelles, J. P. Dedieu, and C. Sergent (1997), Comparison of in situ and Landsat Thematic Mapper derived snow grain characteristics in the Alps, *Remote Sens. Environ.*, *59*, 452–460.

- Flanner, M. G., and C. S. Zender (2005), Snowpack radiative heating: Influence on Tibetan Plateau climate, *Geophys. Res. Lett.*, *32*, L06501, doi:10.1029/2004GL022076.
- Flanner, M. G., and C. S. Zender (2006), Linking snowpack microphysics and albedo evolution, *J. Geophys. Res.*, *111*, D12208, doi:10.1029/2005JD006834.
- Flanner, M. G., C. S. Zender, J. T. Randerson, and P. J. Rasch (2007), Present day climate forcing and response from black carbon in snow, *J. Geophys. Res.*, *in press*.
- Flannigan, M. D., K. A. Logan, B. D. Amiro, W. R. Skinner, and B. J. Stocks (2005), Future area burned in Canada, *Climatic Change*, *72*, 1–16, doi:10.1007/s10584-005-5935-y.
- Foster, D. J., Jr., and R. D. Davy (1988), Global snow depth climatology, *Tech. Rep. USAFETAC/TN-88/006*, USAF Publication, Scott Air Force Base, Illinois, 48 pp.
- Foster, J., et al. (1996), Snow cover and snow mass intercomparisons of general circulation models and remotely sensed datasets, *J. Climate*, *9*, 409–426.
- Fukuzawa, T., and E. Akitaya (1993), Depth-hoar crystal growth in the surface layer under high temperature gradient, *Ann. Glaciol.*, *18*, 39–45.
- Ganguly, D., A. Jayaraman, H. Gadhavi, and T. A. Rajesh (2005), Features in wavelength dependence of aerosol absorption observed over central India, *Geophys. Res. Lett.*, *32*, L13821, doi:10.1029/2005GL023023.
- Giddings, J. C., and E. LaChapelle (1962), The formation rate of depth hoar, *J. Geophys. Res.*, *67*(6), 2377–2383.
- Grenfell, T., S. Warren, and P. Mullen (1994), Reflection of solar radiation by the Antarctic snow surface at ultraviolet, visible, and near-infrared wavelengths, *J. Geophys. Res.*, *99*(D9), 18,669–18,684.
- Grenfell, T., B. Light, and M. Sturm (2002), Spatial distribution and radiative effects of soot in the snow and sea ice during the SHEBA experiment, *J. Geophys. Res.*, *107*(C10), 8032, doi:10.1029/2000JC000414.
- Grenfell, T. C. (1991), A radiative transfer model for sea ice with vertical structure variations, *J. Geophys. Res.*, *96*(C9), 16,991–17,001.
- Grenfell, T. C., and G. A. Maykut (1977), The optical properties of ice and snow in the Arctic Basin, *J. Glaciol.*, *18*(445–463).
- Grenfell, T. C., and S. G. Warren (1999), Representation of a nonspherical ice particle by a collection of independent spheres for scattering and absorption of radiation, *J. Geophys. Res.*, *104*(D24), 37,697–31,709.
- Grenfell, T. C., D. K. Perovich, and J. A. Ogren (1981), Spectral albedos of an alpine snowpack, *Cold. Reg. Sci. Tech.*, *4*, 121–127.



- Grenfell, T. C., S. P. Neshyba, and S. G. Warren (2005), Representation of a non-spherical ice particle by a collection of independent spheres for scattering and absorption of radiation: 3. Hollow columns and plates, *J. Geophys. Res.*, *110*, D17203, doi:10.1029/2005JD005811.
- Gubler, H. (1985), Model for dry snow metamorphism by interparticle vapor flux, *J. Geophys. Res.*, *90*(D5), 8081–8092.
- Hall, A. (2004), The role of surface albedo feedback in climate, *J. Climate*, *17*, 1550–1568.
- Hansen, J., and L. Nazarenko (2004), Soot climate forcing via snow and ice albedos, *PNAS*, *101*(2), 423–428.
- Hansen, J., M. Sato, and R. Ruedy (1997), Radiative forcing and climate response, *J. Geophys. Res.*, *102*, 6831–6864.
- Hansen, J., et al. (2005), Efficacy of climate forcings, *J. Geophys. Res.*, *110*, D18104, doi:10.1029/2005JD005776.
- Hansen, J., et al. (2006), Climate simulations for 1880-2003 with GISS modelE, *arXiv.org*, arXiv:physics/0610109, available online at <http://arxiv.org/abs/physics/0610109>.
- Hess, M., P. Koepke, and I. Schult (1998), Optical properties of aerosols and clouds: The software package OPAC, *Bull. Am. Meteorol. Soc.*, *79*(5), 831–844.
- Hoffer, A., A. Gelencser, P. Guyon, G. Kiss, O. Schmid, G. Frank, P. Artaxo, and M. O. Andreae (2006), Optical properties of humic-like substances (HULIS) in biomass-burning aerosols, *Atmos. Chem. Phys.*, *6*, 3563–3570.
- Hood, E., M. Williams, and D. Cline (1999), Sublimation from a seasonal snowpack at a continental, mid-latitude alpine site, *Hydrol. Process.*, *13*, 1781–1797.
- Jacobson, M. (2001), Strong radiative heating due to the mixing state of black carbon, *Nature*, *409*, 695–697.
- Jacobson, M. Z. (2004a), The short-term cooling but long-term global warming due to biomass burning, *J. Climate*, *17*, 2909–2926.
- Jacobson, M. Z. (2004b), Climate response of fossil fuel and biofuel soot, accounting for soot’s feedback to snow and sea ice albedo and emissivity, *J. Geophys. Res.*, *109*(D21201), doi:10.1029/2004JD004945.
- Jordan, R. (1991), A one-dimensional temperature model for a snow cover: Technical documentation for SNTHERM 89., *Tech. Rep. Special Report 91-16*, U.S. Army Cold Regions Research and Engineering Laboratory.
- Joseph, J. H., W. J. Wiscombe, and J. A. Weinman (1976), The Delta-Eddington Approximation for radiative flux transfer, *J. Atmos. Sci.*, *33*, 2,452–2,459.

- Kalnay, E., et al. (1996), The NCEP/NCAR 40-year reanalysis project, *Bull. Am. Meteor. Soc.*, *77*, 437–471.
- Kamata, Y., S. A. Sokratov, and A. Sato (1999), Temperature and temperature gradient dependence of snow recrystallization in depth hoar snow, *Lecture Notes in Physics*, *533*, 395–402.
- Kiehl, J. T., C. A. Shields, J. J. Hack, and W. D. Collins (2006), The climate sensitivity of the Community Climate System Model: CCSM3, *J. Climate*, *19*, 2854–2596.
- Kirchstetter, T. W., T. Novakov, and P. V. Hobbs (2004), Evidence that the spectral dependence of light absorption by aerosols is affected by organic carbon, *J. Geophys. Res.*, *109*, D21208, doi:10.1029/2004JD004999.
- Koch, D. (2001), Transport and direct radiative forcing of carbonaceous and sulfate aerosols in the GISS GCM, *J. Geophys. Res.*, *106*(D17), 20,311–20,332.
- Koch, D., and J. Hansen (2005), Distant origins of Arctic black carbon: A Goddard Institute for Space Studies ModelE experiment, *J. Geophys. Res.*, *110*, D04204, doi:10.1029/2004JD005296.
- Koh, G., and R. Jordan (1995), Sub-surface melting in a seasonal snow cover, *J. Glaciol.*, *41*, 474–482.
- Kuhn, M., and L. Siogas (1977), Spectroscopic studies at McMurdo, South Pole and Siple Stations during the austral summer 1977–78, *Antarctic J. U.S.*, *13*, 178–179.
- Kurosaki, Y., and M. Mikami (2004), Effect of snow cover on threshold wind velocity of dust outbreaks, *Geophys. Res. Lett.*, *31*, L03,106, doi:10.1029/2003GL018,632.
- Lavoue, D., C. Liousse, H. Cachier, B. J. Stocks, and J. G. Goldammer (2000), Modeling of carbonaceous particles emitted by boreal and temperate wildfires at northern latitudes, *J. Geophys. Res.*, *105*(D22), 26,871–26,890.
- Legagneux, L., A.-S. Taillandier, and F. Domine (2004), Grain growth theories and the isothermal evolution of the specific surface area of snow, *J. Appl. Phys.*, *95*(11), 6175–6184.
- Lehning, M., P. Bartelt, B. Brown, C. Fierz, and P. Satyawali (2002), A physical SNOWPACK model for the Swiss avalanche warning Part II. Snow microstructure, *Cold. Reg. Sci. Tech.*, *35*, 147–167.
- Light, B., H. Eicken, G. A. Maykut, and T. C. Grenfell (1998), The effect of included particulates on the spectral albedo of sea ice, *J. Geophys. Res.*, *103*(C12), 27,739–27,752.
- Loth, B., and H.-F. Graf (1998), Modeling the snow cover in climate studies 1. Long-term integrations under different climatic conditions using a multilayered snow-cover model, *J. Geophys. Res.*, *103*(D10), 11,313–11,327.

- Lynch, A. H., D. L. McGinnis, and D. A. Bailey (1998), Snow-albedo feedback and the spring transition in a regional climate system model: Influence of land surface model, *J. Geophys. Res.*, *103*(D22), 29,037–29,050.
- Mahowald, N. M., D. R. Muhs, S. Levis, P. J. Rasch, M. Yoshioka, C. S. Zender, and C. Luo (2006), Change in atmospheric mineral aerosols in response to climate: Last glacial period, preindustrial, modern, and doubled carbon dioxide climates, *J. Geophys. Res.*, *111*, D10202, doi:10.1029/2005JD006653.
- Marbouty, D. (1980), An experimental study of the temperature-gradient metamorphism, *J. Glaciol.*, *26*(94), 303–312.
- Marshall, S., and R. Oglesby (1994), An improved snow hydrology for GCMs. Part 1: Snow cover fraction, albedo, grain size, and age, *Climate Dyn.*, *10*, 21–37.
- Marshall, S. E. (1989), A physical parameterization of snow albedo for use in climate models, Ph.D. thesis, The University of Colorado at Boulder, Boulder, CO.
- McGuffie, K., and A. Henderson-Sellers (1985), The diurnal hysteresis of snow albedo, *J. Glaciol.*, *31*, 188–189.
- Miller, D. A. (2002), An integrated microstructural study of dry snow metamorphism under generalized thermal conditions, Ph.D. thesis, Montana State University, Bozeman, MT.
- Miller, D. A., E. E. Adams, and R. L. Brown (2003), A microstructure approach to predict dry snow metamorphism in generalized thermal conditions, *Cold Reg. Sci. Tech.*, *37*, 213–226.
- Molotch, N. P., T. H. Painter, R. C. Bales, and J. Dozier (2004), Incorporating remotely-sensed snow albedo into a spatially-distributed snowmelt model, *Geophys. Res. Lett.*, *31*, L03,501, doi:10.1029/2003GL019,063.
- Myhre, G., T. K. Berntsen, J. M. Haywood, J. K. Sundet, B. N. Holben, M. Johnsrud, and F. Stordal (2003), Modeling the solar radiative impact of aerosols from biomass burning during the Southern African Regional Science Initiative (SAFARI-2000) experiment, *J. Geophys. Res.*, *108*(D13), doi:10.1029/2002JD002313.
- Neshyba, S., T. Grenfell, and S. Warren (2003), Representation of a nonspherical ice particle by a collection of independent spheres for scattering and absorption of radiation: 2. hexagonal columns and plates, *J. Geophys. Res.*, *108*(D15), 10.1029/2002JD003,302.
- New, M., M. Hulme, and P. Jones (1999), Representing twentieth-century space–time climate variability. Part I. Development of a 1961–90 mean monthly terrestrial climatology, *J. Climate*, *12*(3), 829–856.

- Novakov, T., V. Ramanathan, J. E. Hansen, T. W. Kirchstetter, M. Sato, J. E. Sinton, and J. A. Sathaye (2003), Large historical changes of fossil-fuel black carbon aerosols, *Geophys. Res. Lett.*, *30*(6), doi:10.1029/2002GL016345.
- Oleson, K. W., et al. (2004), Technical description of the Community Land Model (CLM), *Tech. Rep. NCAR/TN-461+STR*, National Center for Atmospheric Research.
- Painter, T. H., and J. Dozier (2004), Measurements of the hemispherical-directional reflectance of snow at fine spectral and angular resolution, *J. Geophys. Res.*, *109*, D18115, doi:10.1029/2003JD004458.
- Painter, T. H., J. Dozier, D. A. Roberts, R. E. Davis, and R. O. Greene (2003), Retrieval of subpixel snow-covered area and grain size from imaging spectrometer data, *Remote. Sens. Environ.*, *85*, 64–77.
- Perovich, D. K., T. C. Grenfell, B. Light, and P. V. Hobbs (2002), Seasonal evolution of the albedo of multiyear Arctic sea ice, *J. Geophys. Res.*, *107*(C10), doi:10.1029/2000JC000438.
- Pirazzini, R. (2004), Surface albedo measurements over Antarctic sites in summer, *J. Geophys. Res.*, *109*, D20118, doi:10.1029/2004JD004617.
- Pollack, J. B., and J. N. Cuzzi (1980), Scattering by nonspherical particles of size comparable to a wavelength: A new semi-empirical theory and its application to tropospheric aerosols, *J. Atmos. Sci.*, *37*, 868–881.
- Pruppacher, H. R., and J. D. Klett (1998), *Microphysics of Clouds and Precipitation*, second ed., 954 pp., Kluwer Acad. Publ., Dordrecht, Holland.
- Qu, X., and A. Hall (2006), Assessing snow albedo feedback in simulated climate change, *J. Climate*, *19*, 2617–2630.
- Ramanathan, V., et al. (2001), Indian Ocean Experiment: An integrated analysis of the climate forcing and effects of the great Indo–Asian haze, *J. Geophys. Res.*, *106*(D22), 28,371–28,398.
- Randall, D. A., et al. (1994), Analysis of snow feedbacks in 14 general circulation models, *J. Geophys. Res.*, *99*(D10), 20,757–20,771.
- Rasch, P. J., and J. E. Kristjánsson (1998), A comparison of the CCM3 climate model using diagnosed and predicted condensate parameterizations, *J. Climate*, *11*, 1587–1614.
- Rasch, P. J., W. D. Collins, and B. E. Eaton (2001), Understanding the Indian Ocean Experiment (INDOEX) aerosol distributions with an aerosol assimilation, *J. Geophys. Res.*, *106*(D7), 7337–7355.

- Rasch, P. J., M. Fromm, O. Torres, D. J. Diner, R. Kahn, and J. Martonchik (2005), An exploratory study of the impact of pyro-cumulonimbus injections of aerosol on the upper troposphere and lower stratosphere climate during northern hemisphere summer, *Eos Trans. AGU*, *86*(52), Fall Meet. Suppl., Abstract A22B-01.
- Rogers, R. R., and M. K. Yau (1994), *A Short Course in Cloud Physics*, third ed., Pergamon Press, Oxford, UK.
- Romanov, P., and D. Tarpley (2004), Estimation of snow depth over open prairie environments using GOES imager observations, *Hydrol. Process.*, *18*, 1073–1087, doi:10.1002/hyp.5508.
- Rosenthal, W., J. Saleta, and J. Dozier (2006), Scanning electron microscopy of impurity structures in snow, *Cold. Reg. Sci. Tech.*, *in press*.
- Sato, M., J. Hansen, D. Koch, A. Lacis, R. Reudy, O. Dubovik, B. Holben, M. Chin, and T. Novakov (2003), Global atmospheric black carbon inferred from AERONET, *PNAS*, *100*, 6319–6324.
- Schmidt, G. A., et al. (2006), Present day atmospheric simulations using GISS ModelE: Comparison to in-situ, satellite and reanalysis data, *J. Climate*, *19*(2), 153–192, doi:10.1175/JCLI3612.1.
- Schnaiter, M., H. Horvath, O. Möhler, K.-H. Naumann, H. Saathoff, and O. W. Schöck (2003), UV-VIS-NIR spectral optical properties of soot and soot-containing aerosols, *J. Aerosol. Sci.*, *34*(10), 1421–1444.
- Schneebeli, M., and S. A. Sokratov (2004), Tomography of temperature gradient metamorphism of snow and associated changes in heat conductivity, *Hydrol. Process.*, *18*, 3655–3665, doi:10.1002/hyp.5800.
- Schwerdtfeger, P., and G. Weller (1977), Radiative heat transfer processes in snow and ice, *Antarctic. Res. Ser.*, *25*, 35–39.
- Seinfeld, J. H., and S. N. Pandis (1998), *Atmospheric Chemistry and Physics*, 1326 pp., John Wiley & Sons, New York, NY.
- Sellers, W. D. (1969), A climate model based on the energy balance of the earth-atmosphere system, *J. Appl. Meteorol.*, *8*, 392–400.
- Sergent, C., E. Pougatch, and M. Sudul (1993), Experimental investigation of optical snow properties, *Ann. Glaciol.*, *17*, 281–287.
- Sergent, C., C. Leroux, E. Pougatch, and F. Guirado (1998), Hemispherical-directional reflectance measurements of natural snow: comparison with adding-doubling modeling, *Ann. Glaciol. Soc.*, *26*, 59–63.

- Slater, J. F., L. A. Currie, J. E. Dibb, and J. B. A. Benner (2002), Distinguishing the relative contribution of fossil fuel and biomass combustion aerosols deposited at Summit, Greenland through isotopic and molecular characterization of insoluble carbon, *Atmos. Environ.*, *36*, 4463–4477.
- Slingo, A. (1989), A GCM parameterization for the shortwave radiative properties of clouds, *J. Atmos. Sci.*, *46*, 1419–1427.
- Sokratov, S. A. (2001), Parameters influencing the recrystallization rate of snow, *Cold. Reg. Sci. Tech.*, *33*(2–3), 263–274.
- Sommerfeld, R. A. (1983), A branch grain theory of temperature gradient metamorphism in snow, *J. Geophys. Res.*, *88*(C2), 1484–1494.
- Stamnes, K., S.-C. Tsay, W. Wiscombe, and K. Jayaweera (1988), Numerically stable algorithm for discrete-ordinate-method radiative transfer in multiple scattering and emitting layered media, *Appl. Opt.*, *27*(12), 2502–2509.
- Stephenson, P. J. (1967), Some considerations of snow metamorphism in Antarctic ice sheet in the light of ice crystal studies, in *Physics of Snow and Ice, Part II*, Institute for Low Temperature Science, Hokkaido University.
- Stohl, A. (2006), Characteristics of atmospheric transport into the Arctic troposphere, *J. Geophys. Res.*, *111*, D11306, doi:10.1029/2005JD006888.
- Stroeve, J. C., and A. W. Nolin (2002), New methods to infer snow albedo from the MISR instrument with applications to the Greenland Ice Sheet, *IEEE Trans. Geosci. Remote Sens.*, *40*(7), 1616–1625.
- Sturm, M., and C. S. Benson (1997), Vapor transport, grain growth and depth-hoar development in the subarctic snow, *J. Glaciol.*, *43*(143), 42–59.
- Thomas, G. E., and K. Stamnes (1999), *Radiative Transfer in the Atmosphere and Ocean*, Cambridge Atmospheric and Space Science Series, Cambridge Univ. Press, Cambridge.
- Toon, O. B., C. P. McKay, T. P. Ackerman, and K. Santhanam (1989), Rapid calculation of radiative heating rates and photodissociation rates in inhomogeneous multiple scattering atmospheres, *J. Geophys. Res.*, *94*(D13), 16,287–16,301.
- Van der Werf, G. R., J. T. Randerson, L. Giglio, G. J. Collatz, P. S. Kasibhatla, and A. F. Arellano Jr. (2006), Interannual variability of global biomass burning emissions from 1997 to 2004, *Atmos. Chem. Phys.*, *6*, 3423–3441.
- Verseghy, D. L. (1991), CLASS–A Canadian land surface scheme for GCMs. I. Soil model, *Int. J. Climatology*, *11*, 111–133.
- Warren, S. (1982), Optical properties of snow, *Rev. Geophys.*, *20*(1), 67–89.

- Warren, S., and A. Clarke (1990), Soot in the atmosphere and snow surface of Antarctica, *J. Geophys. Res.*, *95*(D2), 1811–1816.
- Warren, S., and W. Wiscombe (1980), A model for the spectral albedo of snow. II: Snow containing atmospheric aerosols, *J. Atmos. Sci.*, *37*, 2734–2745.
- Warren, S., and W. Wiscombe (1985), Dirty snow after nuclear war, *Nature*, *313*, 467–470.
- Warren, S. G., T. C. Grenfell, and P. C. Mullen (1986), Optical properties of Antarctic snow, *Antarctic Journal of the United States*, *21*(5), 247–248.
- Warren, S. G., I. G. Rigor, N. Untersteiner, V. F. Radionov, N. N. Bryazgin, Y. I. Aleksandrov, and R. Colony (1999), Snow depth on Arctic sea ice, *J. Climate*, *12*, 1814–1829.
- Williams, M. A. (2005), Niwot Ridge Subnivean Data Retrieval System, Niwot Ridge Long Term Ecological Research Project, <http://culter.colorado.edu>.
- Willmott, C. J., and K. Matsuura (2000), Terrestrial air temperature and precipitation: Monthly and annual climatologies, [Available online at <http://climate.geog.udel.edu/~climate>].
- Wiscombe, W. J. (1980), Improved Mie scattering algorithms, *Appl. Opt.*, *19*(9), 1505–1509.
- Wiscombe, W. J., and S. G. Warren (1980), A model for the spectral albedo of snow. I: Pure snow, *J. Atmos. Sci.*, *37*, 2712–2733.
- Wu, T.-W., and Z.-A. Qian (2003), The relation between the Tibetan winter snow and the Asian summer monsoon and rainfall: An observational investigation, *J. Climate*, *16*, 2038–2051.
- Yang, F., A. Kumar, W. Wang, H.-M. H. Juang, and M. Kanamitsu (2001), Snow-albedo feedback and seasonal climate variability over North America, *J. Climate*, *14*, 4245–4248.
- Yang, Z.-L., R. Dickinson, A. Robock, and K. Y. Vinnikov (1997), Validation of snow submodel of the Biosphere-Atmosphere Transfer Scheme with Russian snow cover and meteorological observational data, *J. Climate*, *10*, 353–373.
- Zender, C. S., B. Bush, S. K. Pope, A. Bucholtz, W. D. Collins, J. T. Kiehl, F. P. J. Valero, and J. Vitko, Jr. (1997), Atmospheric absorption during the Atmospheric Radiation Measurement (ARM) Enhanced Shortwave Experiment (ARESE), *J. Geophys. Res.*, *102*(D25), 29,901–29,915.
- Zhang, T., K. Stamnes, and S. A. Bowling (1996), Impact of clouds on surface radiative fluxes and snowmelt in the Arctic and subarctic, *J. Climate*, *9*, 2110–2123.

- Zhang, W., and J. H. Schneibel (1995), The sintering of two particles by surface diffusion and grain boundary diffusion – a two-dimensional numerical study, *Acta Metall. Mater.*, *43*(12), 4377–4386.
- Zwally, H. J., W. Abdalati, T. Herring, K. Larson, J. Saba, and K. Steffen (2002), Surface melt-induced acceleration of Greenland Ice-Sheet flow, *Science*, *297*, 218–222.



# APPENDIX A

## List of Symbols

Symbol	Description	Units
$a$	Particle boundary-boundary spacing	m
$\bar{a}$	Mean particle boundary-boundary spacing	m
$c$	Mass mixing ratio	kg kg <sup>-1</sup>
$D$	Mass deposition flux	kg m <sup>-2</sup> s <sup>-1</sup>
$D_v$	Diffusivity of vapor in air	m <sup>2</sup> s <sup>-1</sup>
$d$	Snow depth	m
$\bar{d}$	Mean particle diameter	m
$E$	Efficacy	—
$F_a$	Adjusted radiative forcing at tropopause	W m <sup>-2</sup>
$F_i$	Instantaneous radiative forcing at tropopause	W m <sup>-2</sup>
$F_s$	Instantaneous radiative forcing at surface	W m <sup>-2</sup>
$F_t$	Instantaneous radiative forcing at top-of-atmosphere	W m <sup>-2</sup>
$\vec{h}$	Vertical distance from particle center to pore center	m
$J_v$	Vapor flux	kg m <sup>-2</sup> s <sup>-1</sup>
$K$	Thermal conductivity of air	J m <sup>-1</sup> s <sup>-1</sup> K <sup>-1</sup>
$k_{\text{phi}}$	Hydrophobic scavenging ratio	fraction
$k_{\text{pho}}$	Hydrophillic scavenging ratio	fraction
$L$	Latent heat of fusion	J kg <sup>-1</sup>
$m$	Particle mass	kg
$P$	Probability	—

Symbol	Description	Units
$p_{amb}$	Ambient (environmental) vapor pressure	Pa
$p_{eq}$	Equilibrium vapor pressure over planar surface	Pa
$p_s$	Equilibrium vapor pressure at particle surface	Pa
$q$	Mass flux	$\text{kg m}^{-2} \text{s}^{-1}$
$R_v$	Specific gas constant for vapor	$\text{J kg}^{-1} \text{K}^{-1}$
$r$	Particle radius	m
$\bar{r}$	Mean particle radius	m
$r_e$	Effective radius	m
$r_{e0}$	Initial effective radius	m
$r_n$	Number-median radius	m
$S_s^l$	Downwelling surface-incident solar power	$\text{W m}^{-2}$
$\hat{S}$	Specific surface area	$\text{m}^2 \text{kg}^{-1}$
$\hat{S}_0$	Initial specific surface area	$\text{m}^2 \text{kg}^{-1}$
$T$	Temperature	K
$T_{2m}$	2-meter temperature	K
$T_s$	Surface temperature	K
$t$	Time	s
$z$	Distance along temperature gradient axis	m
	Surface roughness length	m
$\gamma$	Surface tension of ice against air	$\text{J m}^{-2}$
$\kappa$	Empirical parameter for SSA evolution	—
$\lambda$	Wavelength	m
$\rho_i$	Density of ice	$\text{kg m}^{-3}$
$\rho_s$	Density of snow	$\text{kg m}^{-3}$
$\rho_v$	Density of water vapor	$\text{kg m}^{-3}$
$\rho_{v,amb}$	Ambient (environmental) vapor density	$\text{kg m}^{-3}$
$\rho_{v,s}$	Equilibrium vapor density at particle surface	$\text{kg m}^{-3}$
$\sigma_g$	Geometric standard deviation	—

Symbol	Description	Units
$\tau$	Empirical parameter for SSA evolution	hr
	Optical depth	—
$\tau_a$	Absorption optical depth	—
$\tau_{\text{cld}}$	Cloud extinction optical depth	—
$\phi$	Model parameter, interparticle spacing irregularity	—
$\omega$	Single-scatter albedo	fraction